6-5-2013

Integration technologies for implantable microsystems

Dean Johnson

R·I·T

Integration Technologies For Implantable Microsystems

by

Dean G. Johnson

A Dissertation Submitted in Partial Fulfillment of the Requirements for the Degree of Doctorate of Philosophy in Microsystems Engineering

Department of Electrical Engineering
Kate Gleason College of Engineering

Rochester Institute of Technology
Rochester, NY
June 5, 2013

Author: _____
Microsystems Engineering Program

Certified by: _____
David A. Borkholder, Ph.D.
Professor of Microsystems Engineering

Approved by: _____
Bruce W. Smith, Ph.D.
Director of Microsystems Engineering Program

Certified by: _____
Harvey J. Palmer, Ph.D.
Dean, Kate Gleason College of Engineering

Committee Approval:

Bruce W. Smith, Ph.D. Date
Director of Microsystems Engineering Ph.D. Program

David A. Borkholder, Ph.D. Date
Dissertation Committee Chairperson
Chief Advisor

Denis Cormier, Ph.D. Date
Professor of Microsystems Engineering
Committee Member

Lynn Fuller, Ph.D. Date
Professor of Microsystems Engineering
Committee Member

Sergey Lyshevsky, Ph.D. Date
Professor of Electrical Engineering
Committee Member

ABSTRACT

Kate Gleason College of Engineering
Rochester Institute of Technology

Degree: Doctor of Philosophy **Program**: Microsystems Engineering

Name of Candidate: Dean G. Johnson

Title: Integration Technologies for Implantable Microsystems

Microsystems targeted for implantation require careful consideration of power, thermals, size, reliability, and biocompatibility. The presented research explored appropriate integration technologies for an implantable drug delivery system suitable for use in mice weighing less than 20 grams. Microsystems technology advancements include *in situ* pump diaphragm formation; integrated, low volume microfluidic coupling technologies; and incorporation of a low voltage, low-power pump actuation with a zero-power off state. Utility of the developed integration technologies have been tested through *in vitro* reliability and validation experiments. A four-chamber peristaltic pump was created using micromachining (e.g. thin film deposition and Si etching) and direct write techniques. A novel phase change material based actuator was designed and fabricated to deflect deformable diaphragms into and out of four pump chambers while the diaphragms isolated the pumped fluid from the working material. Polyimide capillary tubing with 140-μm OD was integrated in-plane and acted as fluidic interconnects to a drug supply and to the pharmaceutical delivery site. Parylene C conformal coating and the design for gap occlusion provided sealed, flexible tubing connections to the micropump. The per chamber actuation power of 10.1 mW at 0.083 Hz resulted in fluid flow of over 100 nL/min with an efficiency of 11 mJ/nL.

DEDICATION

At times our own light goes out and is rekindled by a spark from another person. Each of us has cause to think with deep gratitude of those who have lighted the flame within us.

Albert Schweitzer

I dedicate this dissertation to my outrageously loving and supportive wife, Kristen. She is the spark that rekindles my light. Without her understanding and inspiration I would not have been able to complete this work or anything else of importance.

ACKNOWLEDGMENT

No one can whistle a symphony. It takes a whole orchestra to play it.
H.E. Luccock

In working on this project, I have received support and encouragement from many people. Dr. David Borkholder has been a mentor and his guidance has made this an enriching experience. I would like to thank my dissertation committee of Dr. Denis Cormier, Dr. Lynn Fuller, Dr. Sergey Lyshevski, Dr. Mustafa Abushagur, and Dr. Bruce Smith for their support and feedback, which helped move me past roadblocks and kept me focused.

I thank my fellow students; Ivan Puchades, Jirachai Getpreechasawas, Sundar Balasubramanian, Cory Cress, Anuj Datar, Karthik Narayanan, Jing Ouyang, and Zhianming Zhou. The faculty and staff of the SMFL, Sean O'Brien, John Nash, Rich Battaglia, Bruce Tolleson, Scott Blondell, Tom Grimsley, Dave Yackoff, Dr. Alan Raisanen, and Dr. Karl Hirschman were instrumental in supporting the work needed to complete my research. For their work with my cannulae and the mouse model I wish to thank Dr. Robert D. Frisina and Dr. Xiao Xia Zhu. For help with the Parylene C deposition model I thank Dr. Steven Weinstein, Dr. Karuna Koppola, and Dr. Masoumeh Haghpanahi. I also wish to thank Dr. Luane Davis Haggerty and the faculty, staff, and students of NTID for introducing me to Deaf culture.

I would like to thank my children, Katie and Adam. They do not know what they had to put up with but I thank them regardless. My parents, Marian Johnson and Dr. Richard Johnson, showed me that it is never too late to further your education and that all things are possible.

CONTENTS

List of Illustrations

List of Tables

Chapter 1 Introduction

> *The problems of deafness are deeper and more complex, if not more important, than those of blindness. Deafness is a much worse misfortune. For it means the loss of the most vital stimulus--the sound of the voice that brings language, sets thoughts astir and keeps us in the intellectual company of man.*
>
> *Hellen Keller*

Advanced hearing loss and deafness therapies that improve auditory function will require carefully timed and dosed, site-directed delivery of multiple therapeutic compounds throughout an extended test period. Deafness research involving intracochlear delivery of therapeutic agents has been limited to acute experiments with syringes and infusion pumps, and chronic, single compound experiments with implantable osmotic pumps. Syringe and osmotic pumps have proven effective for baseline lab investigations in animal models (Brayden, Oudot, & Baird, 2010; Sefton, 1987), but lack the flexibility required for more sophisticated therapy development. A review of intracochlear drug delivery mechanisms by (Borkholder, 2008) concludes that these animal studies have shown significant variability in treatment effectiveness and impact to cochlear function with the drug delivery profile a prominent factor impacting success. An implantable micropump, which provides a means of controlling flow rates and durations, will allow for the required delivery profile flexibility. In this work, integration technologies have been developed to enable the low implant volume and low flow rates required by the small size of the mouse model.

1.1. Auditory Dysfunction Therapy Development

Damage to the cochlea or to nerves leading from the inner ear to the brain causes sensorineural hearing loss (SNHL). According to the American Speech-Language-Hearing Association, SNHL rarely responds to current medical or surgical therapies. SNHL accounts for 90% of permanent hearing loss and is therefore the most common type affecting approximately 10% of the population and more than half of those over 65 years (URMC, 2012). Hearing loss is the primary communication disorder, is one of the top three chronic medical conditions in the elderly, and is a major factor determining function in these older adults (NIDCD, 2012).

Current treatments for hearing loss include cochlear implants or hearing aids, which address the symptom by amplifying sound, but they do not address the biological basis for the hearing loss and have limited efficacy. There are many bases for hearing loss, such as hair cell damage from age, noise damage, or medications, and each cause may require individualized targeted therapy. Many groups are working hard to find these biological bases, which will lead to the use of gene, stem cell, and pharmaceutical based therapies for auditory dysfunction. Gene based therapies have the potential to not only ameliorate but even *cure* some forms of auditory dysfunction. These therapies may be delivered through systemic application (e.g. oral or injections), or site directed delivery.

Systemic approaches have disadvantages such as requiring large amounts of compounds to deliver small amounts to target areas, effects on non-target systems, and difficulty in controlling dose profile (dose profile can be affected or controlled by metabolism and/or blood circulation). The work of (Nuxoll & Siegel, 2009) concludes that success of therapeutic treatments require site directed delivery along with ‘proper temporal presentation’. Site directed therapies use only what is needed at the target site and allow the delivery system to control the dose profile, improving efficacy and reducing systemic side effects. By targeting the cochlea, auditory hair cells have been successfully regrown in guinea pigs via intracochlear Atoh1 gene infusion (Izumikawa et al., 2005). This experiment highlights the importance of site directed delivery of pharmaceuticals and gene therapies.

1.1.1. Site-Directed Delivery

The site-directed delivery of curative agents with controlled dose profiles has had an important impact on the quality and success of disease treatment (Borkholder, 2008). (Akil et al., 2012) have used gene therapy to restore hearing to deaf mice, a mouse model of congenital deafness in humans. Delivery was accomplished with microinjections into the cochlea either via an apical cochleostomy, or through the round window membrane. This study shows the potential benefits of site-directed delivery for deafness research. Therefore, therapy development for deafness research will likely require delivery directly to the cochlea. The optimization of these therapies will involve delivery of multiple agents with flow rates and durations optimized for maximum effect. This can be accomplished only with animals tethered to a syringe as described in (Carson et al., 2002; Sclafani & Glendinning, 2003) or with an implantable pump technology, which allows user control of rate and duration of delivery. Implantable pumps have the advantage of allowing the animals to recover, providing the ability to perform chronic studies, whereas the syringe pumps allow only acute studies.

1.1.2. Mouse Model System: Benefits and Challenges

Researchers primarily use rats, chinchillas, and guinea pigs for inner ear research (Swan, Mescher, Sewell, Tao, & Borenstein, 2008). The main benefit of using these animal models is their larger size as they are easily handled and surgical approaches to access the cochlea are routine, and the larger cochlear volumes make fluidic access easier.

Two of the benefits of using the mouse model are that its genome is fully mapped and transgenic mice are available to model human disease in a controlled model system for therapy development. Transgenic technology has enabled researchers to study gene function and to model human diseases, enabling the *in vivo* study of the effect of various genes on auditory function. For example (Schütz et al., 2010) studied human bilateral middle/high-frequency hearing loss by using transgenic mice and have used transgenic mice to replicate mutation in the GJB2 and GJB6 genes, the most common cause of prelingual deafness in humans not associated with a syndrome. Inbred mouse strains have been identified as models of deafness and presbycusis, hearing loss that occurs gradually in most individuals as they age. The ability to reproduce in the mouse model the same

anomaly that causes deafness in humans allows researchers to target this type of deafness with gene therapy.

The capacity to study diseases that affect humans in transgenic and mutant animals make the mouse a more desirable animal model than larger animals, such as the guinea pig. However, due to the very small size of the mouse inner ear, 620 nL perilymph volume (Thorne et al., 1999), developing effective, controlled infusion systems for *in vivo* hearing therapy studies is quite challenging. Surgical approaches and fluidic interfacing with the mouse cochlea as in (Kawamoto, et al., 2001) are difficult due to the small size of the cochlea (see Figure 1-1).

The challenges with using the small mouse model for auditory dysfunction therapy

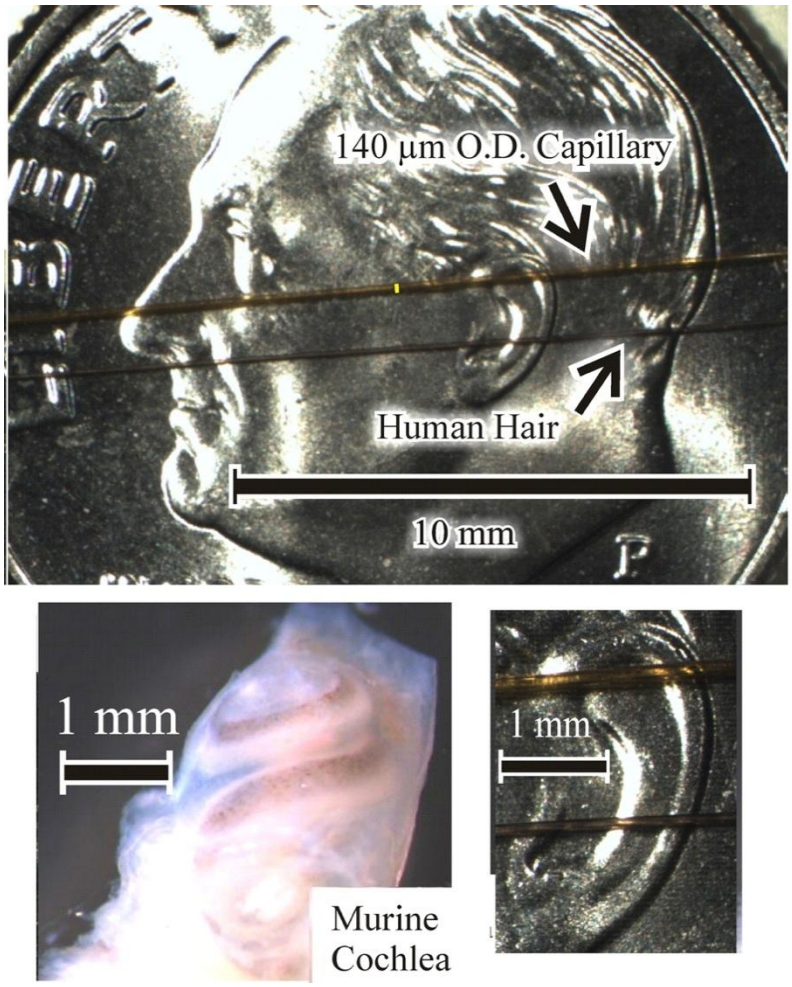

Figure 1-1: Image of murine cochlea for size comparison.
U.S. dime with micro-capillary polyimide tubing used for cochlear infusions (140 µm OD) and human hair (50 µm to 70 µm OD). Image of murine cochlea. Fluid chambers of the mouse cochlea have a volume of ~620 nL.

development include the difficulty in precisely interconnecting the delivery system with the small fluid chambers in the cochlea, avoiding damage to residual hearing, and providing low flow rates into these chambers so that the delivered fluid does not overwhelm the compliance of the inner ear causing damage leading to hearing loss. The low flow rate delivery of fluid required to avoid hearing damage can be accomplished via micropumps.

1.2. Micropumps in Biological Systems

Micropumps used in biological systems can be categorized by their placement relative to the animal. Figure 1-2 shows three types of micropumps, external devices (a), implantable (b), and wearable (c). External devices are attached only by the cannulae and any wiring required for monitoring the animals. Devices in this class, which includes syringe pumps, are often quite large and have power requirements, which may necessitate that the device be plugged into the building's power supply. One of the main limits of the external devices is that it can reduce the length of time an experiment is run as the animal must be sedated or held during the infusion.

Wearable pumps are still external to the animal but the fluid reservoir, controls, power, and the pump itself are attached to the animal and are either mounted to the head or in a backpack. Recently a self-contained pump for fluid phase delivery to the cochlea of

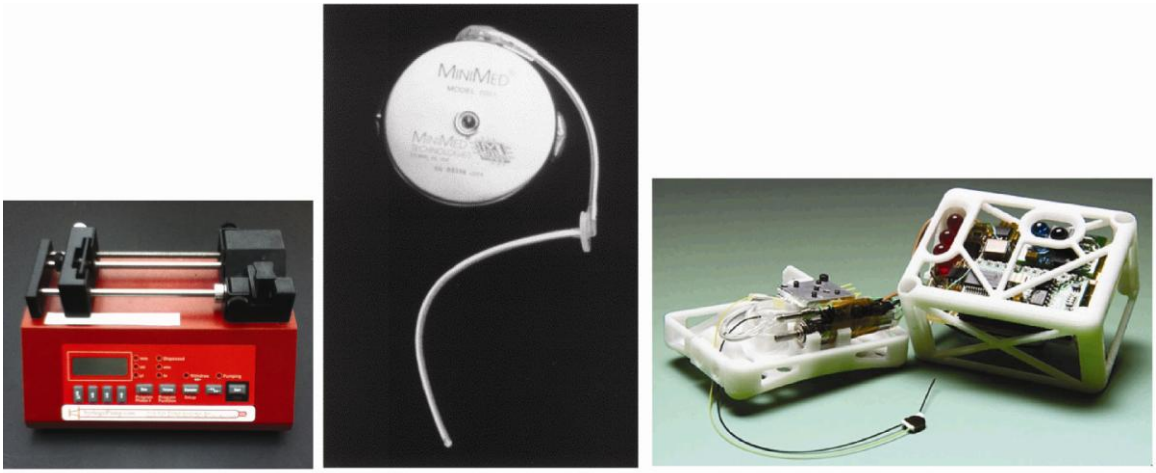

(a) (b) (c)

Figure 1-2: External, wearable, and implantable micropump examples.
(a) Photograph of syringe pump available from New Era (New Era Pump Systems, Inc. Farmingdale, NY)
(b) Implantable insulin pump available from MiniMed (Medtronic, Northridge CA, USA), this device measures 8.1 cm diameter x 1.9 cm thick.
(c) Photograph of wearable device (guinea pig) The device measures 5.5 cm × 4.0 cm × 3.8 cm
(b) and (c) used with permission from Elsevier Limited and Springer

guinea pigs has been developed (Fiering et al., 2009) but the reported size of 83.6 cm^3 is much too large for implantation into mice who are typically less than 10 cm long. The size of this device is even too large for a mouse backpack.

Implantable micropumps are also self-contained with the entire device being implanted *in vivo*, with either subcutaneous or intraperitoneal implantation. In large animals the pump, electronics, and fluid reservoir may be implanted at a single location with drug delivered to the target site through a long cannula. In smaller animals, the reservoir and pump may need to be implanted in separate locations due to size restrictions. In these cases, the sub-systems are connected via cannulae. Implantable micropumps have been used successfully in humans for system wide delivery of a variety of pharmaceutical agents including insulin and other therapeutic compounds (Sefton, 1987).

Implantable pumps approved for human use utilize compressed Freon gas (Abe et al., 1990), osmotic pressure (Eckenhoff, 1981), or solenoids (Carlson, Bair, & Gaona, 1982) for pumping but are too large for use in small animal models (Dash & Cudworth, 1998). Osmotic pumps are commonly used for inner ear drug delivery research.

1.2.1. Use of Implantable Micropumps for Auditory Dysfunction Therapies

Reviews of inner ear drug delivery methods, (Pararas, Borkholder, & Borenstein, 2012; Swan, et al., 2008) report that only osmotic pumps are currently in use for auditory applications. Commercially available osmotic pumps, such as the Alzet osmotic pumps (DURECT Corporation**,** Cupertino, CA) have been used widely in murine research. The principle by which osmotic pumps work is straight forward, therefore the pumps can be simple. A concentration of sodium chloride inside the pump's semipermeable outer membrane pulls fluid into the device causing it to expand. This in turn pressurizes an inner flexible reservoir pushing fluid

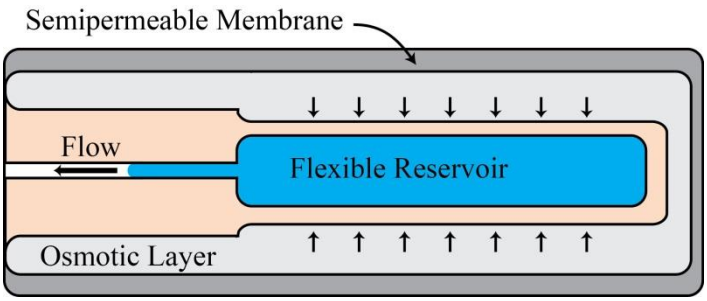

Figure 1-3: Diagram of commercially available implantable osmotic micropump.
Water is drawn though the semipermeable outer membrane by the sodium chloride filled osmotic layer, which swells and compresses the flexible reservoir forcing the fluid through a flow modulator (not shown). Adapted from (Alzet, 2013)

out of the pump through a flow moderator to the delivery portal (see Figure 1-3). Implantable osmotic pumps have two major shortcomings: they are single use devices and cannot be refilled, and the manufacturer sets their pump rate. These single use devices provide a fixed flow rate over a known duration, and lack user-control of the pump rate. As stated above in Section 1.1.1, development of disease treatments requires controlled dose profiles; therefore osmotic pumps will be of limited utility. External devices will also have limited utility due to the restrictions on the length of the experiments and wearable devices currently in use are still too large for use with the mouse model. Since no current implantable pump meets the requirements for subcutaneous implantation in the mouse model for variable rate chronic experimentation, a new micropump is needed to meet this unique set of criteria.

1.2.2. Types of Micropumps

Micropumps can be divided into two groups based on the means of transferring momentum to the pumped fluid: mechanical displacement and dynamic (non-mechanical). Mechanical displacement pumps transfer momentum to the fluid with a periodic change of the volume in a fluid filled chamber while dynamic pumps act on the fluid directly relying on specific properties of the fluid. The momentum transfer in mechanical microelectromechanical systems (MEMS) micropumps can be carried out via deformable diaphragms (Feng & Kim, 2005; Nisar, et al., 2008; Ok Chan & Konishi, 2007), gas boundary (Rahman, et al., 2000), or with rotary motion (Ghalichechian, Modafe, Beyaz, & Ghodssi, 2008; Waldschik & Buttgenbach, 2010).

Diaphragm based pumps consists of an inlet and outlet, a pump chamber covered with a flexible diaphragm, and an actuation mechanism above the diaphragm (see Figure 1-4). Momentum is transferred from the actuation mechanism to the fluid

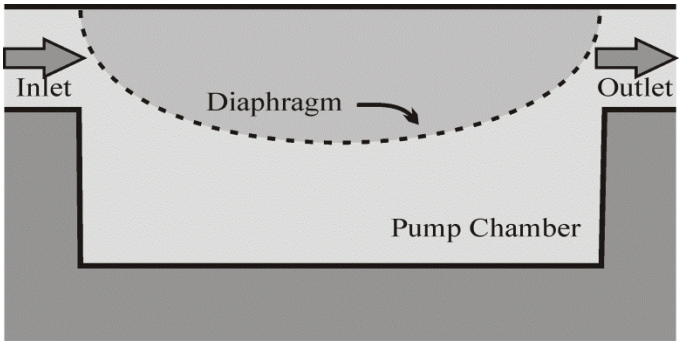

Figure 1-4: Drawing of diaphragm based micropump. Momentum is transferred from the diaphragm to the fluid in the underlying chamber. Valves at inlet and outlet are required to control fluid flow directionality. Adapted from (Nisar, et al., 2008).

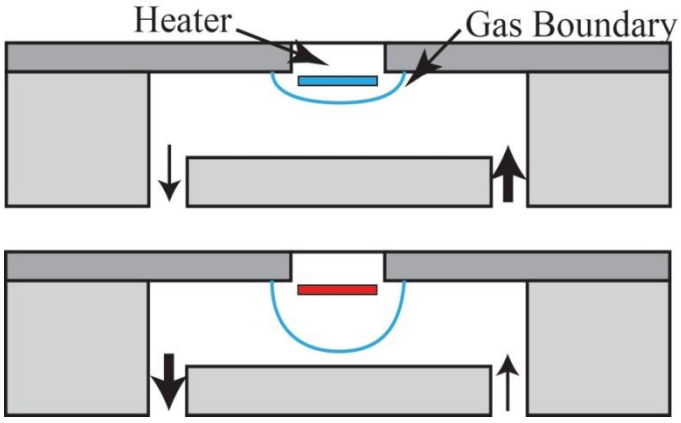

Figure 1-5: Drawing of gas boundary based micropump.
(a) Top figure shows cooled heater, (b) when heated, a gas bubble forms and expands into the pump chamber forcing fluid out. Valves can be used to control the directionality of the flow. Gas boundary based pump. Adapted from (Rahman, Ahmed, Zhao, & Gong, 2000)

in the underlying chamber via the diaphragm. The diaphragms are made to reciprocate to move fluid out of the diaphragm chamber. Valves at inlet and outlet are required to control fluid flow directionality.

Gas boundary based pumps operate in a similar fashion to the diaphragm based pumps in which the diaphragm is replaced with a gas/liquid boundary (see Figure 1-5). A heater above the pump chamber expands a gas bubble into the underlying pump chamber. This moving boundary moves the fluid out to the fluid port. Valves at the inlet and outlet are required to control fluid directionality as in the diaphragm based pumps.

Rotary gear based micropumps consist of two meshing gears, a gear housing with gear hubs, and a fluidic channel directing the fluid to and from the meshing gears (see Figure 1-6). The gears drag fluid along the outer walls of the gear housing pushing it through the pump channel.

Microscale rotary pumps are complex and prone to failure with frictional forces being the limiting factor to their reliability (Meng, Zhang, Huang, Li, & Chen, 2009). Diaphragms offer greater flexibility for the selection of actuation mechanism over gas boundary and rotary pumps and will allow for a less complex fabrication process.

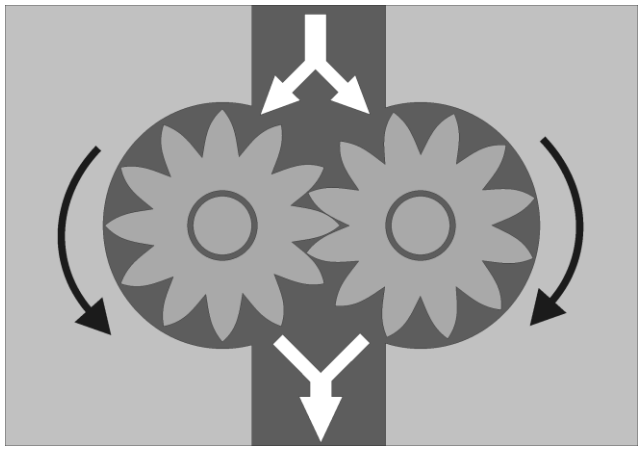

Figure 1-6: Drawing of rotary gear based micropump.
Rotating gear micropumps are difficult to fabricate but are well suited for highly viscous fluids. Adapted from (Waldschik & Buttgenbach, 2010)

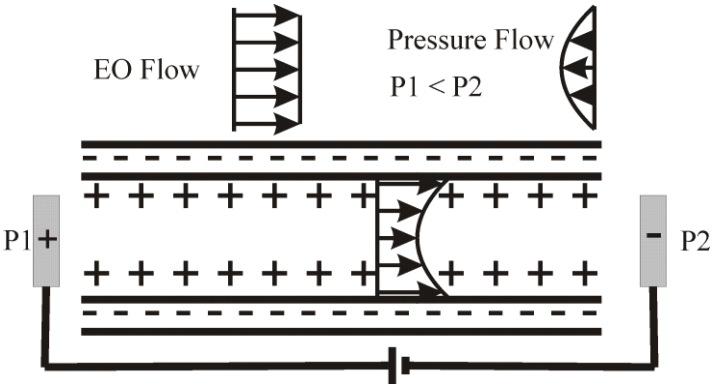

Figure 1-7: Schematic diagram of double charge layer leading to Electro-Osmotic (EO) flow.
The negative ions are drawn to the surface of the channel forming the first layer. The positive ions diffuse towards this layer forming the second layer. The ions in the diffuse layer are motivated by the voltage across the channel, dragging water molecules with them. The velocity of the flow is shaped by the pressure flow, driven by the difference in pressure where P1 < P2. Adapted from (Nan-Chyuan & Sue, 2007)

A variety of dynamic pumps, electrohydrodynamic (EHD) micropumps, have been used for fluid delivery. For example: electrophoretic (L. Chen, Lee, Choo, & Lee, 2008); electrolytic (Daniel A. Ateya, Ashish A. Shah, & Susan Z. Hua, 2004); electro-osmotic (Prakash, Grissom, Rahn, & Zydney, 2006; Seibel, Scholer, Schafer, & Bohm, 2008); and EHD injection pumps, utilizing ion-drag pumping, (C.-L. Chen et al., 2007) have been presented.

Electoosmotic pumps rely on the effects of a double charge layer in the microchannels (see Figure 1-7). Negative ions are drawn to the channel surface forming the inner layer and positive ions in the fluid diffuse towards the negative charge forming the diffuse layer. A voltage applied along the length of the channel moves the ions in the diffuse layer from the anion to the cation dragging bulk liquid by viscous forces.

Electrohydrodynamic ion-drag pumps consist of pairs of permeable electrodes (emitter/collector) in contact with the fluid to be pumped. Electrons are emitted from one electrode dragging the fluid via frictional forces. The pumping force of the device can be increased with repeated patterns of emitter/collector electrodes along the wall of the channel (see Figure 1-8).

These dynamic actuators place specific requirements on the pumped fluid and therefore are not often used in drug delivery systems where these conditions cannot be met. For example, electrohydrodynamic (EHD) pumps; electrophoretic (L. Chen, et al., 2008), electrolytic (D. A. Ateya, A. A. Shah, & S. Z. Hua, 2004), and electro-osmotic (Prakash, et al., 2006) require the use of dielectric liquids. This puts a severe restriction on the compounds the pump is capable of delivering. EHD injection pumps require fluids with

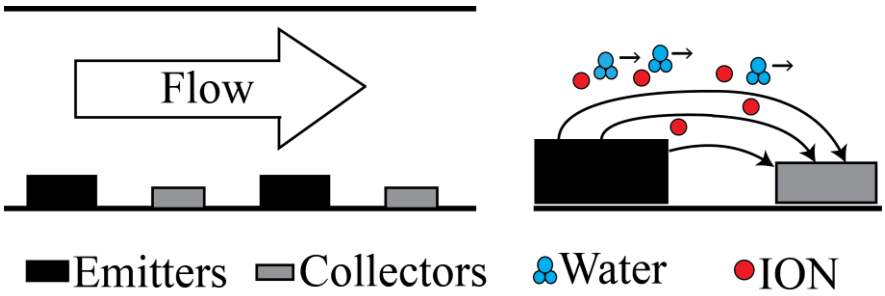

Figure 1-8: Schematic Diagram of an electrohydrodynamic (EHD) pump.
Pairs of permeable electrodes (emitter/collector) in contact with the fluid emit fluid from one electrode dragging the fluid via frictional forces. Multiple pairs of emitter/collector electrodes along the wall of the channel increase flow capabilities.

specific permittivity and conductivity (C.-L. Chen, et al., 2007), which again limits the delivered fluids.

Since dynamic actuators restrict the materials that may be pumped, only mechanical pumps will be considered. Of the mechanical pumps discussed, diaphragm, gas boundary, and rotary, diaphragm offers the most options for low-complexity construction; therefore a diaphragm pump will be used for fluid motivation for this implantable micropump.

1.2.3. Material Selection for Implantable Micropump Components

The basic elements of the presented micropump are the cannulae, cannula stops, flow channels, pump chambers and diaphragms, actuation unit, and the substrate. The function of these elements needs to be considered when determining the material to use for constructing each. Some elements require flexibility, some need rigidity, some the ability to be formed in a complimentary metal-oxide semiconductor (CMOS) like process, some by molding.

All material chosen for an implantable system must either be biocompatible or it has to be isolated from the biological system. Rather than test the micropump for biocompatibility, the presented microsystem achieves biocompatibility by using only biocompatible materials where there is contact between the biological system and the device. Many materials are already classified as biocompatible, so choosing these materials is an obvious first step for an implantable micropump. These include polyimide, Silastic®, and Parylene C. Materials that may have issues with biocompatibility and are therefore candidates for encapsulation in other biocompatible materials include UV-curable resin, silicon, and aluminum.

Cannulae are biocompatible flexible tubing strong enough to resist kinking. Polyimides are high temperature engineering polymers developed by DuPont. Compared to most other organic or polymeric materials, polyimides exhibit an exceptional combination of thermal stability (>500°C), mechanical toughness, and chemical resistance. They can be used for fluidic interconnects between modules, cannulae for intracochlear infusions, stress buffers, and are commercially available as micro-tubing (Microlumen, Tampa, FL).

Cannula insertion stops need to be formed around the end of the polyimide tubing with a biocompatible material. Silastic®, Medical Grade Elastomer MDX4-4210, is a moldable two-part silicone with a tensile strength of 650 psi. Silastic® is easily mouldable to fit many needs. Probes have used Silastic® to bundle and insulate electrodes to deliver charge to cochlear neurons (Richardson et al., 2009). Polymers have also been formed using injection molding techniques for porous implants (Hongbin, Krampe, Schlicht, & Wintermantel, 2009).

Parylene C (chlorinated poly-para-xylylene) can provide a pseudo-conformal, pin-hole free coating. It coats in a near conformal manner due to its long mean free path (MFP) ~1 mm (Mori & Mizutani, 1992). This makes it a good encapsulation material and there are available adhesion promoters and inhibitors so it can be made to adhere selectively.

The substrate for the micropump needs to be easily engineered and machined through common CMOS/MEMS processes. Silicon meets these requirements and can be used unencapsulated without fear of contamination.

1.3. Objectives

The commercially available osmotic pumps are limited to use for one-time infusions at constant rate set by the manufacturer. The smallest of the Alzet pumps recommended for use in the mouse model has an implant volume of 500 mm^3. The size of the presented pump with actuation, therefore, was constrained to less than 500 mm^3.

Pump rate and backpressure requirements were taken from those used in the literature. (Z. Chen, Mikulec, McKenna, Sewell, & Kujawa, 2006) reported an infusion rate of 1 µL/hour (16 nL/min) to the cochlea in the mouse via a basal turn cochleostomy. (Borkholder, 2008) reported infusion rates of 16 nL/min and 32 nL/min via basal turn cochleostomy and canalostomy with limited impact on cochlear function. The

endolymphatic pressure in guinea pigs of 2.5 mm Hg to 4 mm Hg (0.33 kPa to 0.53 kPa) (Inamoto, Miyashita, Akiyama, Mori, & Mori, 2009) was used as an estimate for the pressure in the mouse model cochlea (no measurements have been done to date in mice).

At a minimum, therefore, the pump will need to be able to pump against the 0.53 kPa of backpressure plus the pressure drop in the fluidic system at a rate between 1 nL/min and 100 nL/min. The diaphragm and pump chamber dimensions were designed for low-flow-rate pumping (1 nL/min to 100 nL/min) against a backpressure of 5 kPa (to allow for pumping in other biological systems). An implantable, variable flow micropump platform has been developed, using MEMs technologies, specifically for intracochlear drug delivery in the mouse model for deafness therapy research. This micropump will enable chronic, calibrated delivery of therapeutic agents that is not possible with existing pump technologies. Needs for this application diverge from those commonly pursued in MEMS based micropumps, specifically: accurate delivery of therapeutic agents at nL/min flow rates; interface to target biological structures; a non-reactive, non-water absorbing, biocompatible flow path; and system form factor consistent with subcutaneous implantation in mice. Implantation requires low power, low-voltage to protect the animal in cases of insulation failure. Table 1-1 lists the design targets that will enable the creation of this micropump.

Figure 1-9 is a conceptual drawing of an implantable system incorporating these technologies. To address these unique requirements, several key integration technologies have been developed: low-volume in-plane fluidic interconnects (Chapter 2), micro-molded cannula stops (Chapter 2), flow control (Chapter 3), *in situ* pump diaphragm formation over Parylene C coated fluidic micro chambers and channels (Chapter 4), and integration of a low voltage, low-power actuation mechanism (Chapter 5). The final chapter discusses pump integration, testing, and future work.

Table 1-1: Implantable Micropump Design Targets

Characteristic	Design Target for Presented Micropump
Device volume	< 500 mm^3
Flow rate range	1 nL/min to 100 nL/min.
Back pressure	5 kPa
Form factor	Planar

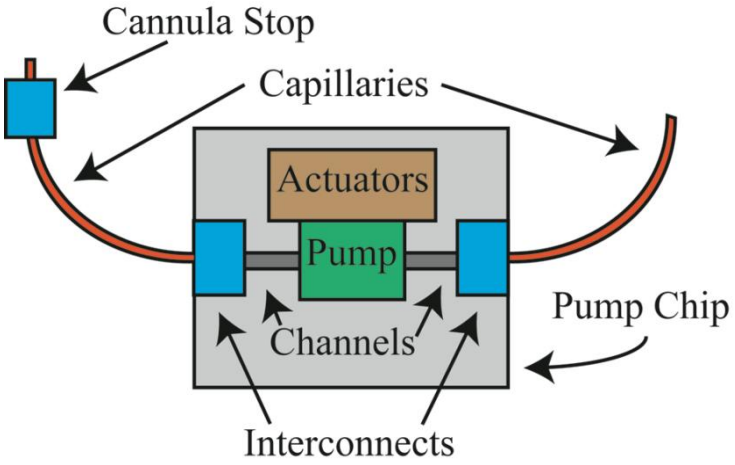

Figure 1-9: Schematic of a four-chamber peristaltic pump concept.

Integration of cannula stops, interconnects, microfluidic channels, micropump, and actuation mechanism will be described in this work. Pump chip designed to be $< 500\ mm^3$.

Chapter 2 Fluidic Interconnects

> *Civilization grew in the beginning from the minute that we had communication -- particularly communication by sea that enabled people to get inspiration and ideas from each other and to exchange basic raw materials.*
>
> *Thor Heyerdahl*

Implantable microfluidic systems for inner ear dysfunction therapy research require fluidic coupling to the inner ear. For the pump technologies being considered here, there are two varieties of interconnects. The first is the interconnect to the implantable microsystem via a cannula and the second is the interconnect of the cannula to the murine cochlea or other targeted biological system.

2.1. In-Plane Biocompatible Microfluidic Interconnects for Implantable Microsystems

In space-constrained applications such as implantation into the human mastoid cavity, or subcutaneous implantation in small animals, the form factor and volume of the fluidic interconnects is of critical importance. Coupling to microfluidic systems is generally achieved with fluidic ports formed with hard polymers, metal, or silicon or by coupling into soft polymers like polydimethylsiloxane (PDMS).

Examples of silicon and hard polymers are described by (Gray, et al., 1999) who present interconnect technologies using deep reactive ion etching (DRIE) of silicon along with silicon fusion bonding (SFB) and anodic bonding to create multilevel fluidic chips. The process utilized a stack of three silicon wafers and an additional glass layer (see Figure 2-1). The top wafer was patterned with DRIE and bonded to a second wafer, which was ground and etched. The bottom wafer is patterned with both DRIE and surface

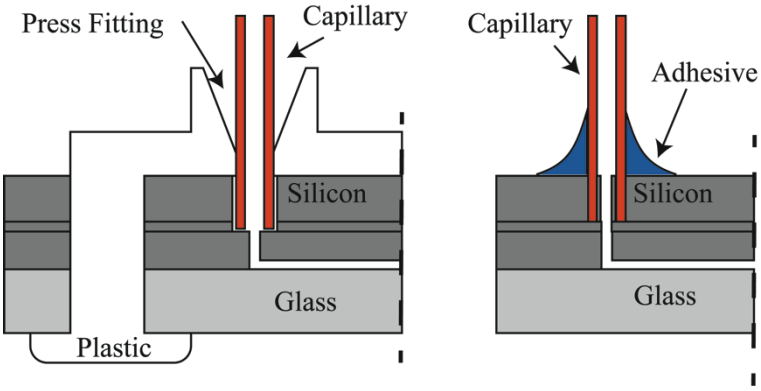

Figure 2-1: Out-of-plane fluidic interconnects formed with deep reactive ion etching.
Top wafer is patterned with DRIE, SFB to second wafer, which is then ground and etched, a final SFB and DRIE are performed on the bottom wafer. Anodic bonding of a glass layer on the bottom forms the fluidic channels. Adapted from (Gray et al., 1999)

micromachining before a final SFB. A layer of glass is anodically bonded to the bottom wafer forming the microfluidic channels. The capillary tubing, out-of-plane, is held in place with either a plastic press fitting or by the use of adhesive.

(Puntambekar & Ahn, 2002) presented a press-in out-of-plane interconnect with three layers of glass (see Figure 2-2). Two layers of drilled glass are bonded together using direct glass-glass fusion bonding. A third etched glass layer is bonded to form microchannels. The device was heated to 583K (310 ºC), Teflon® tubing pressed into the drilled interconnect, with a solid insert keeping the tubing open. The plastic tube spreads into the widened bottom of the inlet hole forming a flange. Other examples of fluidic ports formed with hard polymers, metal, or silicon include those presented by (Gonzalez, Collins, & Smith, 1997a; Korivi & Li, 2007a; Tingrui, Baldi, & Ziaie, 2006).

Soft polymer interconnects using similar structures have been presented by (Christensen, Chang-Yen, & Gale, 2005; Shifeng & Shaochen, 2003) (see Figure 2-3). Holes are punched vertically or horizontally into a layer of PDMS with a punch of the same diameter as the tubing to be held. The diameter of the punched hole is smaller than the punch due to the flexibility of the PDMS such that the tubing is held in place.

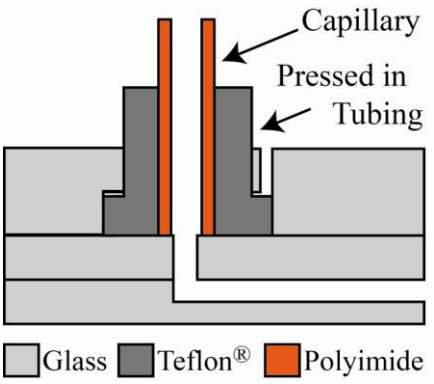

Figure 2-2: Press-in interconnect with three glass layers.
Direct glass-glass fusion bonding is used to form microchannels. Device heated to 310 ºC, Teflon® tubing pressed into etched interconnect, with solid insert keeping its form during pressing. The plastic tube spreads into the widened bottom of the inlet hole (flanged). Adapted from (Puntambekar & Ahn, 2002)

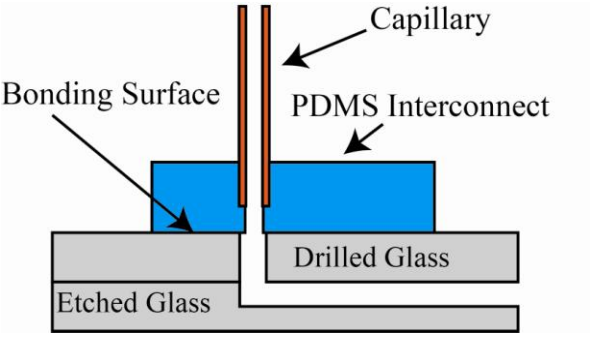

Figure 2-3: Press-in PDMS interconnect.
Two substrate layers form microfluidic channels. Capillary tubing is held in place by the elastic property of the PDMS. Adapted from (Shifeng & Shaochen, 2003)

For medical implant applications, additional coupling structures and out-of-plane approaches add unacceptable volume. In-plane interfaces offer the potential to significantly reduce overall fluidic interconnect volume but often require complex processing (Gonzalez, Collins, & Smith, 1997b) or are incompatible with small diameter tubing (<150 μm OD) (Limited, 2007). Coupling approaches relying on adhesives (epoxies and elastomers) can result in either blocked capillaries (Gray, et al., 1999) or gap formation and dead volumes depending on the material viscosity and gap widths.

Existing microfluidic interconnect technologies fail to reliably meet the combined space and biocompatibility requirements of implantable microsystems that are needed for many clinical applications and for use in small animal model systems such as mice. A method for coupling fine capillary tubing to microfluidic channels is needed to provide low-volume biocompatible interconnects exiting in-plane with the pump.

Here a robust interconnect technology is presented requiring only a single mask level and deposition of Parylene C (chlorinated poly-para-xylylene) onto room temperature surfaces to capture small diameter capillary tubing. Parylene C provides the requisite controlled deposition of a sealing material into the small spaces between the capillary and microfluidic channel. It is an attractive material for biomedical fluidic interconnects due to its biocompatibility and chemical resistance (Licari, 2003). Parylene C has been used for conformal coating (Cosens, 1983), pore-filling (Cale, Bae, Jezewski, & Senkevich), microchannel formation (Hong-Seok, Yong, & Hesketh, 2004), and channel penetration (Broer & Luijks, 1981; Grytsenko & Tolstopyatov). Polyimide, USP Class VI compliant, has been used for implants as medical probes (Metz, Bertzch, Bertrand, & Renaud, 2004), and microchannels (Lacour et al., 2008) and is well suited as small diameter tubing for use as cannulae (Komaromy, Varner, de Juan, Acland, & Aguirre, 2006) in the implanted

microsystems targeted in this work. This section presents the interconnect concept, modeling, fabrication, and testing with emphasis on added interconnect volume, dead volume, resistance to leakage from internal pressure, and robustness to applied force on the extending capillary. Characterization of Parylene C deposition into channels was used in conjunction with equations describing molecular flow and diffusion to spatially model monomer concentration and polymer deposition within tapered channels. This model, implemented in MATLAB, permitted rapid optimization of channel geometries for full gap filling without voids at the tubing / channel interface. This approach was significantly faster and less computationally intensive than the traditional Monte-Carlo simulations to predict Parylene penetration into trenches and crevices (Bowie & Zhao, 2004; McVittie et al., 1991; Tolstopyatov, Yang, & Kim, 2002).

Device fabrication is described with testing on several designs bracketing the predicted optimum channel dimensions. Testing includes measurement of deposited Parylene C and void characterization along the length of the interconnects, burst / leakage pressure, and pull-strength. These results, along with overall interconnect volume, dead volume, and fabrication complexity, are compared against commercial and other research devices.

2.1.1. Interconnect Concept

The microfluidic interface consists of capillary tubing inserted in-plane into the widened end of an on-chip microchannel. The tubing is held in place with a deposition of Parylene C, which polymerizes into the space between the capillary tubing and the microchannel and effectively secures the tubing. The gap between the capillary and the microchannel walls is designed to be tapered such that the entire gap will be filled with the polymer before occluding. The entire device is simultaneously encapsulated in Parylene C, enhancing device biocompatibility. Figure 2-4 is an illustrative diagram of the interconnect concept showing the capillary tubing coupled directly to a microchannel in a glass-covered silicon wafer. The long mean-free path of Parylene C during deposition (20 °C, 42 mtorr) allows penetration into micro-gaps resulting in a pseudo-conformal coating with deposition thickness decreasing with depth inside the micro-gaps (Broer & Luijks, 1981; Ramachandran, Junk, Koch, & Hoffmann, 2007). The channel shape was designed to leverage this effect such that the narrow region at the tip of the inserted tubing would occlude first during deposition to provide a fluidic seal and reduce

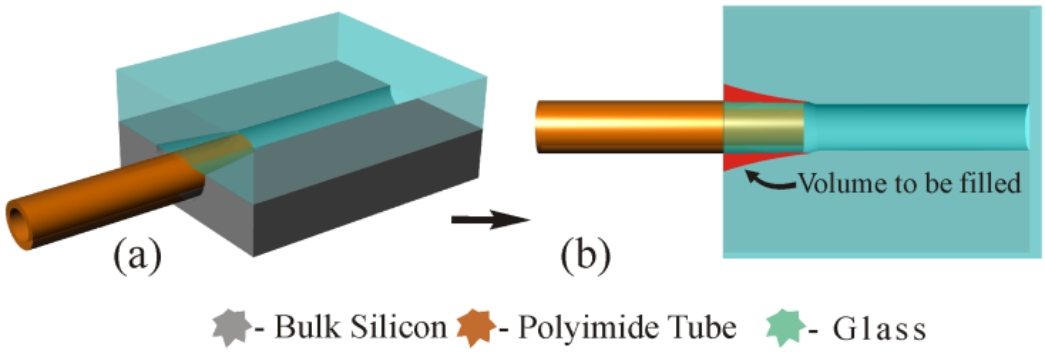

Figure 2-4: In-plane fluidic interconnect concept.
(a) 140 µm OD polyimide tubing is inserted 500 µm into tapered channel end, 215 µm wide at opening. (b) Top view showing designed gap taper in red. Parylene C will fill this gap while encapsulating the entire device. not drawn to scale.

the potential for dead volumes. Continued Parylene C deposition filled the space between the capillary tubing and the microchannel, effectively securing the tubing in place. A model of this polymerizing deposition was created to design the interconnect channels with optimal width and taper for complete fill without creation of voids and dead volumes.

Figure 2-5 is a drawing of capillary tubing inserted 500 µm into the channel and shows the two types of voids that may occur with this design. The first (void type 1) results from a channel taper that is too broad and occludes at the tubing/microchannel interface leaving a void at the channel entrance. This void is not in contact with the fluid flow path and would not contribute to dead volume, but could affect pull-strength or burst tests. The second (void type 2) results from a channel taper that is too narrow and occludes at the channel entrance resulting in dead volume at the

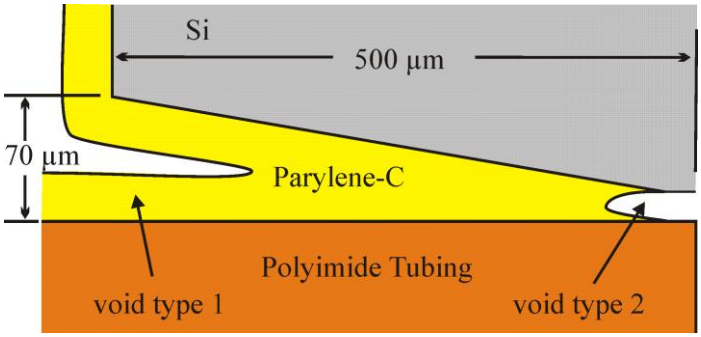

Figure 2-5: Potential voids resulting from Parylene C deposition.
Gap between polyimide tubing and Si microchannel provides an opportunity for void formation. Voids of type 1 result from a taper angle that is too large and requires additional polymer deposition. Voids of type 2 result from a taper angle that is too small and creates dead volume. The 70-µm gap between the channel wall and the tube at the channel entrance is typical for the interconnects.

tubing/microchannel interface. Dead volume is a concern for implantable microfluidic systems for drug delivery where precise measurement of delivered fluids is important and fluid exchange may be required. Unswept volumes, areas of stagnation within the flow path, are not as critical as dead volume for these applications and fabricated interconnects.

This simple processing method can provide a low volume, low dead volume interconnection between the capillary tubing and the microchannel while encapsulating the entire device with a biocompatible, chemical resistant material. Unswept volumes are minimal, being dictated by the wall thickness of the capillary tubing.

Two types of devices were created to develop and verify the deposition model. The first were characterization devices used to test very narrow straight channels and consisted of glass and silicon that were fabricated with isotropically etched constant width channels (50 µm). The glass and Si were clamped together to enable easy separation for deposition thickness measurement. The deposition of Parylene C into these narrow constant-width channels was characterized to gain an understanding of the deposition profile and used to develop a heuristic model.

The Parylene C was deposited into the narrow characterization channels, using a deposition system fabricated locally at Rochester Institute of Technology (see Figure 2-6), the silicon and glass were separated, and the thickness of the deposited polymer was measured with a profilometer. Characterization of Parylene C channel penetration (see Figure 2-7) demonstrated a reduction in deposition thickness with depth into the channel consistent with results presented by (Broer & Luijks, 1981) for 56-µm channels. This initial characterization data indicated that constant width channels would not be completely filled with polymer, and that channels with tapered ends would need to be designed to facilitate tubing capture and gap occlusion. The second device type contained tapered channels that more closely mimicked the geometry of the interconnects (described in detail in Section 2.1.1).

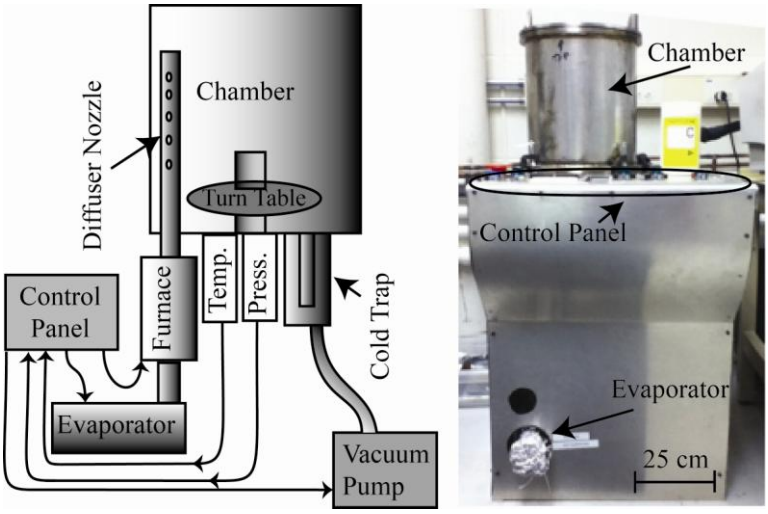

Figure 2-6: Schematic and photograph of Parylene deposition tool. Parylene C dimer (loaded into the evaporator) is evaporated (at up to 175 °C) into the furnace where it is cracked into monomers. The monomer flows into the room temperature deposition chamber. Pressure is maintained during deposition by controlling the heat of the evaporator, increasing the temperature when the chamber pressure drops and lowering the temperature when pressure becomes too high.

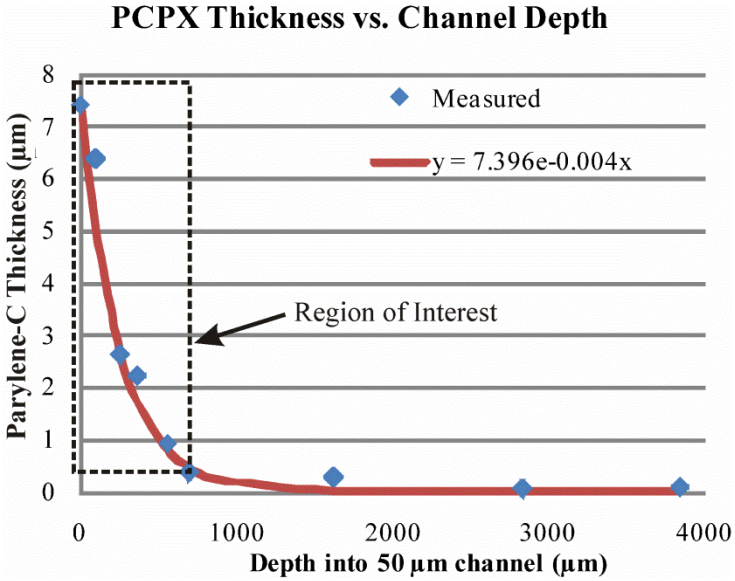

Figure 2-7: Measured thickness of Parylene C along the 50-µm wide channel.
Shown with exponential curve fit $y = 7.396 \times 10^{-0.004} x$

2.1.2. Parylene C Deposition Model

A model was developed to simulate the deposition of the Parylene C inside the tapered channels. The behavior of the Parylene C monomers is dependent on the type of interactions within the interconnect gap as shown in Figure 2-8. The monomers can (a) interact with other monomers or (b) with the gap walls. They can adsorb directly on the channel walls, (c) polymerize to an existing polymer at the adsorption site, or (d) continue to migrate along the surface until they arrive at another polymerization site. The sticking coefficient, $1/N$, is the probability that a monomer striking the wall will lead to adsorption, where N is the average number of wall strikes a monomer experiences before being permanently adsorbed.

The governing equations for polymer deposition in tapered channels will depend on the transport regime of monomers in the system. The Knudsen number, which is the ratio of the mean free path to the characteristic length in the system, characterizes the monomer transport as shown in Table 2-1. For low Knudsen numbers, the mean free path of the monomer is much smaller than the dimensions of the system and intermolecular interactions predominate. High Knudsen numbers indicate wall / molecule interactions will predominate. In this work, the characteristic length is defined by the width of the gaps around the polyimide tubing. The mean free path, calculated using (2-1) and the

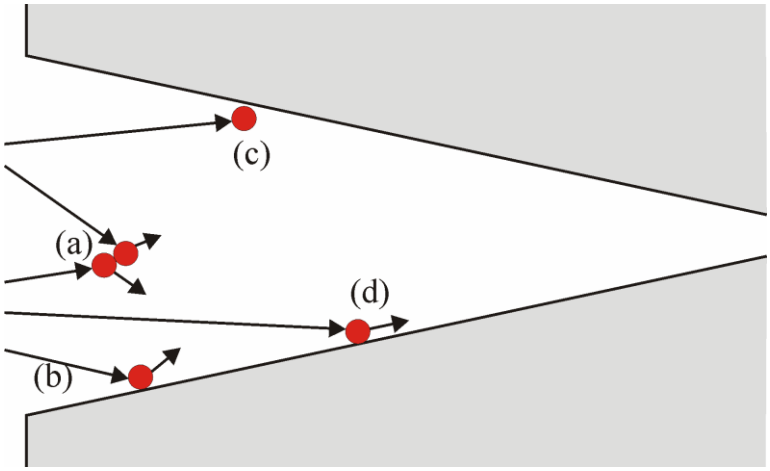

Figure 2-8: Diagram of different molecular interactions within a tapered channel.
(a) Monomer-monomer interaction (b) Monomer-wall interaction, not adsorbed (c) Monomer-wall interaction, adsorbed. (d) Monomer-wall interaction, surface migration

Table 2-1: Flow Regimes

Knudsen Number	Regime
$Kn < 0.01$	Continuum Flow
$0.01 < Kn < 0.1$	Slip Flow
$0.1 < Kn < 3$	Superposition of Viscous Flow and Molecular Flow
$Kn >> 3$	Molecular Flow

Adapted from (Tolstopyatov, et al., 2002)

parameters for this deposition configuration in Table 2-2, is 1.47 mm.

(2-1)

The openings in this work are less than 100 µm, Kn > 14.7, therefore the transport of the Parylene C monomer is in the free molecular regime, Knudsen flow, where intermolecular collisions may be ignored. This result agrees with the work by (Broer & Luijks, 1981), which states that the deposition due to molecular flow dominates that of viscous flow for a system of similar dimensions and pressures. The long mean free path of Parylene C at the deposition pressure of 42 mtorr (10 mtorr Parylene C partial pressure) makes interactions between molecules a rare event and does not affect the deposition equations. This, along with a low-sticking coefficient, allows the monomers to penetrate deeply into the channels before adsorbing onto the walls.

The spaces between the capillary tubing and the hemispherical microchannels are roughly triangular as seen in Figure 2-9 and the deposition is modeled as a one dimensional diffusion problem. A diffusion coefficient is calculated using the same form factor as a Knudsen coefficient (2-2) with an empirical fitting coefficient, *B*, determined

Table 2-2: Parameters used to determine the mean free path, the Diffusion Constant, Flux, and C_0

Symbol	Quantity	Value/Units
k_b	Boltzmann constant	1.38E-23 J/K
T	Temperature	473 K [*]
P_m	Pressure	5.6 Pa (42 mtorr)
D	Diameter of monomer	7.5E-10 m (0.75 nm) [†]
R	Universal gas constant	8.3145 J/mol K
M	Molecular weight of monomer	137.59 kg/kmol [‡]
m	Weight of a single monomer	1.38×10^{-25} kg [‡]
P_P	Partial pressure of Parylene C	10 mtorr

[*] Temperature of gas in deposition chamber (surface temperature is 293 K)
[†] Approximated by using the largest reported diameter of Benzene (Gulley & Buckman, 1999), the basis of all Parylenes
[‡] (Specialty Coating Systems, Indianapolis, Indiana)

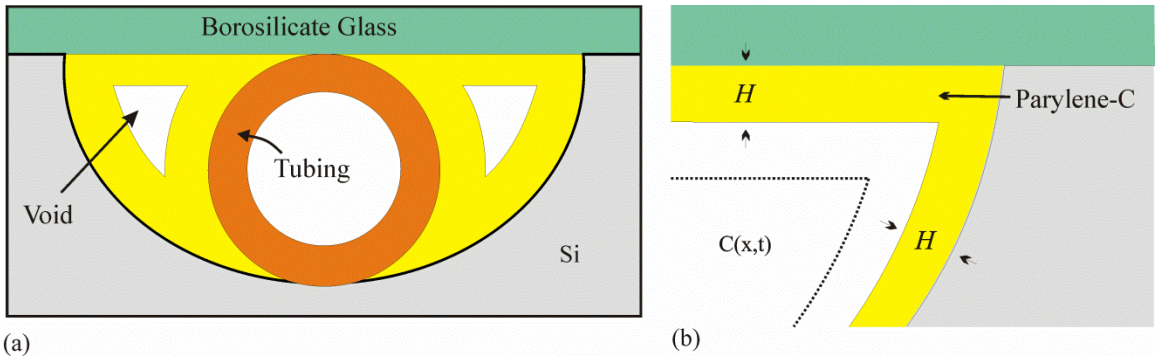

Figure 2-9: Drawing of cross-section (edge view) of characterization device.
Figure shows the channel and Parylene C. First order one-dimensional model uses the Parylene C monomer concentration, *C(x, t)*, to determine the deposition thickness, *H(x)*, along the channel axis. (b) Deposited film thickness, *H(x)*, is equal on all surfaces for a given depth into the channel. Continued deposition increases film thickness as shown by the dotted line.

experimentally. This allows predictions for similar geometries under varying conditions.

$$D = B\sqrt{\frac{8RT}{\rho M}} \tag{2-2}$$

The derivation of the equation for the concentration along the length of the channel, *C(x, t)*, is a straightforward application of Fickian diffusion as in (2-3), which defines how the monomers travel along the gap.

$$\frac{\partial C(x,t)}{\partial t} = -D\frac{\partial^2 C(x,t)}{\partial x^2} \tag{2-3}$$

The initial conditions (@ $x = 0$, $C = C_0$; @ $x = L$, $\partial C/\partial x = 0$; @ $t = 0$, $C = 0$) are used to derive the formula for the concentration along the channel, $C(x)$ in (2-4).

$$C(x,t) = C_0 - \frac{C_0 4}{\pi}\sum_{n=0}^{\infty}\frac{e^{-D(2n+1)^2\frac{\pi^2}{4L^2}t}\sin\left(\frac{(2n+1)\pi}{2L}x\right)}{(2n+1)} \tag{2-4}$$

$$\Psi(x,t) = C(x,t)\sqrt{\frac{k_B T}{2\pi\mu}} \tag{2-5}$$

The monomer flux into the walls, $\Psi(x, t)$, shown in (2-5), is based on an approximation using a homogeneous Maxwell distribution for the particle velocity distribution function (Ramachandran, et al., 2007).

The number of monomers striking the wall in time τ per unit area, M_{SA}, is shown in (2-6).

$$M_{SA}(x,t) = \int_0^{\tau} \Psi(x,t)dt = \int_0^{\tau} C(x,t)dt\sqrt{\frac{k_B T}{2\pi\mu}} \tag{2-6}$$

Multiplying (2-6) by the surface area of the channel walls at *x*, $Pt \cdot dx$, provides the total number of monomers striking the channel walls, M_S, as in (2-7), where *Pt* is the perimeter of the triangular cross-section.

$$M_S(x) = Ptdx\int_0^{\tau} C(x)dt\sqrt{\frac{k_B T}{2\pi\mu}} \tag{2-7}$$

The sticking coefficient, 1/*N*, determines the deposition of the monomers that strike the walls. This has been reported to be from (10^{-4} to 10^{-5}) (Bowie & Zhao, 2004) or (10^{-3} -10^{4}) (Tolstopyatov, et al., 2002). After the model was developed, the sticking coefficient was adjusted to match the measured deposition profile ($1/N = 2\text{x}10^{-5}$). The number of monomers striking the wall (2-7) was multiplied by the sticking coefficient, 1/*N*, to determine the number of monomers adsorbed by wall segment *dx* in time τ, as shown in (2-8).

$$M_D(x) = \frac{Ptdx}{N}\int_0^{\tau} C(x)dt\sqrt{\frac{k_B T}{2\pi\mu}} \tag{2-8}$$

The deposited film thickness, *H(x)*, can be derived from the density of the monomers in the film, ρ, the surface area of the wall, $Pt \cdot dx$, and the number of deposited monomers, $M_D(x)$, as in (2-9).

$$H(x) = M_D(x)\frac{\mu}{\rho Ptdx} \tag{2-9}$$

Substituting (2-8) into (2-9) leads to (2-10), the equation for the thickness of the Parylene C film, *H*(*x*).

$$H(x) = \frac{1}{\rho N}\int_0^{\tau} C(x)dt\sqrt{\frac{k_B T\mu}{2\pi}} \tag{2-10}$$

2.1.2.1. Experimental Setup

A simulation was written in MATLAB (MathWorks, Natick, Massachusetts) using (2-4) and a discrete version of (2-9) to model the penetration and polymerization of the Parylene C, into the narrowing spaces used for the presented interconnects. The equation

for the concentration of the monomer at the entrance of the tapered channel can be derived from the ideal gas law and is shown in (2-11).

$$C_0 = \frac{P_P}{RT} \tag{2-11}$$

P_P is the partial pressure of the Parylene C monomer, T is the deposition temperature, and R is the ideal gas constant (see Table 2-2). Using (2-11) and Avogadro's number, the initial concentration at the gap opening is calculated to be $C_0 = 2.04 \times 10^{17}$ monomers/L.

The simulation was used to optimize the width profile of the proposed tapered channel by simulating the deposition of Parylene C into the gap between the channel walls and the polyimide tubing. Figure 2-10 shows the programmatic flow of the discrete MATLAB simulation. The variables and constants used for the deposition simulation are shown in Table 2-3. The simulation was used to optimize the width profile of the proposed tapered channel by simulating the deposition of Parylene C into the gap between the channel walls and the polyimide tubing.

The input to the simulation is an array containing the widths of the space between the polyimide tubing and the channel wall. Intermediate results of the simulation are arrays of the polymer thicknesses and the resulting gap widths along the channel axis. The simulation was run iteratively to refine the intermediate results until the resulting gap widths were all zero. This provides an optimized taper geometry that indicated that the input width profile would fill completely with polymer. The channel profile was then used with the

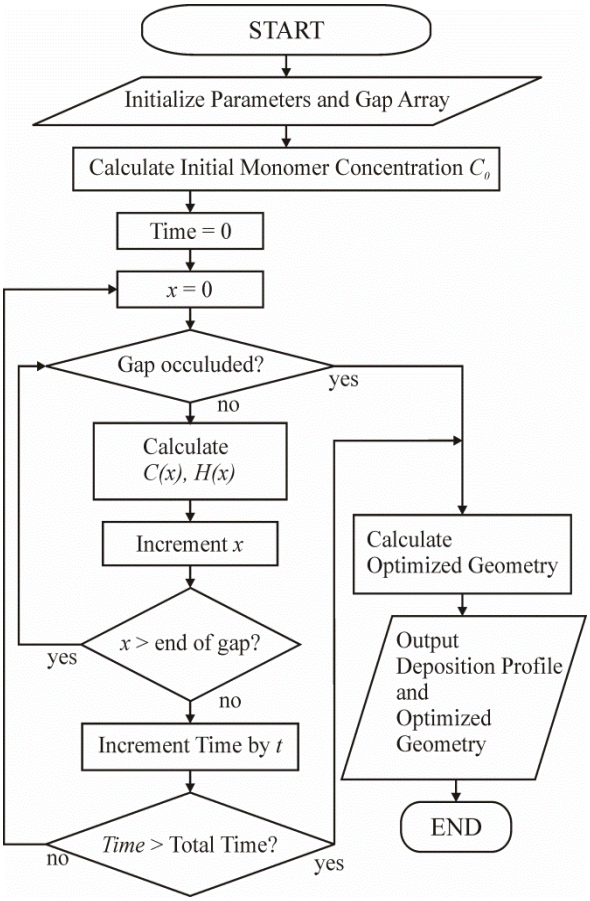

Figure 2-10: Flowchart for the MATLAB simulation of the Parylene C deposition.
Gap occlusion is detected if the deposition at the entrance, $H(x = 0)$, is half of the channel width.

Table 2-3: Simulation Variables and Constants

Symbol	Quantity	Value, Units
C_0	Concentration of monomers at channel entrance	2.04 x10^{17} monomers/L
$C(x, t)$	Concentration of monomers in segment x	monomers/L
$M_D(x, t)$	Monomers deposited in segment x	monomers
$H(x, t)$	Thickness of Parylene C film	µm
D_K	Diffusion Factor	1.13 x10^{-4} cm^2/s
N	Number of wall strikes before adsorption	5.01 x10^4
B	Fitting coefficient	1.33 x10^5

tubing diameter and the isotropy of the Si etch to design the mask for the tapered interconnect channels. The resultant design was used to experimentally verify the model results through characterization of deposited Parylene C volume along the length of the tapered channel.

2.1.3. Test Device Fabrication

Interconnect devices were fabricated as shown in Figure 2-11 for use with polyimide capillary tubing (140 µm OD, Microlumen, Tampa, FL). This creates the tapered gap between the tubing and channel designed by the model to be filled fully with Parylene C. An aluminum hard mask was used to pattern the channels in the surface of the Si with an isotropic etch (Drytek Quad SF_6: 130 sccm, O_2: 10 sccm, Pressure: 30 mtorr, RF power: 130 Watts) to a depth of 140 µm. Once the hard mask was removed in a wet etch, the wafers were diced and treated in a piranha clean. Borofloat glass (Addison Engineering San Jose, CA) was diced, cleaned, and anodically bonded to the silicon substrate to enclose the channels and provide optical access to the interface. The anodic bonding was performed at 1000 VDC (F15, EMCO, Sutter Creek, CA) and 400 °C for 10 min (see

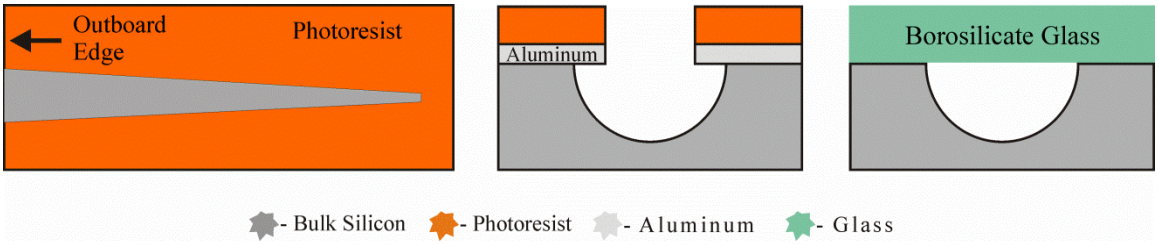

Figure 2-11: Interconnect fabrication process.
(a) Top view showing tapered pattern of photoresist
(b) 0.36-µm Al hard mask used to pattern Si wafer. Isotropic etch in SF_6 and O_2 in Drytek Quad results in an approximately hemispherical microchannel.
(c) The aluminum was removed, the devices were diced and cleaned, and borosilicate glass was anodically bonded to create the channels. © 2011 IEEE Reprinted, with permission, from (Johnson, et al., 2011)

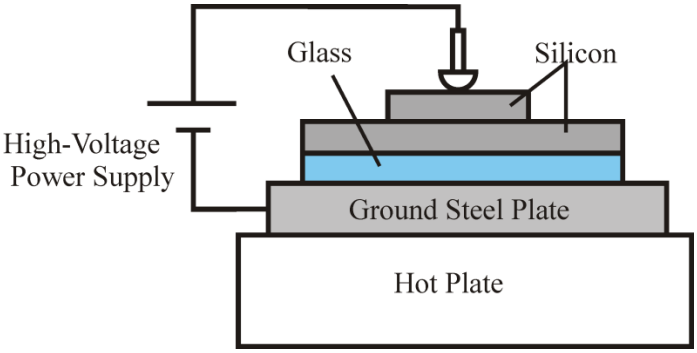

Figure 2-13: Anodic Bonding set-up used to test interconnect devices.
Sodium ions in the borosilicate glass are mobilized by high heat (400 °C). The power supply (400 VDC) moves the ions away from the interface with the Si forcing the materials together by electrostatic force. Oxidation of the Si at the surface forms a chemical bond with the glass.

Figure 2-13). Three designs were produced to bracket the optimized channel width profile provided by the simulation by ±10%, with widths at the opening of 193 µm, 215 µm, and 236 µm. All channels had a length of 500 µm and narrowed to 112 µm to match the ID of the polyimide capillary tubing; having a smaller overall diameter than the tubing assures that the tube will stop against the channel walls during insertion.

Polyimide capillary tubing (140-µm OD) was inserted in-plane until the tubing end interfaced with the channel walls. A fixture set-up was used to keep the tubing aligned in the channel (see Figure 2-12). The free ends of the tubing were covered with Parafilm (Structure Probe, Inc. Westchester, PA) to prevent unwanted Parylene C deposition into the distal end of the tubing. A 40-µm layer of Parylene C was deposited to capture the tubing, create a fluidic seal, and fully encapsulate the device to provide a biocompatible surface suitable for medical implantation.

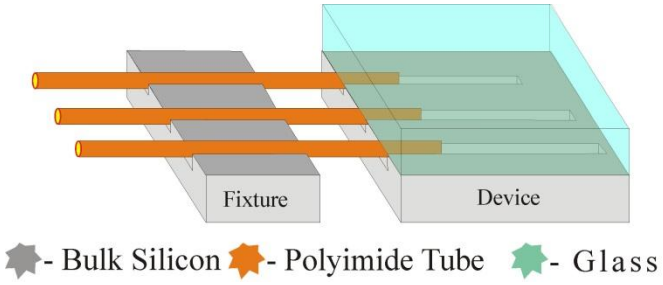

Figure 2-12: Drawing of alignment fixture used to aid insertion.
The silicon fixture is micro-machined simultaneously with the device creating channels in perfect alignment with the microchannels. Fixture is use for the placement of small diameter capillary tubing into microchannels.

2.1.4. Testing

To verify the suitability of the interconnects for the intended purpose, three types of tests were performed. The first is fill percent, an indication of the robustness of the interconnect as well as a test of the effectiveness of the model. The next is a leak/burst pressure test, which measures the fluidic pressure at which the interconnects can operate. Lastly is the pull test, another proof of robustness, which will serve to prevent interconnect failure.

2.1.4.1. Fill Percent and Deposition Thickness

The thickness of the Parylene C deposited within the original gaps was measured by cross sectioning the devices using a MultiPrep™ edge polisher (Allied High Tech Products, Inc., Rancho Dominguez, California USA) and imaging the sections under a microscope. The edge polisher was used, to precisely remove 50 μm of material from the edge of the chip and produced clean images. The images were measured for Parylene C thickness, void area, and original gap width at various depths into the channel. These measurements were used to calculate the percent of the original gap volume filled with Parylene C. Fill percent (*FP*) is calculated from the area of the gap to be filled (*g*) and the void area (*v*), ($FP = (g–v)/g$). Fill percent is a measure of how well the polymer penetrates and fills the gap. This metric is useful for the type of interconnect presented here as these devices rely on the Parylene C to capture the tubing and secure it in the interconnect taper.

A simulation of the deposition into the measured gap width was run to compare with the deposited polymer deposition measurements in tapered channels. The results are all within 1.8% of the predicted values. Devices using polyimide tubing were fabricated and measured for fill percent. The designs for these devices bracketed the optimized design: four interconnects with the optimal geometry, four with 10% wider geometry, and four with 10% narrower-than-optimal geometry. Figure 2-14 is an image of a cross-section of a 10% narrower design 50 μm into the channel showing the areas that were measured, the original gap area (*g*), the void area (*v*), and the thickness of the deposited Parylene C film. The results from the cross-sectioning show that the four optimized and four wide channels filled in 100% with Parylene C, as predicted by the simulation, whereas the four narrow channels had an average fill percent of 97.9 % (σ = 0.7%). The narrowest

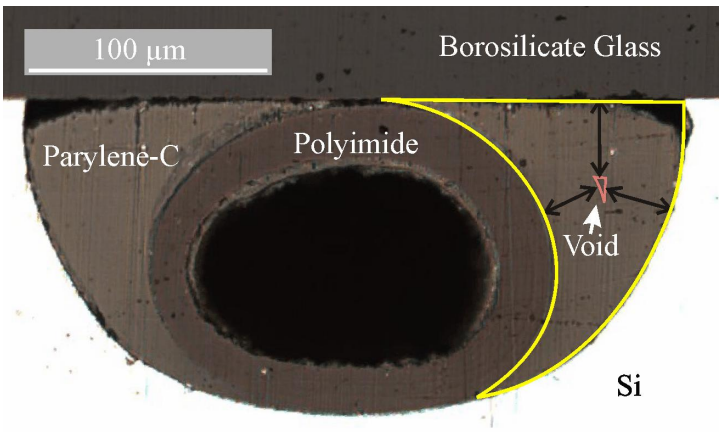

Figure 2-14: Optical image of cross-section of Parylene C deposition into interconnect.
The polymer fills the gap in the channel around polyimide tubing. Original designed gap is outlined in yellow, which has been filled with Parylene C. Void area is outlined in red. Deposited film thickness shown by double pointed arrows. Cross-section 50 µm from edge of the wafer

channels occluded at the opening before filling completely resulting in type 2 voids likely starting near the interior end of the tubing and extending to the middle. The dead volume for the 100% filled, optimized interconnects is zero and the unswept volume is calculated to be 0.0004 mm^3 (0.4 nL).

The calculated unswept volume is the result of the difference between the inner and outer diameters of the tubing and not a result of any voids in the deposited polymer. The volume of the original gaps to be filled and the volume of the voids in the Parylene C were interpolated using the measured area and the thickness of each slice, ~50 µm (see Figure 2-15). The distances from the three sides of the opening are measured to the center of the triangular gap. The three measurements are averaged to arrive at the deposition thickness. For measurements interior to the gap occlusion, the outboard gaps are extrapolated to find a central measuring point. These numbers are also averaged.

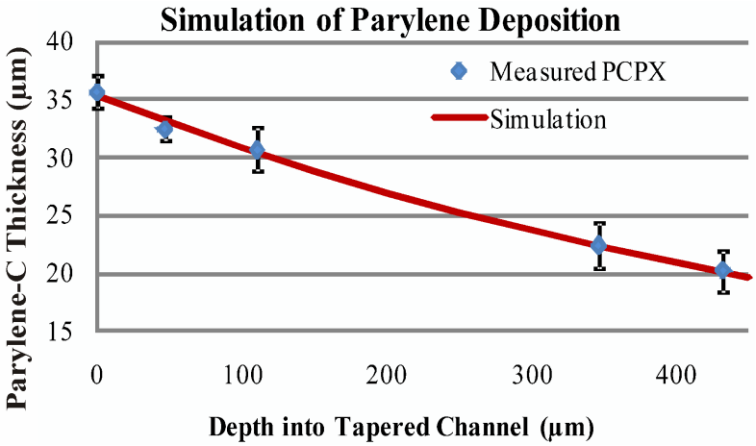

Figure 2-15: Simulation of Parylene C deposition compared to experimental data.
Simulated thickness shows high degree of agreement with measured thickness. Data averaged from six measurements at each cross-section. Error bars ± σ.

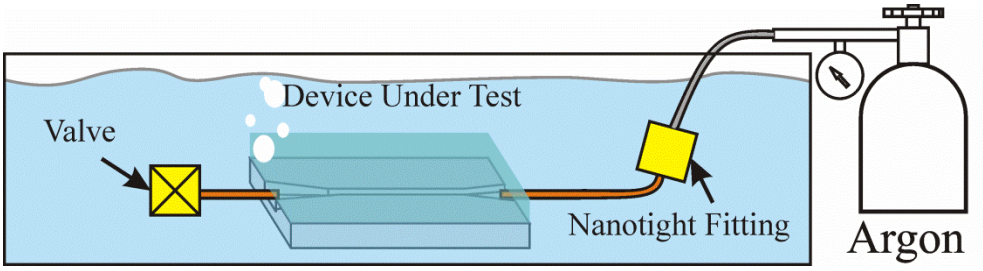

Figure 2-16: Drawings of leak test set-up.
Bubble detection test set-up for flow and leak testing. Pressure was measured with pressure gauge. Device was submerged in water for bubble detection under a microscope. Flow through the device was verified before closing valve at the outlet tube. Pressure was measured as high as 120 psi with no leaks at the interfaces. © 2011 IEEE Reprinted, with permission, from (Johnson, et al., 2011)

2.1.4.1. Leak-Burst Pressure/Leakage Test

The interconnects with 140-µm OD polyimide tubing were connected to the pressure test setup using Nanotight fittings (Upchurch, Scientific, Oak Harbor, WA, USA). One side of the device was connected to compressed argon with a luer connector, while the other side was connected to a valve.

Compressed argon with a maximum pressure of 120 psi was applied to the interconnection (see Figure 2-16). Pressure was measured with a gauge on the gas regulator. The devices were submerged in water and viewed through a microscope to detect air bubbles. The downstream valve was opened to confirm flow through the devices and then closed for pressure testing. Interconnects were tested for leakage and held to the maximum available pressure of 120 psi for all devices (N = 8).

Interconnect volume is the volume added to the device for the interconnect system. Numbers for this metric are not normally reported and have been calculated from the dimensions of the fabricated devices, but do not include the effective added volume of an out-of-plane connection. An order of magnitude improvement was achieved in total interconnect volume over the best out-of-plane designs, with over two orders of magnitude improvement over other in-plane designs. Burst or leak pressure tests measure the maximum internal pressure of air or liquid in the microfluidic system that the interconnect can withstand before failure. If interconnect failure does not occur, then the maximum tested pressure is reported. The pressure performance of the in-plane interconnects exceeded all reported maximum pressures for research devices. Test setup limitations prevented testing to the 435 psi pressures reported for the commercial device.

2.1.4.2. Pull Test

Pull tests with polyimide tubing can be difficult as the tubing can stretch before the interconnect fails. So to facilitate pull-testing, polyimide-coated fused silica capillary tubing (153 µm OD, Polymicro Technologies, Phoenix, Arizona) was used for these devices. Test devices were fabricated as in Section 2.1.3 except channels were over-etched to a depth of 155 µm and a 50-µm layer of Parylene C was deposited to capture the tubing. This created a non-optimal gap geometry not designed to fill completely with Parylene C. A pull-test load cell was designed using a strain gauge (1.5/120-LY11, Omega Engineering Inc., Stamford, CT) in a Wheatstone bridge configuration with weights from 50 g to 500 g used for calibration prior to testing. One gram of mass on earth weighs 0.0098 Newtons: grams are thus converted to Newtons. A micromanipulator was used to pull the polyimide-coated fused silica tubing out of the interconnect channel, while a multi-meter was used to record the strain signal in order to capture the peak force (see Figure 2-17).

The interconnects were subjected to the pull test with an average recorded force of 2.9 N (σ = 0.6 N, max. = 4.1 N, min. = 2.3 N) required to pull the tubing cleanly out of the Parylene C in the interconnect channel. The nature of the observed pull-test failures, where the tubing pulled cleanly from the polymer suggests the failure mechanism is polyimide to Parylene C adhesion. For these interconnects with rigid polyimide-coated fused silica tubing, the average fill percent was 87.5% (σ = 5.7%). These non-optimized channels occluded at the entrance leaving a void at the tube end as a dead volume of

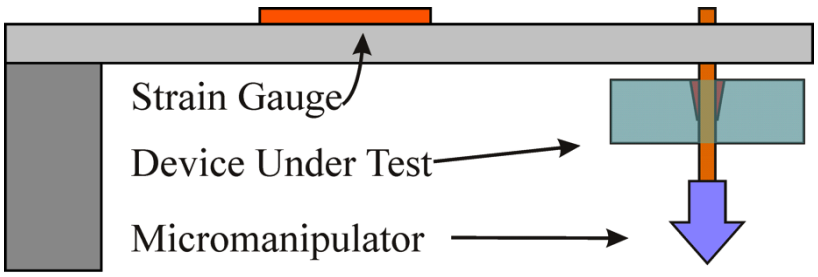

Figure 2-17: Drawings of Pull test set-up.
Pull-test to measure force required to pull tubing from the device. Bending force load cell was calibrated with precision weight set before being used in pull-test.

Table 2-4: Comparison of Microfluidic Interconnect Devices

Materials	Volume* (mm^3)	Max Pressure	Pull Test	Dead Volume mm^3	Fabrication Complexity	In-Plane	Tubing OD (mm)	Ref
Silicon and Epoxy	0.667 †	60 psi	1-2 N	0.002	high	no	0.425	(Gray, et al., 1999)
Flanged Thermoplastic Tubing /glass /Polycarbonate	>50	NR	39 N	NR	high	no	0.25	(Puntambekar & Ahn, 2002)
Needle/Epoxy into Acrylic	5	67 psi	NR	NR	medium	no	2.38	(Korivi & Li, 2007b)
Silicon	6	20 psi	NR	NR	high	yes	0.84	(Gonzalez, et al., 1997b)
Heat Shrink Tube/Silicon	4.7	29 psi	3 N	NR	high	no	0.9	(Tingrui, et al., 2006)
PDMS/Needle/luer fitting	>50	102 psi	NR	NR	low	no	1	(Christensen, et al., 2005)
PDMS/Epoxy	33	100 psi	2 N	NR	medium	no	1.02	(Shifeng & Shaochen, 2003)
Metal/Plastic (commercial)	>1500	>435 psi	NR	0.1	low	yes	1.6	(Limited, 2007)
Parylene Captured Polyimide	0.018	120 psi	2.9 N	0 ‡	low	yes	0.14	This work

* Volume calculated from published drawings, not reported.
† Volume without epoxy = 0.089 mm^3
‡ Calculated Dead Volume, Calculated unswept volume = 0.0004 mm^3
NR = Not Reported

0.00115 mm^3 (1.15 nL). Robustness may have been impacted by the 87.5% fill percent and optimized interconnects may perform even better in the pull tests. The characteristics and performance of the microfluidic interconnects presented herein are compared against commercial and other research devices in Table 2-4. Pull-test results are comparable to those reported in the literature with the exception of the flanged thermoplastic approach (Puntambekar & Ahn, 2002), which achieved 39 N. This strength is attributed to the significantly larger volume of the interconnect (> 50 mm^3).

Both pressure and pull-test performance are related to the available surface area for the interconnect and either adhesion or applied force to generate the seal. The achieved performance with an interconnect length of 500 µm and a total capillary contact area of < 0.24 mm^2 speaks to the robustness of this polymer deposition approach for in-plane fluidic interconnects. The completed interconnect is shown in Figure 2-18 and demonstrates the low added volume aspect of this technique.

2.1.5. In-Plane Interconnect Conclusion

An in-plane microfluidic coupling scheme has been demonstrated that allows for low-volume interconnects to small diameter polyimide tubing with simple silicon processing

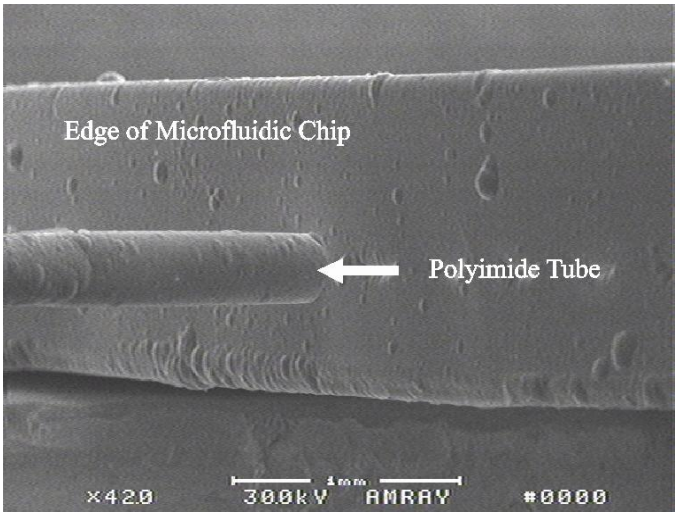

Figure 2-18: SEM of the side of the microfluidic chip. Image shows the small diameter (140 µm OD) tubing exiting in the plane and demonstrates the small volume nature of the interconnect system.

techniques and low-temperature Parylene C deposition. These interconnects are not removable, but this is not a requirement for implantable biomedical devices. The low volume of the interface, 0.018 mm^3 (18 nL), is important for medical applications where implant volume is critical and enables a system form factor consistent with subcutaneous implantation in mice. The robust design produced by the simulation and the optimization routine ensures the complete filling of the original gap between the channel and the polyimide capillary tubing with minimal deposition of Parylene C.

The model can produce designs for a range of tubing sizes with the only limitations set by the required amount of polymer deposited and the etch profile at the tubing/channel interface. The size of the tubing would not affect the utility of this method as much as the size and shape of the resultant gap between the tubing and the channel. The favorable results of the pull test and burst test for the non-optimized channels indicate that the optimized interconnects would perform as well if not better than those tested here. In light of these positive results, future designs could focus on shorter taper lengths requiring less deposited Parylene C while still maintaining sufficient contact area for robust performance. The low dead volume makes these interconnects suitable for drug delivery. The novel technology developed here was used in the fully integrated micropump to be described in Chapter 6.

2.2. Micro-molded Cannulae for Intracochlear Infusions in Small Rodents

Auditory dysfunction therapy research involving cochlear infusions in mice is challenging due to anatomical size and the lack of commercially available cannulae with integrated insertion stops. Historically, researchers have created custom cannulae by insertion of micro-tubing into larger tubing to create a stepped profile (Kawamoto, et al., 2001) or by manually applying a small volume of silicone Silastic® a fixed distance from the tip of the micro-tubing (Z. Chen, et al., 2006; Kingma, et al., 1992; Prieskorn & Miller, 2000) (see Figure 2-19). These approaches rely on the effective change in tubing diameter to provide an insertion stop to limit cannula intrusion into the intracochlear space. The profile also facilitates bonding the cannula to the bony tympanic bulla for long-term infusion studies. While successful in some applications, the methods of construction make consistency and reliability difficult to achieve, particularly for the small sizes required by the murine animal model. The cannula shown in Figure 2-19 (a) suffers the further problem of increased cannula stiffness, which can be a hindrance in small animal models. In the present investigation, a method has been developed to facilitate controlled interfaces for intracochlear infusions. Using microfabrication technologies, precision molds have been created that allow control of the size and shape of a Silastic® insertion stop molded around capillary tubing. The insertion depth is controlled by mold design. The goal of this study was to evaluate consistency of fabrication techniques and to assess the micro-cannulae suitability for use in intracochlear infusions.

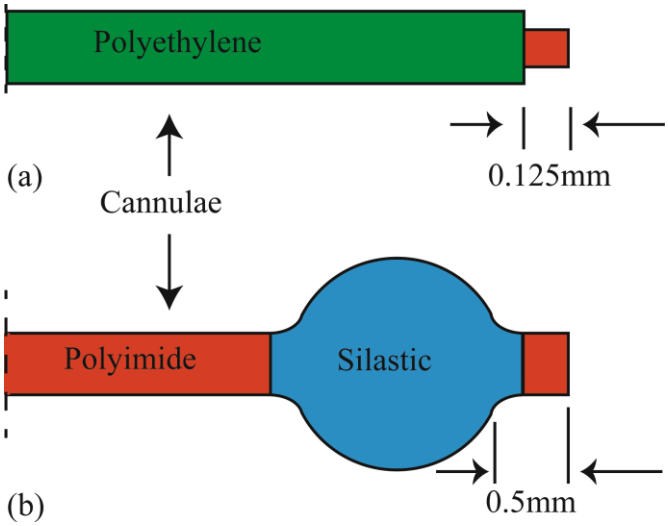

Figure 2-19: Drawings of cannula insertion stops presented in literature.
(a) Shows how small capillary tubing (125 µm OD) is inserted into a larger diameter cannulae to create a stepped profile as in (Kawamoto, Oh, Kanzaki, Brown, & Raphael, 2001). (b) Shows a drop of Silastic placed manually and cured on the end of a polyimide tube (~350 µm OD) as in (Kingma, Miller, & Myers, 1992).

2.2.1. Micro-Molded Cannula Concept

A micro-molding approach was developed that aims to control cannula insertion depth and the contact area between Silastic® and cochlear bone, and to retain the circular shape of the tubing during the cutting operation (critical to minimize the required cochleostomy hole size). Figure 2-20 shows the insertion stop micro-mold concept in cross-section. Current micro-molding procedures use either a surface micro-molding technique to create molded sheets of material like Parylene (Hong-Seok, et al., 2004) and Polydimethylsiloxane (PDMS) (J. R. Anderson et al., 2000) or micro-injection molding (Tolinski, 2005). The presented approach is similar to the injection molding except the material is ejected onto a surface mold instead of injected into a cavity mold. (Tolinski, 2005) reports difficulties associated with bringing macro processes down to the micro scale including variation of properties of low volumes of materials. This is the case with using Silastic® at the micro scale; thin films of the elastomer have longer curing times (Dow, 2007) and may require process changes such as oven curing to obtain the desired results. To ensure this would not be a problem for this application, oven curing was integrated into the molding process described in Section 2.2.3.

The mold dimensions and fabrication process control the insertion depth and the contact area. The total volume of the silicone is controlled by the mold structure as well as the precision delivery allowed by the Picospritzer III (Parker Hannifin Corp, Cleveland, OH). The tubing

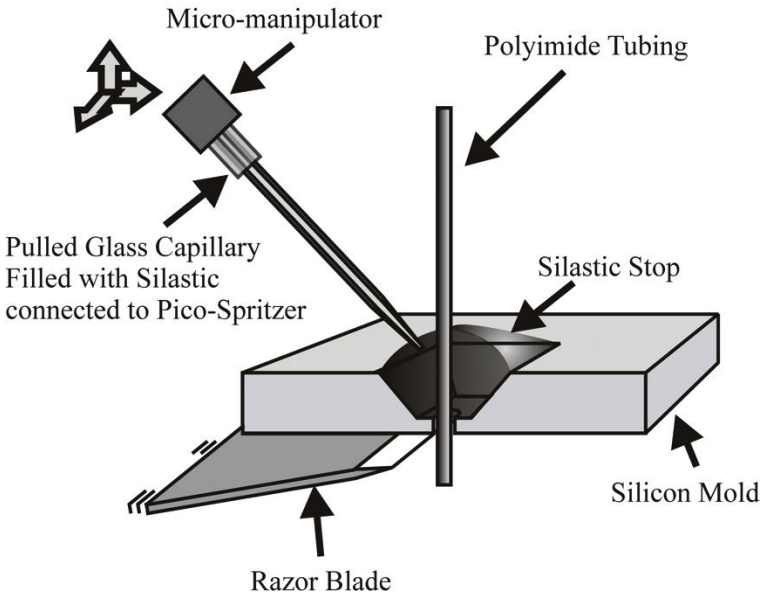

Figure 2-20: Polyimide micro-tubing was inserted through the silicon mold.
A pulled glass capillary filled with Silastic® was positioned with a micromanipulator. The Silastic® was delivered to the mold site by a Picospritzer III picoliter ejector. After curing of the Silastic®, the protruding tube was cut from the underside with a razor blade. The cannula with integrated insertion stop was then removed from the mold.

was supported by the mold during the cutting operation to ensure maintenance of tube roundness.

2.2.2. Micro-Mold Fabrication

The silicon mold was created from silicon wafers (520 μm thick) using standard micromachining fabrication processes as shown Figure 2-21. A nitride film, 1500 Å, was deposited via Low Pressure Chemical Vapor Deposition (LPCVD) on top of 500 Å of thermal oxide. Square openings in the 1500 Å silicon nitride film were patterned to define the widest dimension of the insertion stops.

Both sides of the wafer must be coated to prevent backside etching. After a one minute buffered oxide etch (BOE) to remove the oxynitride the nitride was pattered via plasma etch followed by another BOE to remove the 500 Å of oxide. A timed anisotropic KOH etch of the silicon substrate determined the insertion depth of the micro-cannulae. The wafers were etched for 5 hours and 25 minutes providing a measured etch depth of 346.4 μm, which created an insertion depth of 174 μm. The remaining nitride was then removed in hot phosphoric acid. Thermal oxide, 1 μm, was grown and 1 μm of PECVD oxide was deposited as a mask and an etch stop for the Deep Reactive Ion Etch (DRIE).

The backside mask was aligned to the KOH etched pits. 155 μm openings were then patterned through the 2 μm oxide on the backside of the wafer. A DRIE was performed to etch through the backside of the wafer with an etch stop at the topside oxide. Following oxide removal, the finished molds were diced from the wafer and cleaned with WRS™

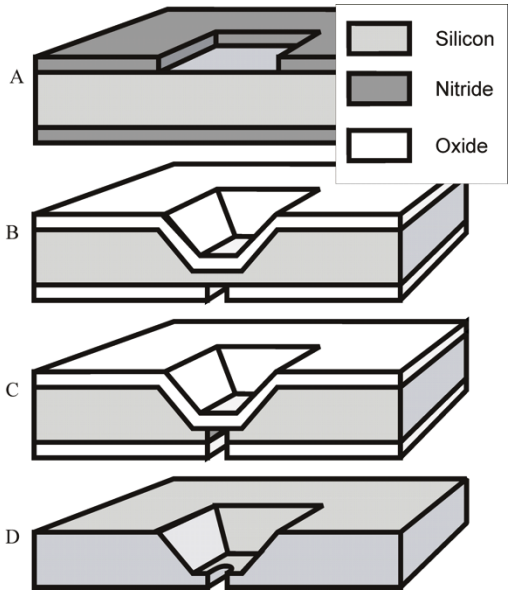

Figure 2-21: Cross-sectional view of the silicon mold fabrication process
(A) Square openings in a 1500 Å silicon nitride film were patterned. (B) A timed anisotropic KOH etch determined the insertion depth of the micro-cannula. The nitride was removed. 2 μm of oxide was used as a mask and as an etch stop for the DRIE. 155 μm openings were patterned through the 2 μm oxide on the backside of the wafer. (C) DRIE etch through the backside of the wafer with an etch stop on the topside oxide. (D) Following oxide removal, the finished molds were diced from the wafer, cleaned and ready for use.

200 Cleaning Solution (General Chemical, Hollister, CA).

2.2.3. Micro-Molding Process

To create molded insertion stops on micro-cannulae, medical grade Silastic® (MDX4-4210, Dow Corning, Midland, MI) was mixed with cross-linker, placed under vacuum for 20 minutes to remove air bubbles, and allowed to set for 30 minutes prior to being packed into pulled glass pipettes.

The silicon molds were degreased with acetone, cleaned with Micro-90® detergent (International Products Corp.) and baked for 15 minutes at 80° C. A thin film of detergent remained on the mold to act as a release agent. Polyimide micro-tubing (# 044, 138 μm OD, 112 μm ID, Microlumen, Tampa, FL) was cleaned with isopropanol and then inserted into the silicon mold as shown in Figure 2-20. The diameter of the DRIE hole on the backside of the wafer measures 155 μm and the hole narrows slightly as it enters the silicon, which provided a pressure fit to hold the tubing in the mold. The mold and tubing were held in place by a simple fixture (not shown). The Silastic® filled pipette was placed in a micromanipulator and connected to a Picospritzer III, which provided regulated pulses of air to control the dispensed volume of the silicone. The pipette tip was brought to the mold site and Silastic® was ejected to create the insertion stop. The Silastic® was cured at 80° C for 15 minutes, and a razor blade was used on the back side of the mold to precisely cut the tubing to length. Mold support around the micro-tubing during the cutting process helped maintain roundness. The cannula was then manually removed from the mold.

2.2.4. Cannula Stop Evaluation

Three critical design parameters were examined to evaluate success of the molding process: insertion depth, interface contact area, and tubing out of round. Physical dimensions of micro-cannulae created from multiple molds were measured as detailed in Figure 2-22. Worst-case variations were found to be 5 μm for insertion depth, 502 μm^2 for interface contact area, and 7% for tip out of round. Data for these parameters have not been reported for manually fabricated insertion stops (Z. Chen, et al., 2006; Kawamoto, et al., 2001; Kingma, et al., 1992; Prieskorn & Miller, 2000).

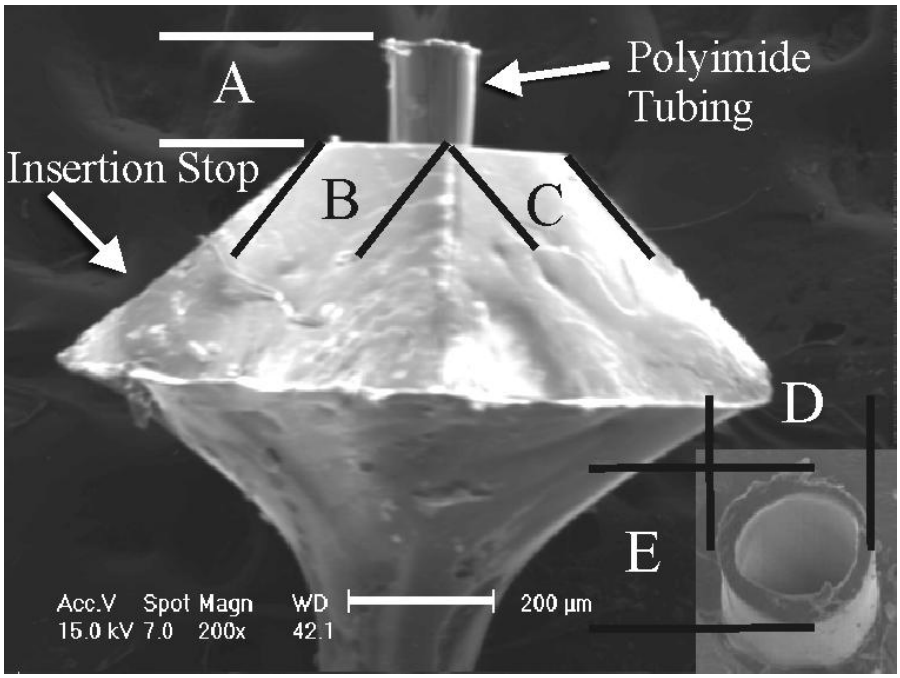

Figure 2-22: SEM of micro-cannula showing critical dimensions of integrated insertion stop.
Inset is tubing tip (magnification 320x).
Insertion Depth = A (µm): Avg. = 175.7, Std. Dev. = 1.1, Max. = 178.4, Min. = 173.4 (19 samples, three molds)
Interface Contact Area = B•C (μm^2): Avg. = 62,383. Std. Dev. = 290, Max. = 62,550, Min. = 62,048 (3 samples, one mold)
Out of Round = D/E within part out of round: Avg. = 1.03, Std. Dev. = 0.02, Max. = 1.07, Min. = 1.00 (20 samples, three molds)

Adhesion of the Silastic® stop to the polyimide tube was measured to aid process evaluation and control. Stop adhesion was measured with a strain gauge (1.5/120-LY11, Omega Engineering Inc., Stamford, CT) as shown in Figure 2-23. The average force required to pull the stop off the tubing was 0.17 N for a sample size of 17 (Std. Dev. = 0.09 N). Inclusion of an extension above the surface of the mold on the tubing increased the required force to 0.22 N for a sample size of 9 (Std. Dev. = 0.1 N). The large standard deviations could be the result of differing contact areas between the stop and the tube.

The out of round parameter as well as the quality of the cut is controlled by the condition of the cutting device and the geometry of the DRIE backside etch. The backside etch can be controlled within less than 1.5 µm. The main challenge with quality of cut is elimination of small (20 µm) protrusions of thin polyimide or 'flags'.

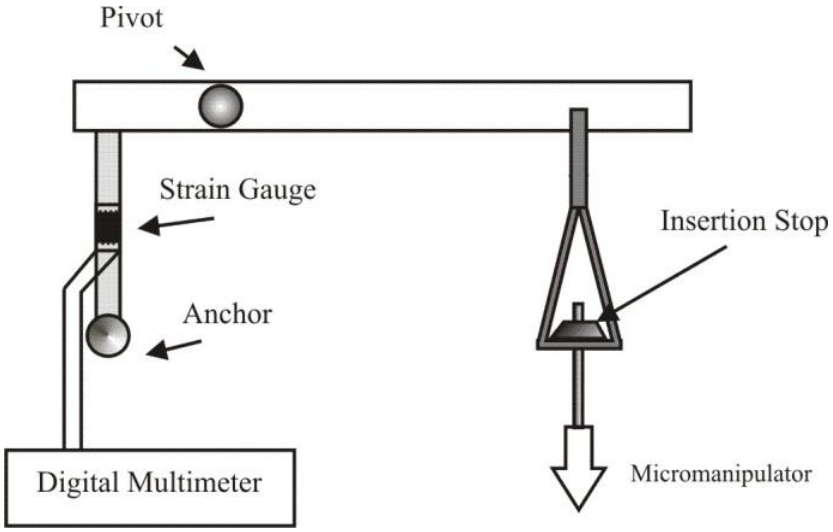

Figure 2-23: Cannulae adhesion measurement setup.
A lever was used to magnify the force on the strain gauge. The system was calibrated using a series of measured weights.

In this study an anisotropic KOH etch was used, however, an isotropic etch or a combination of an anisotropic etch followed by an isotropic etch could be used to define a more rounded insertion stop profile. Polishing the wafers before they are diced is another method of controlling the insertion depth.

2.2.5. Histological Evaluation of Cochlear Infusion Site

Surgery was performed on the left (ipsilateral) ear of adult CBA/CaJ mice. Following the procedures initially developed by (Jero, Tseng, Mhatre, & Lalwani, 2001) and modified by (Z. Chen, et al., 2006), the tympanic bulla was exposed by a ventral approach. A cochleostomy was drilled by hand using a micro-drill bit (# 05M020, 200 μm diameter, Drill Bit City) at a location approximately 300 μm below the stapedial artery stump. Polyimide infusion tubing with a molded insertion stop was inserted into the cochleostomy. Cyanoacrylate (Loctite 4206 Medical Grade Adhesive) was used to secure the infusion tubing and molded insertion stop to the cochleostomy opening. The insertion point at the basal turn of scala tympani is illustrated in Figure 2-24.

Following animal sacrifice the temporal bones were removed. The cochlea was decalcified and transferred to a cryo-mold filled with embedding compound.

10-μm thick sections were cut on a cryostat at two different orientations to allow visualization of the cochleostomy site and placement of the cannula tube in the scala

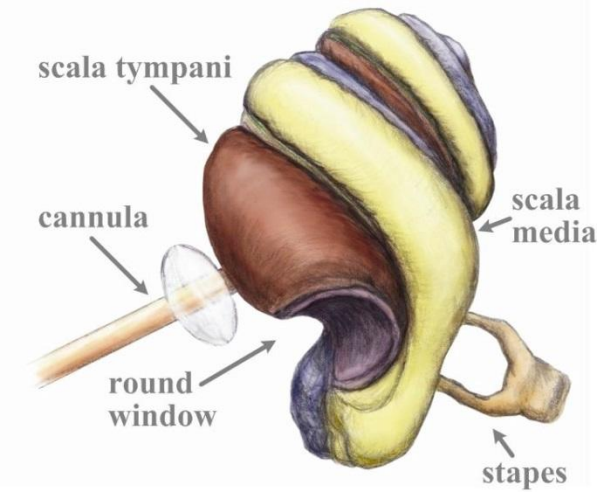

Figure 2-24: Illustration of cannula insertion into the murine cochlea.
The insertion point is located at the basal turn of the cochlea near the round window.

tympani. These sections were collected onto electrostatic glass slides and stained with H&E (see Figure 2-25). The Histology revealed the cannula to be located correctly within the scala tympani.

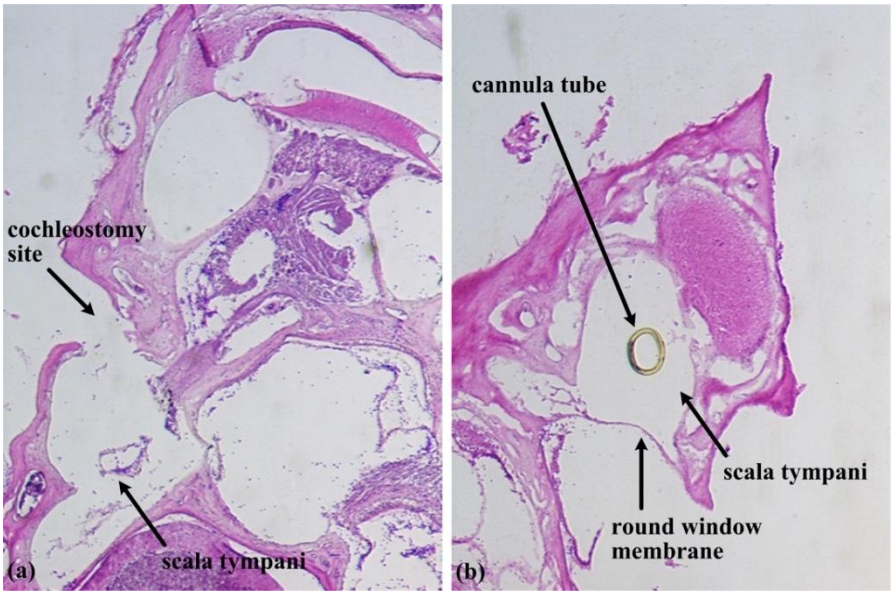

Figure 2-25: Histological images showing cannula placement.
Cochlear sections following fixation, decalcification, sectioning (10 μm thick), and H&E stain.
(a) Cross-section showing cochleostomy entry site into scala tympani. Note that no damage to adjacent tissue is evident. (b) Cross-section perpendicular to cannula tube showing round window membrane, and scala tympani with inserted cochleostomy tube.
Note: tube section was located here prior to H&E stain, but was manually replaced to replicate the pre-stain location

2.2.6. Cannula Stop Conclusion

The presented micro-molding approach allows consistent manufacture of micro-cannulae specifically designed for intracochlear infusions in mice or other small rodents. The mold fabrication process and molding techniques permit insertion depth control within 5 μm, interface contact area control within 502 μm^2, and 7% for tip out of round. Intracochlear infusions in CBA/CaJ using micro-cannulae designed especially for the surgical approach were performed with post-surgery histology verifying proper placement of the cannula tube in the basal turn of the scala tympani without damage to adjacent structures. Future studies could explore additional etch methods, including isotropic and anisotropic plasma etches as well as modifications to the process such as cutting tool stabilization and use of double sided polished wafers.

Additional molds with longer and narrower stops could also be studied to enhance insertion stop adhesion and improve optical access to the cochleostomy site during surgery. This approach to an engineered interface for intracochlear infusions has the potential to enhance infusion consistency and mitigate complications associated with variable insertion depths and leakage at the cochleostomy site.

2.3. Interconnect Summary

The low-volume aspect of the interconnect technique enables the planar form factor desired for subcutaneous implantation. The materials used in both technologies satisfy the design target of biocompatibility. The burst test results, 827 kPa far exceeds the target for differential pressure. Direct coupling of the micropump to biological systems is enabled by the integrated cannulae stops molded directly onto the end of the same capillary tubing (140 um OD) as is used for the interconnects.

Before discussing the micropump channels to which the micro-capillary tubing is connected, the fabrication process for the pump will be developed. To this end, the pump flow control is considered next.

Chapter 3 Flow Control

Life is a series of natural and spontaneous changes. Don't resist them - that only creates sorrow. Let reality be reality. Let things flow naturally forward in whatever way they like.
Lao Tzu

Diaphragm pumps require a means of controlling the flow directionality within the channels. This can be accomplished either by the use of valves or through peristalsis. Valves can be either active, such as a diaphragm actuated with external force (e.g. piezoelectric or electrostatic), or passive, as in the case of a flap check valve, where pressure of the pumped fluid opens and closes the valve (see Figure 3.1). Passive valves also include fixed geometry valves, which rely on the fluid mechanics within the channel to favor flow in one direction over another, resulting in flow rectification.

Many valves used for MEMS based micropumps are out-of-plane passive valves using diaphragms (Feldmann, Demming, Lesche, & Buttgenbach, 2008; Jung Ho, King Tong, & Diamond, 2008; Wu, Yang, & Chen, 2006), or flaps (Dong et al., 1999; G. Xu, Tay, Iliescu, & Luar, 2005) while others use in-plane flap valves (Loverich, Kanno, & Kotera, 2007; B. Yang & Lin, 2007). A check valve with high-pressure cut-off was developed by (Lo & Meng, 2011), the cracking pressure, the pressure needed to open the valve, is quite low, 2.9 kPa (0.425 psi), however, the critical actuation volume is greater than that possible in the current device. Figure 3-1 (a) is a drawing of a diaphragm based active valve that is normally open permitting underlying fluid flow, unless deformed (by positive pressure above it or by other mechanical means) at which time it blocks the fluid flow. The valves in Figure 3-1 (b) and (c) create a difference in the fluidic resistance in the forward and reverse direction. In the diffuser/nozzle valve, the fluid flow is well

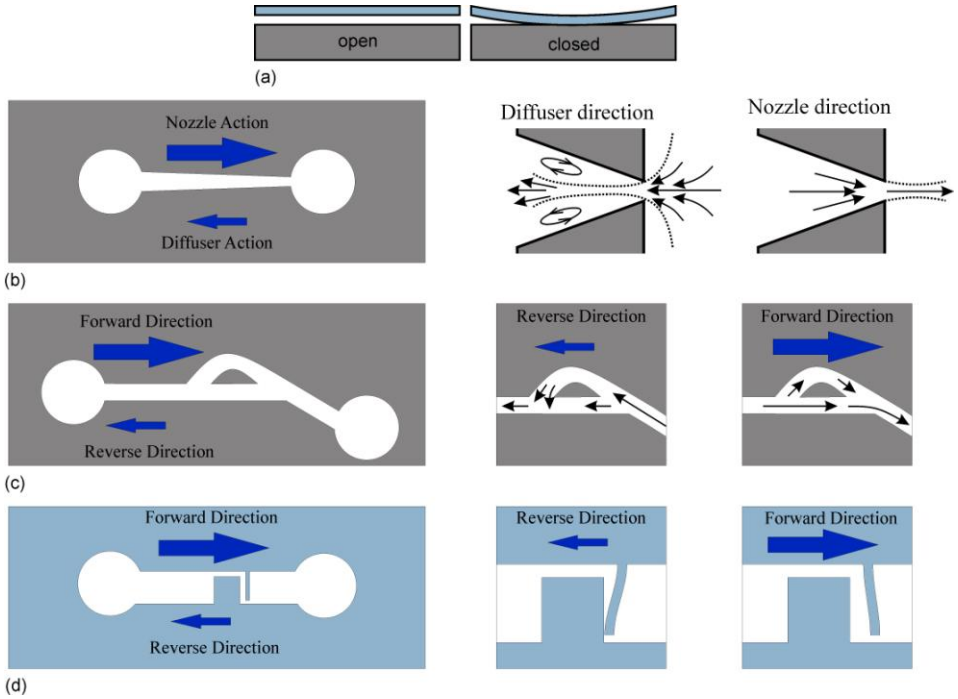

Figure 3-1: Diagram of available valve types.
(a) Cross-section, side view, of an active valve using a diaphragm to block flow via positive pressure applied from above (b) Diffuser/nozzle valve (top view) (c) Tesla valve adapted from (Bendib & Francais, 2001). (d) In-plane flap valve formed in compliant polymer. Adapted from (B. Yang & Lin, 2007; Zahn, 2006)

controlled in the nozzle direction but can experience turbulence in the diffuser direction, dependent on the flow regime, which increases the fluidic resistance. The Tesla valve, which allows the creation of preferential flow from the difference in fluidic resistance, is described in Section 3.2. Figure 3-1 (d) is a normally open check valve utilizing a PDMS flap that is pushed by reverse direction pressure against a stop in the flow path sealing off the flow. Forward direction flow opens the gap between the stop and the flap.

3.1. Hydrodynamics

Fixed geometry valves, such as those presented by (Deshpande, Gilbert, Bardell, & Forster, 1998; Hwang, An, Ko, Shin, & Lee, 2007; Yoon, Choi, Lee, & Kim, 2007), require an understanding of the flow regime in which the pump operates as they rely on the hydrodynamics of the system to produce a valve effect. The Reynolds number (Re), the ratio of the inertial to viscous forces, needs be calculated. Systems with low Reynolds numbers, Re, require careful consideration in the design phase to ensure sufficient flow rectification to enable pumping. This is true for fixed geometry valves, such as nozzle-

diffuser and Tesla valves (Singhal, Garimella, & Murthy, 2004), as well as valves that rely on differential pressure to close such as normally open flap valves (Loverich, et al., 2007). An understanding of the type of flow in the presented system will enable the selection of a suitable method of flow control as well as providing other design parameters for the overall system. For example, ensuring the developed pressure is sufficient to overcome the fluidic resistance of the devices internal channels and external interface tubing. The various types of flow possible in MEMS fluidic systems is first considered, followed by a discussion of the fluidic resistance of a system. Water is used as the fluid in the following calculations as a benchmark.

When the flow velocity of water exceeds the speed of sound in water then a supersonic flow rate has been reached. Although supersonic flow may be achieved via MEMS micro-nozzles for specialized pumps (Louisos & Hitt, 2008; Morinigo & Hermida-Quesada, 2010), the maximum flow rate for the system under consideration is well within the subsonic range. Hook's law (3-1) was used to determine the minimum flow velocity that the fluids would need to reach for supersonic flow.

$$c = \left(E/\rho\right)^{1/2} \tag{3-1}$$

E the modulus of elasticity is 2.15 x10^9 N/m^2 and ρ the density of water is 999.8 kg/m^3, the speed of sound in water is 1466 m/s. Even for very small channels with 1-µm by 1-µm cross-section, this would require a flow rate of more than 88.2 µL/min, which is well above the flow rates used in animal experiments, 1 µL/hour to 22 µL/hour (Brown, Miller, Altschuler, & Nuttall, 1993; Fiering, et al., 2009) and much more than the maximum rate for the pump of 100 nL/min. The speed of sound is decreased as the inverse of square root of the density and even very dense materials would remain in the subsonic range for flow in this range.

Changes in temperature and pressure of the fluids to be pumped are sufficiently small so that they may be considered incompressible (Marks, 1978). This assumption will hold true as long as the pumping action remains isothermic with no bubbles forming within the fluid. Other characteristics, viscous versus invicid flow and laminar versus turbulent flow, require calculation of the Reynolds number, the ratio of the inertial and viscous forces.

The definition of the Reynolds number includes the density, viscosity, and velocity of the fluid and a characteristic dimension of the system. For incompressible gasses the formula for the Reynolds number is shown in (3-2) (S. Kim & Karrila, 1991), where Re is the Reynolds number, ρ is the density of the fluid, V is the mean fluid velocity, L is the characteristic dimension of the system, and μ is the dynamic viscosity.

$$\mathrm{Re} = \frac{\rho V L}{\mu} \tag{3-2}$$

The characteristic linear dimension, L, in a circular pipe is simply the diameter, D, of the pipe. In the case of other shapes (e.g. rectangular channels), an equivalent diameter is defined. If the width is more than an order of magnitude greater than the depth of the channel the characteristic dimension used should be twice the depth (White, 1979). For square or rectangular channels where the height and width are comparable the characteristic dimension is taken to be the hydraulic diameter, D_H, which is four times the cross-sectional area, A, divided by the internal perimeter, P_i, (3-3) (Munson, et al., 2005). The internal perimeter for a channel is the total perimeter of all channel walls that are in contact with the flow.

$$\text{—} \tag{3-3}$$

The Reynolds number can be used to determine whether the flow is viscous or inviscid. High Reynolds numbers indicate that the inertial forces should dominate the equations as in the case of inviscid flow. At the other extreme is "Stokes flow" where $Re << 1$, a special case where inertial forces can be neglected compared to viscous forces. The flow control mechanisms available will depend upon the flow regime in which the pump operates. Table 3-1 lists the ranges of Reynolds numbers for different types of flows.

As shown above, the designed pump will operate with Re << 1. Therefore the Navier-Stokes equation, (3-4), is used to describe how the inertia and viscosity affect flow.

Table 3-1: Laminar vs. Turbulent flow by Reynolds number ranges

$0 < Re < 1$	Highly viscous laminar "creeping" motion
$1 < Re < 100$	Laminar, Strong Reynolds-number dependence
$100 < Re < 10^3$	Laminar, boundary-layer theory useful
$10^3 < Re < 10^4$	Transition to turbulence
$10^4 < Re < 10^6$	Turbulent, moderate Reynolds-number dependence
$10^6 < Re <$ infinity	Turbulent, slight Reynolds-number dependence

(3-4)

ρ is the density, μ is the viscosity, $\boldsymbol{v}$ is the velocity vector, and P is the pressure. When Re << 1 the inertial components on the left of (3-4) can be ignored leaving Stokes equation, (3-5).

(3-5)

This means that the pressure gradient is a function of the viscosity and the fluid velocity. The Hagen-Poiseuille equations are exact solutions to the Navier-Stokes equation, (White, 2011).

Hagen-Poiseuille law gives the equation for the pressure difference along a low profile rectangular cross-section channel ΔP_c (3-6) and the fluidic resistance in (3-7), which gives the pressure lost in a given device per volumetric flow rate and can be used to design device geometries.

(3-6)

(3-7)

where Q is the volumetric flow rate, μ is the dynamic viscosity, l the length of the channel, ΔP_c is the pressure drop across the channel, and L is the characteristic dimension of the system. For a circular channel or tube the corresponding formulae are given below.

(3-8)

(3-9)

where d is the diameter of the tubing.

These hydrodynamic properties have been used to design pump architecture appropriate for this project. The flow regime, as determined by the Reynolds number, Re, have been used to select the types of fluidic control that are effective in the calculated flow regime. Knowing the fluidic resistance will guide design of the diaphragms ensuring that sufficient momentum is transferred to the fluid to overcome the pressure drops through these resistances.

3.2. Fixed Geometry Valves

Flow rectification of a fluidic device is quantified by the diodicity, *Di*, the ratio of the pressure drop in the negative flow direction to that in the positive direction, as shown in (3-10),

(3-10)

where ΔP_{neg} and ΔP_{pos} are the pressure loss of the rectification geometries in negative and positive flow directions. The fluid is encouraged to flow in the direction that experiences less pressure drop across the device. Therefore, $Di \geq 1$, or the designation of positive and negative directions would need to be switched. The greater the ratio of pressure drop in the negative direction to that in the positive direction, the greater the diodicity and the greater preferential movement in the positive direction. The closer the ratio to unity the smaller the preference of flow in the positive direction and for $Di = 1$, there is no preferential flow due to the geometry. The device can have fixed geometry such as a nozzle, or the geometry can change due to fluid pressure such as a flap valve. For valves that close completely, $\Delta P_{pos} \rightarrow 0$ and the $Di \rightarrow \infty$. For a channel with no valve, $\Delta P_{neg} = \Delta P_{pos}$ leading to $Di = 1$.

Fixed Geometry valves create turbulence in the flow that works against the flow direction. In the Tesla valve shown in Figure 3-1 (c) the majority of the fluid in the forward direction passes through the main channel, where in the reverse direction much of the flow is pushed into the elbow and is made to work against the flow in the main channel. This causes a greater fluidic resistance and therefore a greater pressure drop in the negative direction creating flow rectification. Figure 3-2 shows the flow around a cylinder for various Reynolds numbers and illustrates how the pressure drops across a device. The pressure drop, when made asymmetric by the channel geometry leads to flow rectification. Figure 3-2 (a) is of particular interest as it shows how for very low Reynolds numbers the pressure drop is symmetrical, the same for forward and reverse flow therefore equal pressure drops across the device in both directions and therefore no preferential flow, $Di = 1$.

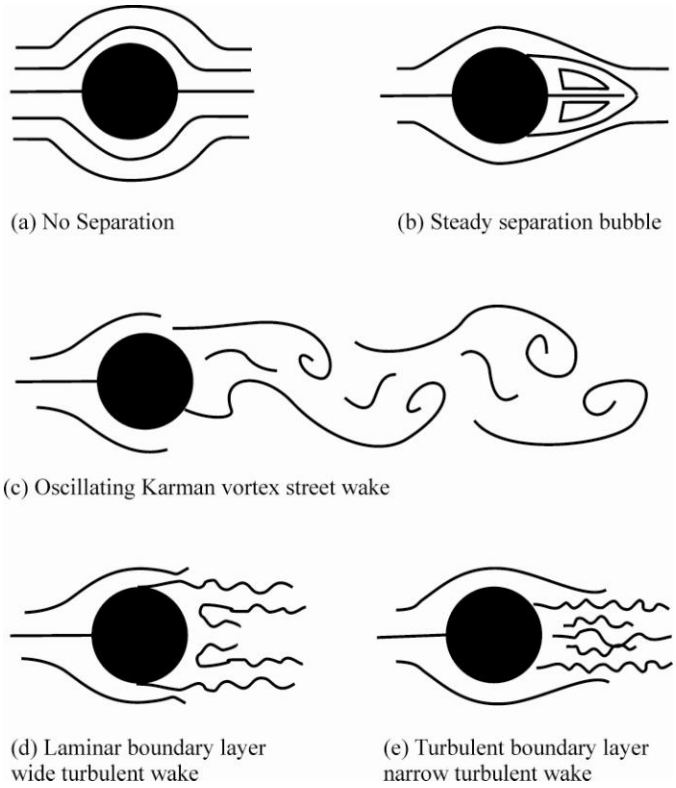

Figure 3-2: Variation in flow pattern for flow over a cylinder.
(a) Reynolds number = 0.2; (b) 12; (c) 120; (d) 30,000; (e) 500,000; Flow is from left to right.
Adapted from (Munson, Young, & Okiishi, 2005)

Equation (3-2) is used to calculate the Reynolds number. The maximum flow rate for the micropump, Q, is 100 nL/min (1.67 nL/s). Using channel dimensions of 100 μm wide and 15 μm deep as a starting point for the fluidic system, the fluid velocity, $V = Q/A$, is 0.111 cm/s, cross-sectional area $A = 1.5 \times 10^{-9}$ m^2, $P_i = 2.3 \times 10^{-4}$ m. This gives a hydraulic diameter, D_H, of 2.6×10^{-5} m. Using these and the values in Table 3-2 for water, results in a Reynolds number, Re = 0.029. More viscous fluids, with the same density, would have lower Reynolds numbers, as would fluids with lower flow rates.

Figure 3-3 is a graph of the Reynolds number versus cross-sectional area for square channels for flow rates of 100 nL/min, 150 nL/min, and 500 nL/min. This illustrates that even for very small channels (< 15 μm x 15 μm) or large flow rates (500 nL/min) the Reynolds number is quite low. For the channels in the micropump, the flow is in the highly viscous laminar "creeping" flow range. In this range, the inertial forces may be neglected. With the range of Reynolds numbers, it is now possible to further characterize the flow, and the types of devices that can be used to control flow directionality.

Table 3-2: Variables to Determine Reynolds number, Re

Symbol	Quantity	Value	Dimension
V	Mean fluid velocity	1.67×10^{-3}	m/s
μ	Dynamic viscosity of water	1.0	mPa·s
P	Density of the fluid (water)	998.2	kg/m^3
Q	Volumetric flow rate	2.50×10^{-12}	m^3/s
A	Cross-sectional area	1.5×10^{-9}	m^2
L	Characteristic Dimension	2.6×10^{-5}	m

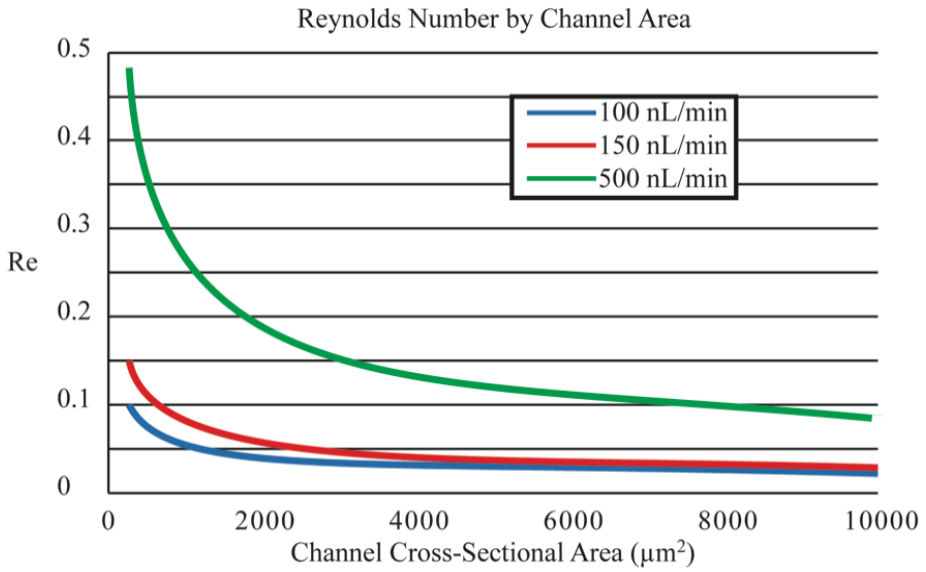

Figure 3-3: Graph of Reynolds number vs. Channel Area.
Square channels with varying cross-sectional area for flow rates of 100 nL/min, 150 nL/min, and 500 nL/min.

Numerical analysis by (Singhal, et al., 2004) for low Reynolds numbers (Re = 200, 400, and 1000) indicates that diffusers and Tesla valves will not function at very low Reynolds numbers. (Gerlach & Wurmus, 1995) modeled dynamic micropumps with Reynolds numbers, $0 < Re < 10^8$, and determined the critical number below which flow is completely laminar to be Re = 15. They showed that below this value, valves relying on pressure loss coefficients, such as fixed geometry valves will not work.

(Fadl et al., 2009) investigated (numerically) a variety of fixed geometry valves, including Tesla and nozzles. They found that for the Tesla, nozzle, heart, and triangle shapes, Reynolds number must be larger than 10 to achieve rectification, only the semicircular valves showed any rectification at Re < 10, but these showed no rectification for Re < 0.8. (Deng, Liu, Zhang, Wu, & Korvink, 2010) examined diodicity versus Reynolds number and determined that for various types of Tesla valves, the diodicity equals 1 with no flow rectification for Re < 1. For the micropump, with Re < 0.05, fixed geometry valves will not work. This shortcoming in fixed geometry valve leads to a consideration of passive flap valves (i.e. check valves).

The differential pressure across a flap, or diaphragm, moves it against or away from a valve seat. When the flap is forced against the valve seat, the valve closes preventing the flow of fluid. The pumped fluid and not an external source provide the work needed to open and close passive flap valves, which can be normally open or normally closed.

Normally open valves require the pressure of the reverse flow to be sufficient to close the valve completely. Normally closed valves require only enough pumping pressure to open the valve. The normally open valves can be easier to fabricate, as the sealing surfaces are exposed during processing. (Loverich, et al., 2007) presented a PDMS flap valve (normally open) that does not fully close but instead relies on the diodicity of the valve structure similar to fixed geometry valves, as discussed in the section above on diodicity. This arrangement can produce a pressure drop across the valve in the fully open position that is less than the drop in the reverse flow directions when the valve is partially closed restricting the flow path leading to flow rectification as discussed in the previous section. However, they reported that it was capable of diodicity of 1.6 for Reynolds numbers as low as Re = 0.7 but no diodicity was reported for lower numbers.

In general, conclusions about the reported efficiency of fixed geometry valves (and passive valves that do not fully close) suffer from a lack of agreement for expressing the rectifying efficiency (Fadl, et al., 2009). No rectification has been reported for very low Reynolds numbers, $Re << 1$ and only modest diodicity of 1.6 has been reported for $Re < 1$.

The calculated Reynolds number for this micropump, $Re < 0.03$, is very low indicating laminar, non-turbulent, flow. The discussion above clearly shows that for Reynolds number in the range of this microsystem, no rectification ($Di = 1$) is achievable for either fixed geometry valves, normally open valves.

Because the normally open valves do not provide flow rectification, normally closed valves, which can seal completely in the closed position, will be considered. Only out-of-plane valves were considered due to the fabrication complexity of in-plane normally closed valves. Flap valves that are able to close completely do not suffer from the same restrictions for low Reynolds numbers, as they will open as long as the pressure in the positive direction is great enough to deform the flap and open the valve by means of a differential pressure. This requires a flap or diaphragm that closes against a stop and a flow path above the device wafer, which will require an additional substrate layer in the stack. A conceptual drawing of an out-of-plane valve is shown in Figure 3-4. The pump stroke volume needs to be larger than the volume the flap can displace while deforming before opening. These out-of-plane valves require more complex processing and are

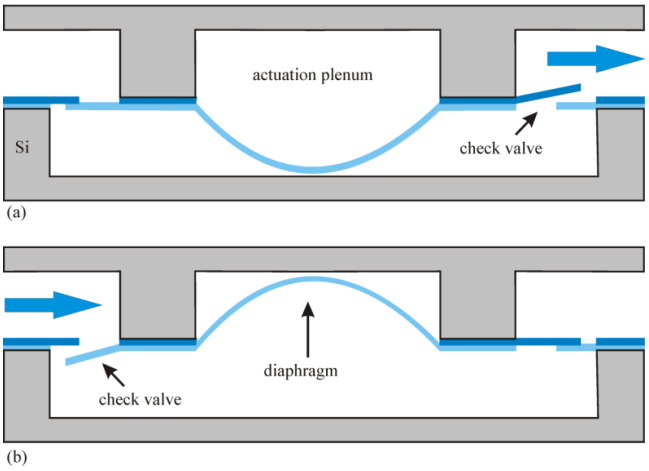

Figure 3-4: Drawing of out-of-plane passive check valves.
The top wafer contains the plenum whose pressure is controlled by the actuator (not shown), the fluid path, and one of the check valve flaps. The bottom wafer contains the pump chamber and diaphragm and the other valve. (a) the 'push' pump cycle (b) the 'draw' pump cycle

difficult to fabricate while ensuring the flow path is biocompatible. Due to fabrications complexity, normally closed valves are not used for this project.

3.3. Peristalsis

Another type of fluidic control that does not rely on differential pressure of the pumped fluid to activate the valves is a peristaltic pump. Peristaltic pumps are a form of bio-mimicry where devices are designed to imitate the function of biological systems. Peristalsis is the mechanism of swallowing where waves of esophageal contractions push material towards the stomach. Though recent work in MEMS has come closer to mimicking the tubular shape of the esophagus with various actuating mechanisms effectively contracting a tube (Jeong & Konishi, 2008; Komatsu, Binh-Khiem, Iwase, Matsumoto, & Shimoyama, 2009; Wang & Lee, 2006), most of the MEMS peristaltic pumps reviewed use diaphragm-covered chambers in place of the single tube (L.-S. Jang & Yu, 2008).

Peristaltic pumps with individual diaphragms are a variation of mechanical diaphragm pumps where two additional diaphragms have been used to replace the outboard valves. Many MEMS peristaltic pumps use three chambers, the minimum number required for peristalsis since one diaphragm must block the channel at all times to enable the directional flow. Peristaltic pumps do not rely on the inertial forces of the pumped fluid for flow control and therefore do not fail with low Reynolds flow as do the fixed

Table 3-3: Actuation Sequence to Achieve Peristalsis

Cycle/chamber #	1	2	3	4
1	down	down	up	up
2	up	down	down	up
3	up	up	down	down
4	down	up	up	Down

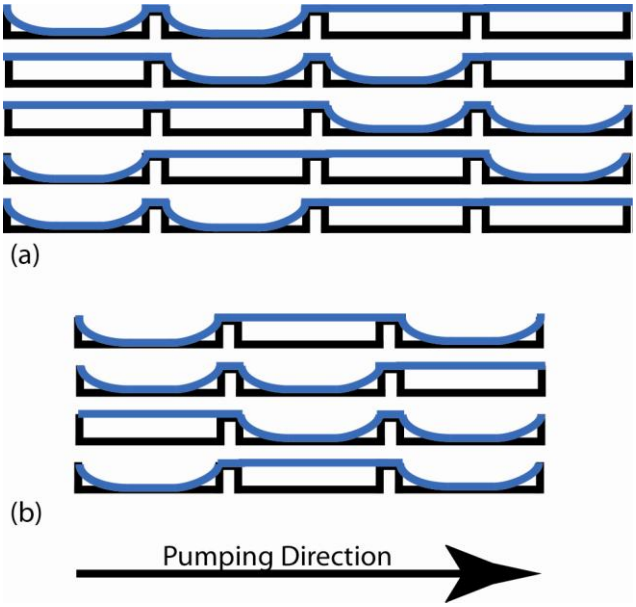

Figure 3-5: Sequence of actuation to effect directional pumping.
(a) four-chamber pump, (b) three-chamber pump.
Peristaltic flow control in diaphragm based system. The four-chamber pump delivers two boluses of fluid in four actuation steps. The three-chamber pump delivers one bolus with three steps. The four-chamber pump, 2 actuations/bolus, is more efficient than the three-chamber, 3 actuations/bolus

geometry and normally open passive valves. Table 3-3 shows the four-step actuation cycle with chamber pairs, 1 & 3 and 2 & 4, acting tandem. When chamber one is pushed down (i.e. closed) chamber three is pulled up (i.e. open).

Figure 3-5 shows the actuation sequence for a four-chamber pump and a three-chamber pump. The four-chamber pump uses a four step sequence with two chambers in the up position and two chambers down. The first two chambers begin in the closed position and hold the two boluses of fluid in the last two chambers. The first chamber then opens as the third chamber closes, this draws fluid in from the left and pushes one bolus of fluid out of the pump. The second chamber then opens and the fourth closes drawing more fluid in from the left and pushing the second bolus out at the right. The first chamber then closes and the third chamber opens, moving two boluses of fluid to the middle of the pump. The second chamber closes and the fourth chamber opens, moving the two boluses to the end of the pump bringing the pump to the starting position. These four sequence steps are required to deliver two boluses of fluid in the four-chamber pump. The three-chamber pump requires three actuation steps but delivers only one bolus per sequence. This translates to four chamber actuations to deliver two boluses for the four-chamber pump and three actuations to deliver one bolus for the three-chamber. So the four-chamber pump is more efficient delivering more fluid per actuation. In fact, the efficiency of a peristaltic pump increases with the number of chambers but the complexity also increases.

3.4. Conclusion

The highly laminar flow regime extant in the presented micropump requires either the use of peristalsis, active valves, or normally closed passive valves. The latter require more complex processing and/or more substrate layers to fabricate. Peristaltic MEMs pumps using diaphragm covered chambers is really a form of active valve pump where the chambers act as both pumping chambers and active valves. The benefit of this approach is that the ‘valves’ in this case also contribute to the pumping action. For these reasons, peristalsis is selected as the flow control method. A four-chamber design is used not just for the increased efficiency, but because it will allow for actuation by push-pull actuation mechanisms that would open one chamber as it closes another. Having decided upon a specific flow control paradigm, the design and fabrication of the required biocompatible flow path can now be considered.

Chapter 4 Biocompatible Flow Path: Micropump Diaphragms and Channels

I tried to use the questions and answers as an armature on which to build a sculpture of genuine conversation.
Clifton Fadiman

A non-reacting, non-water-adsorbing, biocompatible flow path that includes micropump diaphragms and fluidic channels is required for the implantable pump. Parylene C is an attractive material for biomedical flow paths due to its biocompatibility and chemical resistance (Najafi, 2007). Additionally, as discussed in Section 2.1.1, Parylene C penetrates deeply into narrow spaces, which allows it to coat fluidic channels as well as forming diaphragms.

Parylene diaphragms for pumps or valves can be formed by a variety of techniques. One technique is to etch through from the back side of a Si wafer (Zopfl, Klare, Wachutka, & Schrag, 2009) using Parylene as an etch stop on the front side of the wafer (see Figure 4-1 (a)). On the backside, openings are patterned in a hard mask, such as nitride, and a diaphragm is formed by removing the bulk silicon under the Parylene. This can be used to create chambers by bonding another substrate, silicon or glass, to the backside closing off the etch opening. As the height of the chamber is determined by the wafer thickness, creating chambers less than 100 μm can be difficult and creating systems with a number of different channel/chamber heights is not possible.

Another method uses sacrificial layer release (Fan, Engel, Chen, & Liu, 2004; Majumdar, Satyanarayana, & McCormick, 2006), where Parylene is deposited on top of a sacrificial material such as silicon oxide (SiO_2) as shown in Figure 4-1 (b). The sacrificial material is removed with a wet etch process leaving the Parylene suspended over an open

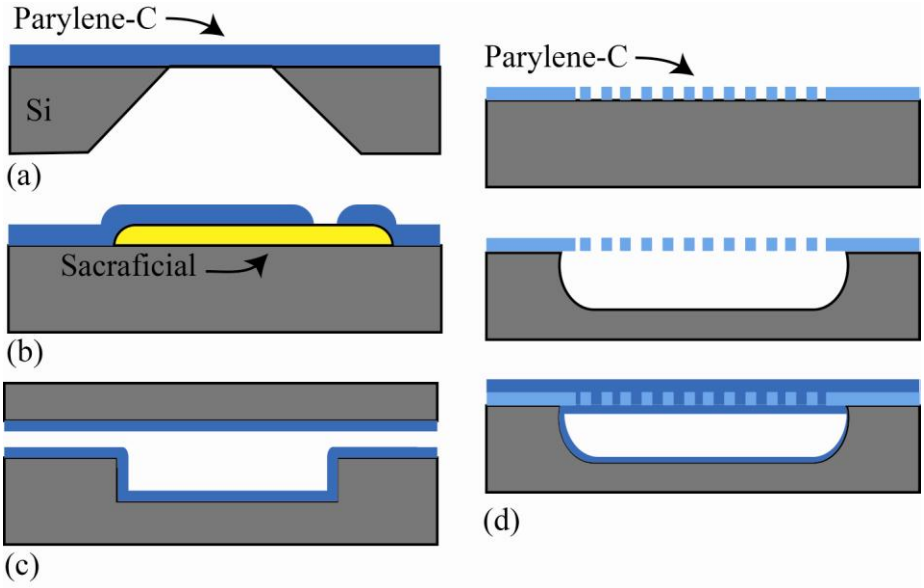

Figure 4-1: Techniques for forming Diaphragms.
(a) Backside etching of Si wafer to form Parylene C diaphragm. Parylene C is used as etch stop. (b) Sacrificial layer defines chamber under Parylene C diaphragm. (c) Wafer level transfer, chambers and channels formed on wafer, diaphragm of Parylene transferred from carrier wafer.
(d) A Parylene C layer is patterned with holes to define underlying chamber, the Si is isotropically etched through these holes. Parylene C then fills the holes and coats the chamber. (Parylene C shown in two colors for clarity)

cavity previously occupied by the oxide. Openings must be made in the Parylene, via laser ablation or plasma etching, to allow the etchant access to the sacrificial material. These openings must be subsequently closed.

In a third method, wafer level transfer (H. Kim & Najafi, 2007), chambers and channels are etched in a Si wafer, which is coated with Parylene, and another Parylene film is transferred from a carrier wafer (see Figure 4-1 (c)). This process relies on the bonding of the Parylene to the surface of the patterned wafer and release from the sacrificial wafer.

Recently, diaphragms for sensors have been formed *in situ* by etching-through small openings in a Parylene mask with a xenon fluoride (XeF_2) Si etch (Giacchino & Yu-Chong, 2008) (see Figure 4-1 (d)). A modification of this process is used here to allow *in situ* formed diaphragms while simultaneously coating the pump chambers and fluidic channels with Parylene C. This process allows for thinner diaphragms for pump applications with increased adhesion of the diaphragm to the substrate.

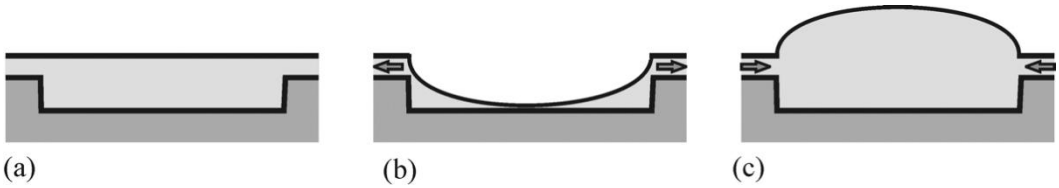

Figure 4-2: Three phases of a generic diaphragm pump chamber.
(a) Neutral position with equal pressure above and below the diaphragm. (b) Higher pressure above diaphragm pushes diaphragm down pushing fluid out of the chamber. (c) Lower pressure above the diaphragm pulls it up drawing fluid into the chamber.

4.1. Overall Concept (Hard Mask, Diaphragm Framework)

A hard mask of low tensile stress TEOS oxide is deposited via Plasma Enhanced Chemical Vapor Deposition (PECVD). The oxide is pattered to define fluidic cavities and to act as a framework onto which Parylene C is deposited creating a deformable diaphragm. TEOS is an excellent choice for a number of reasons. Low Stress TEOS deposition of a micron and beyond is routine, it is easily patterned with standard processes, and it is an excellent mask for XeF_2 etching of silicon. In addition, TEOS adheres well to the silicon substrate so that during the 'draw' pump cycle when the diaphragm is pulled upward by a lower pressure above it, no separation occurs. Figure 4-2 shows the three positions of the diaphragm over pump chamber with (c) showing the 'draw' cycle.

The TEOS oxide is patterned with a regular grid of apertures to define the fluidic regions to be etched into the surface of the silicon. The use of a low tensile stress TEOS allows for a fine framework structure that can be used to hold a thin deposition of polymer and form a diaphragm. Tensile stress oxide is required to reduce buckling of the etch-through mask; low stress is required so the mask will not break at the easily fractured attachment points. Figure 4-3 is an illustration of the

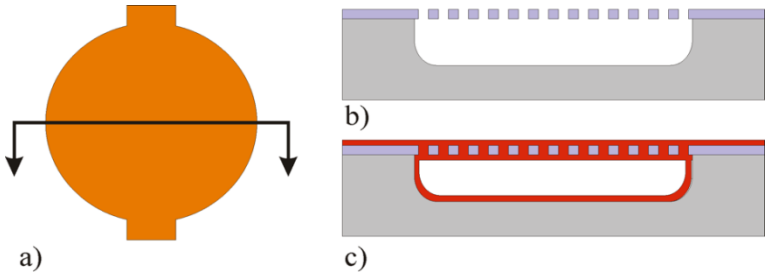

Figure 4-3: Hard mask and framework concept for in situ diaphragm formation.
(a) Top view showing layout of diaphragm and fluidic channel (b) Patterned TEOS (blue) allows Si etch creating fluidic features. (c) Parylene C (red) encapsulating TEOS to form diaphragm over chamber. The Parylene C also coats the chamber and microfluidic channels. (Not drawn to scale)

diaphragm concept showing the layout (a), the patterned TEOS mask (b), and the Parylene C forming a diaphragm over the fluidic chamber (c). The small openings (2 µm to 4 µm in diameter) in the TEOS mask allow for an isotropic Si etch with XeF_2 to form the underlying fluidic cavities as it releases the oxide structure. Photoresist can be used as an additional mask for the XeF_2 etch such that some areas of the patterned TEOS experience a deeper Si etch. In this way multilevel channels, chambers, and interconnects can be formed. The Parylene C not only forms the diaphragm but also seals the entire flow path with a biocompatible barrier.

4.2. Design

(Giacchino & Yu-Chong, 2008) used 1.3-µm thick masks (Parylene C, Au, Cr, Al) with 7.5-µm holes. Parylene C is the major component of the mask, the metals are part of the sensor being incorporated into the diaphragm. The spacing of these hole required a deep etch to connect neighboring etch sites and required thick depositions of Parylene, 8.5 µm. They incorporated Parylene anchors as an additional process with its own deposition step leading to a total diaphragm thickness of 21.5 µm. The reported pressure required to deform this thick diaphragm 15 µm, at 8.5 nm/psi, is more than 1700 psi. This diaphragm functions for the small deflections needed for sensors but is too stiff for the large deflections required for micropumps. Low power actuation for the large deflection of pumps necessitates thinner diaphragms.

4.2.1. Chamber Dimensions

The required chamber volume is informed by the flow rate requirement and the volume limits of actuation and the required compression ratio. The pump was based on design considerations of compression ratio for gas and liquid micropumps presented by (Richter, Linnemann, & Woias, 1998). The equation for the diaphragm compression ratio, ε, is shown in (4-1), where ΔV is the change in volume due to the moving diaphragm and V_2 is the dead volume of the chamber (see Figure 4-4).

—, (4-1)

(4-2)

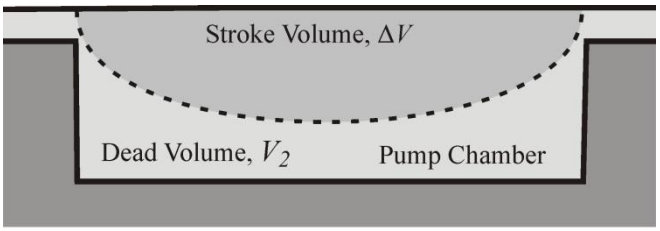

$$\Delta V = V_1 - V_2 \tag{4-3}$$

Figure 4-4: Drawing of diaphragm pump chamber.
The diaphragm compression ratio, ε, is the ratio of ΔV, the change in volume due to the moving diaphragm, and V_2, the dead volume of the chamber
Adapted from (Nisar, Afzulpurkar, Mahaisavariya, & Tuantranont, 2008)

The change in pressure, ΔP, is calculated with (4-2) where P_1 is the initial pressure, V_1 and V_2 are the initial and compressed volumes respectively. The change in pressure due to the moving diaphragm must be able to overcome a critical pressure difference, ΔP_{crit}, (4-3) as is required to open a valve, or overcome the back pressure in the biological system. For example, if the pumped fluid must open a check valve that requires 1 psi to open, then $\Delta P_{crit} = 1$ psi and $\Delta P > 1$ psi.

The formula for the minimum compression ratio for a gas pump, assuming isothermal behavior, is shown in (4-4) (Richter, et al., 1998), where P_0 is the atmospheric pressure. Equation (4-5) is the formula under the same conditions for a liquid pump. Where κ is the compressibility of the liquid (e.g. water: $\kappa = 0.5 \times 10^{-8}$ m^2/N).

(4-4)

(4-5)

Equation (4-5) assumes that no degassing occurs during operation and that the chamber is completely filled with liquid prior to pumping. Therefore, in order for the pump to be self-priming and 100% bubble tolerant, the conditions set by (4-3) will need to be enforced. These equations show that the higher the compression ratio the more pressure the pump can work against. The pressure, ΔP, can be thought of as the maximum pressure a diaphragm can produce in a single actuation cycle regardless of how much pressure is used for actuation.

4.2.2. Pump Fluidics and Diaphragm Mechanics

A parameter that captures the pressure loss through the system, as discussed in section 3.1, is the fluidic resistance, R. The formula for rectangular channels and chambers is given in (3-7). For channels with circular cross sections, the resistance is found from (3-9). The polyimide tubing used for system interconnections has an inner diameter, d, of 1.120 x10^{-4} m and the dynamic viscosity of water, μ = 1.0 mPa·s. This gives a value of 2.59 x10^{14} Pa·s/m^4 for the resistance per meter of tubing (pressure per volume flow rate per length). The pressure drop due to the restriction of the channel/tubing is dependent on the volumetric flow rate: the greater the rate, the greater the pressure loss. For the flow rate of Q = 100 nL/min through the tubing, the pressure drops 4.32 Pa/cm. Table 4-1 lists the resistance per cm for four fluidic features, rectangular channels, shallow chambers, square channels, and round tubing.

Also listed is the pressure drop per cm for each feature for 10 nL/min flow and for 100 nL/min flow. Note that the resistance and pressure drop per cm across the chambers is determined by the height and not the diameter therefore, total pressure drop across a chamber is directly proportional to the diameter. Figure 4-5 shows how the pressure drop per channel length decreases for increased height.

Fluid pumped through a chamber requires a pressure of 8.4 Pa, 1 cm of rectangular channel takes 838 Pa, and 15 cm of tubing needs 65 Pa, which adds to 911 Pa (< 1 kPa). This represents the largest pressure a chamber needs to supply in order to pump fluid out of the device and through the cannula. The lowest supply pressure calculated above for 500 µm chambers, ΔP = 900 kPa, is much greater than the critical pressure, so these chambers will be able to transfer momentum to the fluid. The actuation needs to

Table 4-1: Fluid Resistance and ΔP by Fluidic Feature for Various Flow Rates

Feature	Characteristic Dimension L	Pa·s/m^4	Pa /cm 100 nL/min	Pa/cm 10 nL/min
Rectangular Channel*	15 µm†	5.03x10^{14}	838.35	83.83
Shallow Chambers*	15 µm†	5.03x10^{14}	838.35	83.83
Square Channel‡	15 µm	2.37x10^{15}	3950.62	395.06
Round Tubing§	112 µm	2.59x10^{12}	4.32	0.43

* $R = 8\ \mu l/\pi L^4$
† Width > 2·L µm
‡ $R = 12\ \mu l/wh^3$
§ $R = 128\ \mu l/\pi d^4$

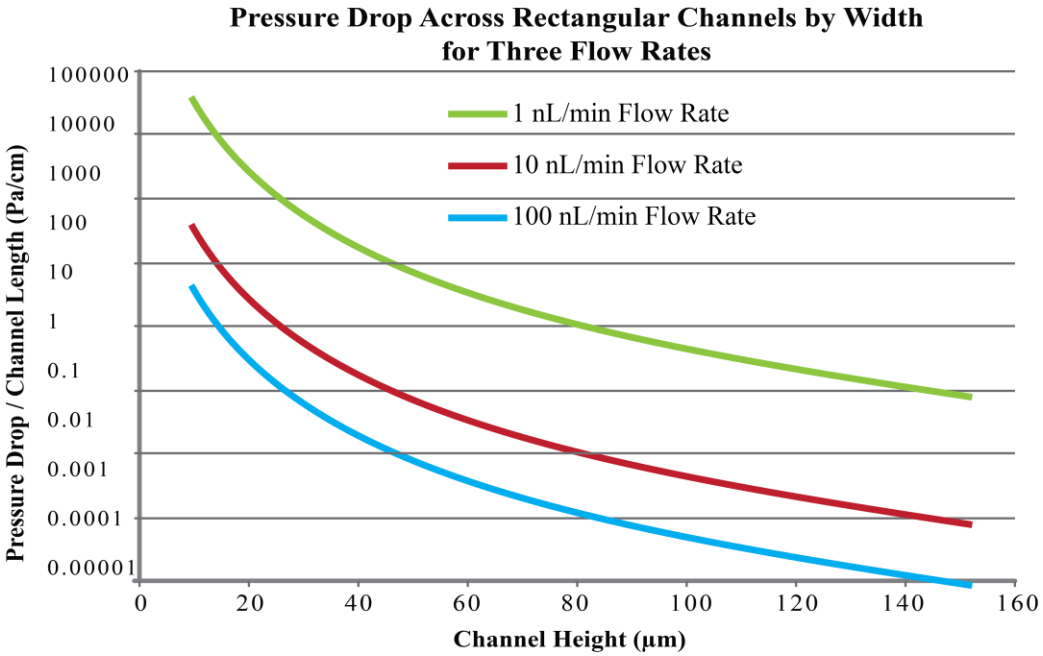

Figure 4-5: Pressure drop per cm along rectangular microchannels.
As the channels widen, the pressure drop diminishes $\Delta P \propto 1/L4$. As the flow rate increases the pressure drop increases proportionally, $\Delta P \propto Q$.

overcome the pressure lost in the system in order to provide any pumping energy at the output of the pump. These pressure drops include that lost in the channels and capillary tubing, the backpressure of the biological system, and the diaphragm actuation pressure. From the section above on fluidic resistance, the pressure lost in the capillary tubing and channels of the device is 1 kPa.

An initial goal 3 psi (20 kPa) for the diaphragm actuation pressure was used. With 5 kPa backpressure and 1 kPa lost in the device, due to fluidic resistance, and the 20 kPa required deflecting the diaphragms, this pump has sufficient compression ratio to allow for ΔP_{crit} = 1474 kPa (1500 kPa - 5 kPa - 20 kPa - 1 kPa) of potential pressure, assuming

Table 4-2: Calculation of Compression Ratio, ε, and Pressure Change, ΔP_D *for different diameter pump diaphragms*

Quantity (Units)	Symbol			
Diameter (µm)	D	500	800	1000
Height (µm)	H	15	15	15
Volume (nL)	V_1	2.95	7.54	11.78
Dead Volume (nL)	V_2	0.29	0.47	0.59
Stroke Volume (nL)	ΔV	2.65	7	11.2
Compression Ratio	ε	9	15	19
Induced Pressure Change (kPa)	ΔP_D	900	1500	1900

P_0 = 101 kPa

the actuation mechanism can supply enough pressure. Using values from Table 4-2 it can be shown that any diaphragm diameter between 500 µm and 1000 µm will provide sufficient compression to pump fluid through the fluidic system against backpressure ≤ 5 kPa.

Visual inspection of an initial design revealed a dead volume, V_2, with a roughly triangular cross section with a height of 15 µm and a width of 25 µm around the circumference of the chamber. The stroke volume, ΔV, is the difference between the chamber volume, V_1, and the dead volume, V_2. For an 800-µm diameter chamber, ΔP_D= 1500 kPa. This indicates that the estimated compression ratio of this pump is high enough to overcome a total upstream pressure of 1500 kPa and since the conditions for gas pumping are met, the system has been designed to be tolerant of bubbles and in fact can be self-priming when used peristaltically.

The available actuation force and the processing parameters determine the diaphragm thickness but as one goal is to reduce the required actuation force, the diaphragms should be made as thin as possible. The equation for large deflections, where the deflection is greater than the diaphragm thickness, is shown in (4-6) and (4-7) from (Timoshenko, 1940). This takes into account the strain on the diaphragm undergoing large deflections.

(4-6)

$$D_f = \frac{Eh^3}{12(1-\nu^2)} \tag{4-7}$$

Table 4-3: Constants used to calculate the Diaphragm Deflection

Symbol	Quantity	Value	Units
q	Pressure	6.89×10^3	Pa
a	Radius of circular diaphragm	250	µm
h_D	Thickness of diaphragm	0.4 to 10	µm
v_{Si}	Poisson's Ratio SiO_2	0.40	
v_P	Poisson's Ratio Parylene C	0.30	
E_{TEOS}	Young's Modulus SiO_2 *	7.3×10^{10}	N/m^2
E_P	Young's Modulus Parylene C *	3.20×10^9	N/m^2

* Values for bulk material, (Pasupuleti & Sahin, 2007) report much lower values for films < 1 µm. $E_{TEOS} = 1.0 \times 10^{10}$ N/m^2

The deflection, w_0, is measured at the center of the diaphragm, ΔP_D is the pressure across the diaphragm of radius a and thickness h (see Figure 4-6). D_f is the flexural rigidity of the plate. E is the Young's modulus and ν is the Poisson's ratio. To find the required trans-diaphragm pressure, ΔP_D, to deflect a composite diaphragm a given amount, the ΔP_D, for all of the materials is calculated. The total pressure to deflect the diaphragm is derived by adding the pressures assuming the principle of superposition holds. This approximation ignores any interaction between the materials, which could add to the flexural rigidity but will suffice for an approximation.

Using (4-6) and (4-7), the deflection at the center of diaphragms, for various thicknesses of potential masking materials (TEOS and Aluminum), and the encapsulating Parylene C, under 3 psi of evenly spread pressure, as is the case during pneumatic or hydraulic actuation, is calculated with the parameters in Table 4-3.

Figure 4-7 shows that the deflections decrease for increasing diaphragm thickness, but the diaphragm diameter has a greater influence on the deflection. Later, in Chapter 5, diaphragm diameters will be determined based on actuation selection as it may be beneficial to use a diaphragm of up to 1000 µm in diameter in order to

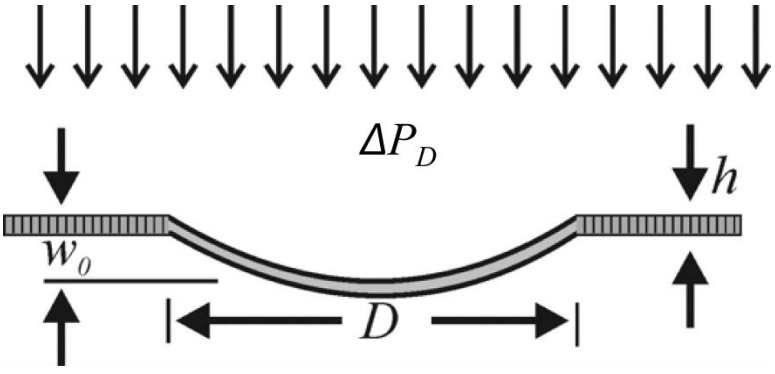

Figure 4-6: Diagram of parameters for diaphragm deflection. Large deflection ($w_0 > h$) of diaphragms of diameter D under trans-diaphragm pressure ΔP_D.

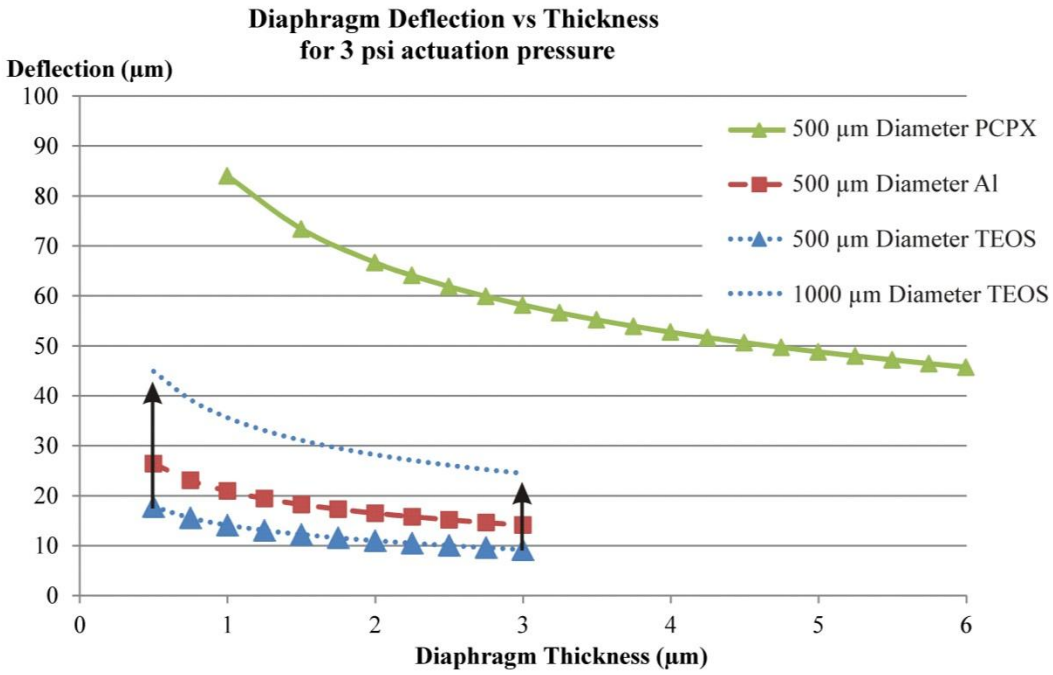

Figure 4-7: Graph of the derived deflection diaphragms.
Deflection for TEOS, Parylene C, and Aluminum diaphragms.
The change in deflection for the 500-µm to the 1000-µm diameter TEOS diaphragms indicates that the diaphragm diameter has more influence over deflection than does the diaphragm thickness.

reduce diaphragm actuation pressure, but for the deflection tests in Section 4.4, 500-µm diameter diaphragms were used.

4.2.1. Cross Hatch Pattern (size / frequency)

The lower end for the size of the apertures is determined by the etch rate of Si through small openings and by the lithographic resolution, < 1 µm. (Sugano & Tabata, 2002) studied the effects of XeF_2 etching and reported that the Si etch rate slows dramatically with decreasing aperture size. Small openings require less Parylene C to fill, resulting in thinner diaphragms; this limits the aperture size at the upper end by the thickness of the diaphragms. In addition to the initial deposition thickness required to fill the openings, subsequent polymer thickness will add to the strength of the diaphragms by adding material to the weak points in the center of each etch hole.

Equation (4-8) relates the total diaphragm thickness, h_D, to its component layers; the Parylene C thickness needed to fill the hole, h_P; the thickness of the TEOS, h_T; and the thickness of the Parylene C deposited after the hole has been filled, h_x, which adds to the strength of the diaphragm. Equation (4-9) is a quantitative guideline for the width of the

openings in the TEOS, W_a, based on the total thickness of the diaphragm, the TEOS thickness, and the strengthening layer of Parylene C.

(4-8)

(4-9)

Figure 4-8 is an illustration showing how a 2 µm Parylene C deposition is needed to just occlude a 4 µm hole and how an additional 1 µm of polymer could be used to strengthen the diaphragm. (Giacchino & Yu-Chong, 2008) used an 8.5-µm deposition of Parylene C to fill 7.5-µm diameter holes.

4.2.2. Anchors

A process for forming anchors without additional processing steps and without depositing further Parylene C thickness was developed. Anchors placed in the field regions between fluidic features can be used to enhance the adhesion of the Parylene C during dicing. Figure 4-8 is a drawing of the cross-section of an anchor showing how the TEOS mask captures the polymer. The openings defining the chambers and channels anchor the Parylene C to the TEOS via the encapsulation that occurs during the diaphragm formation process. The Parylene C is deposited into the isotropically etched region under the TEOS opening and holds the polymer film to the TEOS. These are patterned with the same mask as the holes used to create the fluidic channels and chambers and thereby do not add to the complexity of the fabrication. If the width of the anchor openings is less than or equal to the openings that define the fluidic features, then the Parylene C thickness does not have to be increased as was the case for (Giacchino & Yu-Chong, 2008).

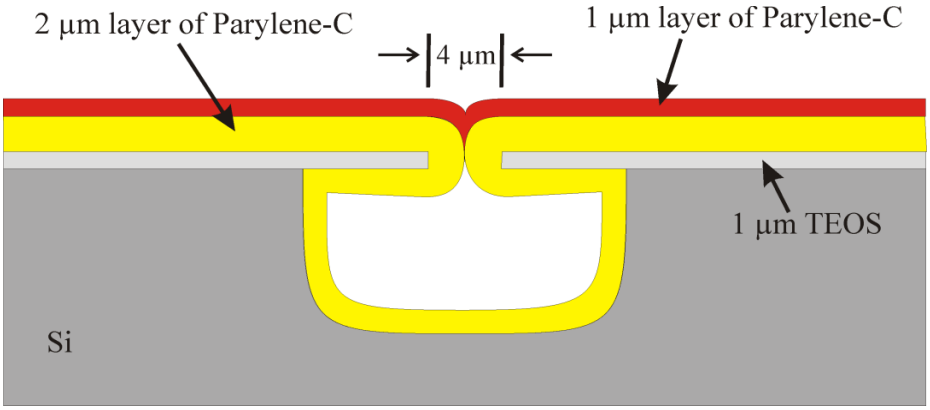

Figure 4-8: Drawing of the cross-section of a 4 µm diameter Parylene C anchor.
The Parylene C polymerizes into the wide pit etched into the Si by the XeF_2 etch. The small opening in the TEOS prevents the Parylene C from pulling out acting as an anchor.

4.3. Fabrication

Wafers were cleaned (RCA) and 1 µm of TEOS SiO_2 was deposited (P5000, 290 W, 113 s). The TEOS was patterned to define fluid channels, interconnects, and diaphragms then etched (Drytek Quad, Ar: 35 sccm, CHF_3: 65 sccm, O_2: 5 sccm, 200 W, 70 mtorr) to create the hard mask. The Si-etch process can be done in multiple steps to achieve different etch depths for the chambers/channels and the interconnections. Figure 4-9 (a) shows the photoresist pattern for a channel (wide pattern) transitioning to an interconnect (narrow pattern). The narrow interconnect pattern experiences two etches and as a result becomes as wide as the shallow etched wide channels due to the isotropicity of the etch. Figure 4-9 (b) is a SEM image of the openings in the TEOS that allow for the etch of the underlying silicon.

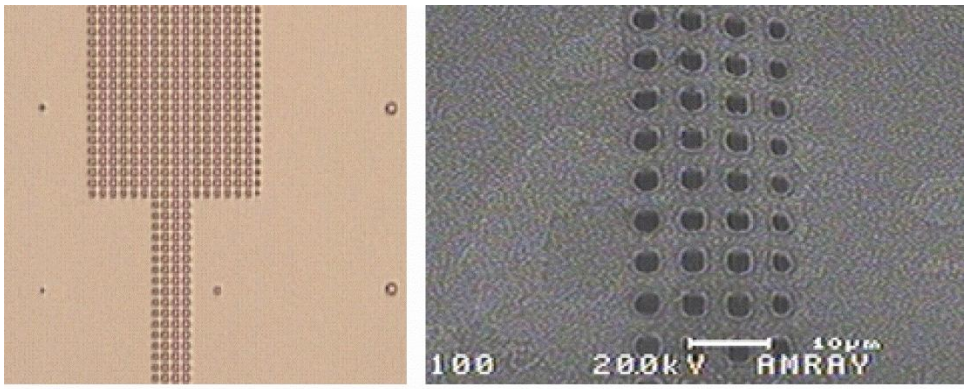

Figure 4-9: Micrographs of TEOS SiO_2 patterned for Channel etching.
(a) SEM of photoresist patterned over TEOS prior to etching. The wide channel will be protected by photoresist and experience only a shallow Si etch and the narrow pattern will be etched deeply to formed the interconnects. Both patterns lead to equal width channels due to the isotropicity of the XeF_2.
(b) SEM image showing 1-µm holes etched in TEOS through which the underlying silicon is etched.

Figure 4-10 is an illustration of the external interconnect and the channel/chamber of a device. Note the deep etch at the interconnect end due to the two step etch process. Channels and diaphragms were protected with photoresist while interconnects were deeply etched (140 µm) in XeF_2. Periodic visual inspection was required to determine when the appropriate depth had been reached as the XeF_2 etch rate of silicon is dependent on opening size as the etch is transport limited (Brazzle, Dokmeci, & Mastrangelo, 2004) as well as the amount of silicon exposed to the available XeF_2 gas in the etch chamber.

With the protecting photoresist removed in an O_2 plasma (a wet etch could damage delicate TEOS

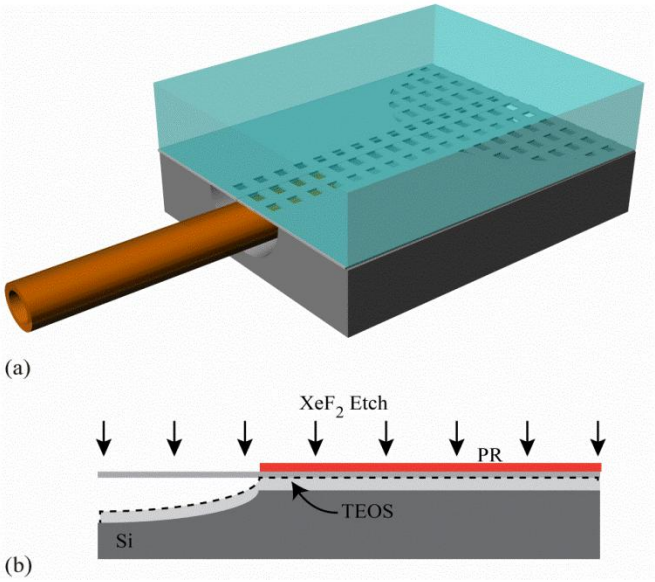

Figure 4-10: Drawing showing how the in-plane interconnects interface with the pump chamber.
(a) Image of interconnect with polyimide tubing inserted. (b) Two XeF_2 etches are performed, the first etch (dotted line) forms the deep interconnects while the photoresist (PR) protects the chamber areas. After the PR is removed an additional etch forms the chambers and channels.

structures) the channels and chambers were etched in XeF_2 to a depth of 20 µm. The interconnects are further etched during this step and the additional depth has been accounted for in the timing of the initial deep etch. The photoresist was removed and a diaphragm was formed with a 4.5-µm deposition of Parylene C, which also coated the micro fluidic channels and chambers. The 20-µm chambers are coated with Parylene C both above and below reducing the chamber depth to 15 µm for the devices with 4-µm wide openings.

4.4. Diaphragm Deflection And Long Term Test

For verifying the diaphragm deflection, plastic plena were fabricated from acrylic (1 mm thick) and adhered to a chip using cyanoacrylate. The chip contains seven diaphragms each with an inlet and outlet channel. A nanoport fitting (Upchurch, Scientific, Oak Harbor, WA, USA) was glued to a glass slide with a hole drilled to allow pneumatic access.

The stack of device/plenum/glass (see Figure 4-11), was viewed under a Wyko interferometric microscope (Veeco, Plainview, NY USA) while pressure was applied to the plenum. Since the diaphragm is under one layer of glass, the interferometric microscope requires a similar sample of glass in the optical path in order for the interference to produce results so a small chip, ~20 mm^2, of a glass slide was affixed to a removable aperture and placed in the Wyko. The Wyko allows for deflection measurements through the microscope slide. An NPC-100 pressure sensor (GE Novasensor, Inc., Fremont, CA) was used to record the pressure required to deflect the diaphragm. Figure 4-12 shows images from the Wyko of a diaphragm in the relaxed state at, ΔP_D = 0 psi and deflected

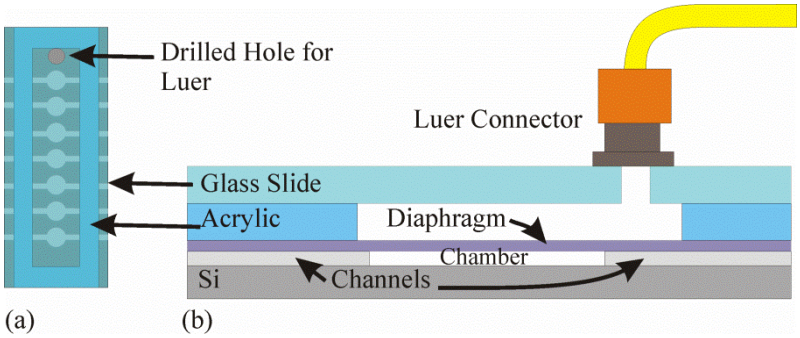

Figure 4-11: Illustration of cross-section of test fixture for testing diaphragm deflection.

Visual inspection with Wyko interference microscope allows for correlation between actuation pressure and deflection at the center of the diaphragm for comparison to theory.

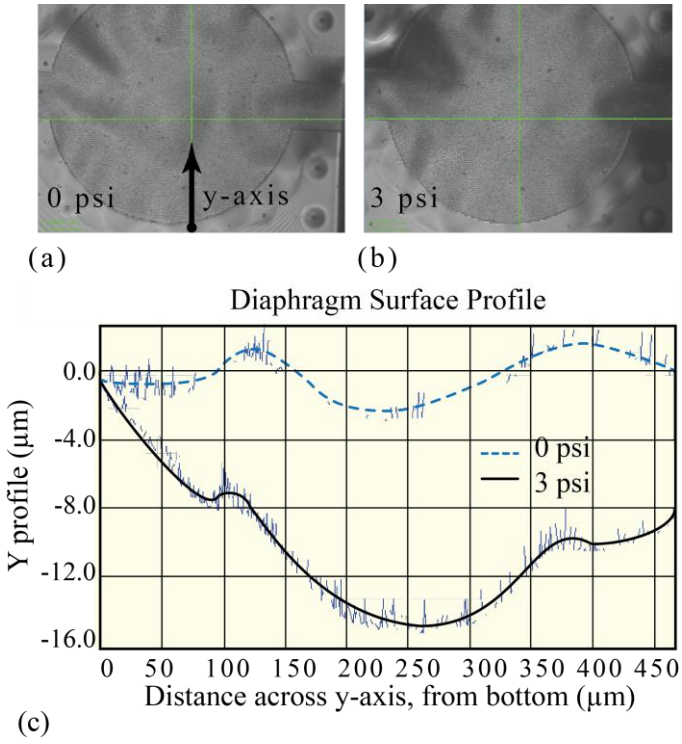

Figure 4-12: Membrane deflection images and graph.
(a) and (b) are images from the Wyco interferometer of the pump diaphragm at rest, 0 psi, and at 3 psi.
(c) shows the data from the Wyco showing the maximum deflection at the center of a 500-µm diameter diaphragm.

downward 15 µm at the center of the diaphragm.

An actuation pressure of 3 psi was needed to fully deflect a 500-µm diameter diaphragm of 1-µm TEOS, and 4.5-µm Parylene C. Using (4-6) and (4-7) and the superposition of two diaphragms (one of TEOS and one of Parylene C) gives an actuation pressure of 3.3 psi for a 15-µm deflection, which is an error of 10%. The approximation is performed by modeling the pressure required to deflect a 1-µm thick TEOS diaphragm and a 4.5-µm thick Parylene C diaphragm separately, and adding the two pressures using an average thickness, where the average thickness is equal to the film thickness times the percent coverage (75%). Potential sources of error include non-uniformity in film thicknesses, and the non-planarity of the composite film.

Long-term testing has been conducted on seven diaphragms using the same test chips as for the Wyko tests described above with a plenum formed with a gasket and an acrylic plate (see Figure 4-13). Compressed air was fed into a regulator (10 psi indicated on gauge) connected to a relay controlled by a triangle waveform from a wave generator (10 Vpp at 1 Hz). The solenoid passed the 10-psi air pulses to the plenum over the diaphragms and bled to atmosphere when turned off.

Visual access through the acrylic plate allowed detection of the diaphragm deflection. One inlet/outlet side of the channels was filled with water forming an air/water interface at the distal end of the channels that could be watched during deflection (see the call-out in Figure 4-13). The interface could be seen to move back and forth in synchronization

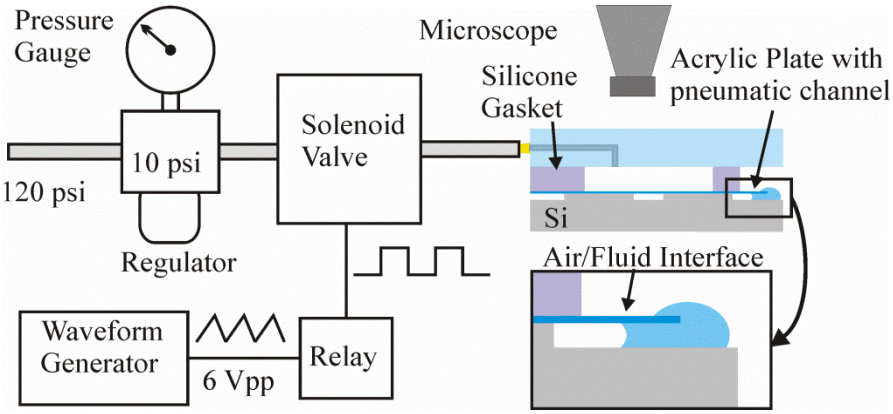

Figure 4-13: Drawing of the long- term test set-up.
A waveform generator controls a solenoid allowing compressed air, 10 psi, to pressurize the plenum fully actuating the diaphragm. The call-out shows a close up of the air/water interface that was examined on a weekly basis to verify the integrity of the diaphragms.

with the air pulses. To ensure the diaphragms were still intact, steady pressure was applied to deflect the diaphragm. Leaky diaphragms would have allowed air to pass pushing the water out of the channel. The diaphragm was inspected under a microscope on a weekly basis and upon completion of the long-term test. During the weekly steady state pressure tests, the air/water interface did not move indicating intact diaphragms. Testing was conducted for 307 days with over 26 million (26,524,800) actuations on seven diaphragms with no failures. This is the equivalent of over 185 million diaphragm actuations without a single failure.

4.5. Conclusion

Diaphragms over pump chambers were successfully created and deflected. Figure 4-14 is a SEM image of the *in situ* formed diaphragm, showing a Parylene C diaphragm over the TEOS framework. The dimples in the surface correspond to the holes in the TEOS hard mask. During the diaphragm formation process, the entire fluidic space is coated with a thin layer of Parylene C, sealing the whole microfluidic structure with a biocompatible coating (see Figure 4-15). A process for creation of diaphragms over micro cavities with simultaneous coating of the microfluidic channels has been demonstrated allowing integration of a biocompatible fluid flow path.

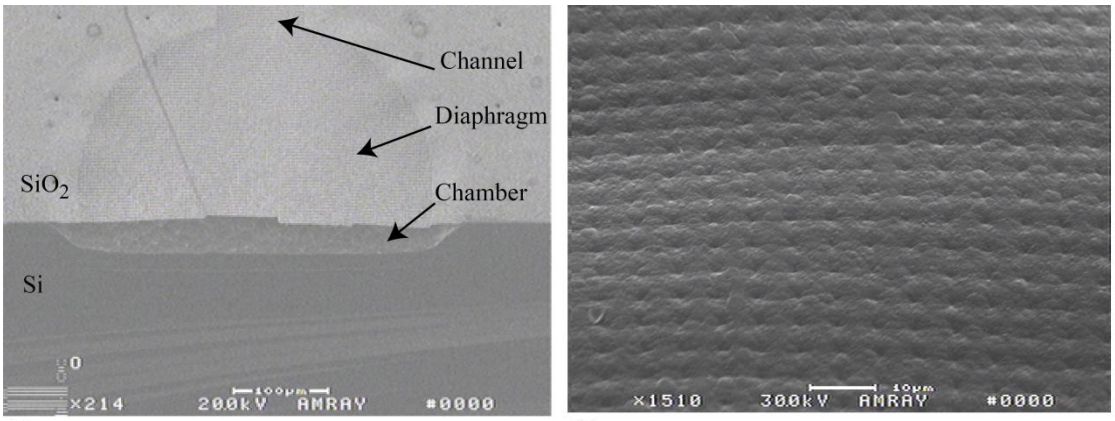

Figure 4-14: SEM images Parylene C Diaphragm.
(a) SEM images showing fluidic chamber under Parylene C Diaphragm.
(b) SEM of Parylene C Diaphragm formed over TEOS framework. Dimples in the Parylene C surface correspond to the etched holes in the underlying TEOS framework

With the flow path, including pump diaphragms, in place, the next step is to determine the method by which actuation momentum is transferred to the diaphragms. A pump with 500-µm diameter chambers will require an actuator capable of overcoming the deflection pressure (20 kPa), the pressure lost in the fluidics (1 kPa), and the backpressure of the system (5 kPa) for a total of 26 kPa. Larger diameter pump chambers would require even less output from the actuator so 26 kPa is a good minimum requirement for actuation output.

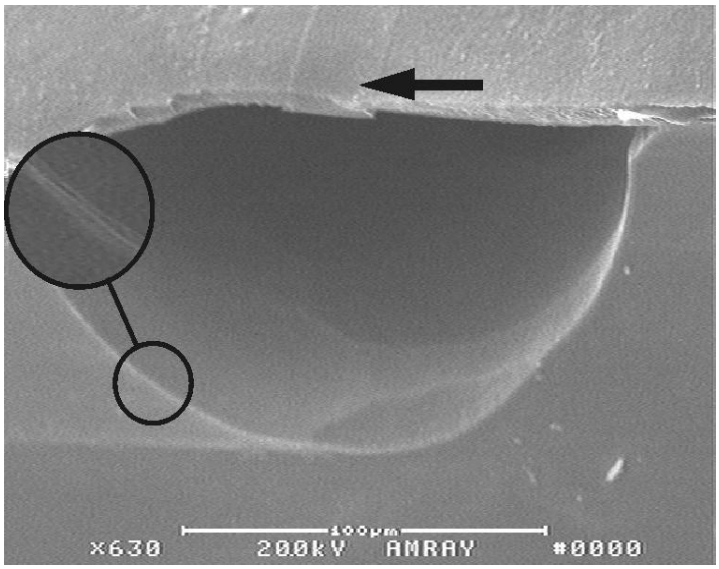

Figure 4-15: SEM image showing fluidic chamber under Parylene C Membrane.
Arrow indicates location of openings in TEOS. Blow out shows layers of Parylene C deposited on the surface of the fluidic channel. © 2010 IEEE Reprinted, with permission, from (Johnson, Waldron, Frisina, & Borkholder, 2010)

Chapter 5 Actuation Mechanism

What makes life dreary is the want of a motive.
George Eliot

Chapter 1 concluded that a diaphragm pump is the most suitable for pumping the wide range of compounds needed for auditory therapy development, but to power the pump, an actuation mechanism needs to be selected. A number of actuation mechanisms may be used to motivate the diaphragms and important properties of these will be discussed and include, actuation voltage, delivered pressure, pump rate, and known issues that arise with certain types of devices such as excessive heat output.

5.1. Actuation Types

The actuation mechanism can operate with a separate working fluid that transfers momentum to the diaphragm, which in turn transfers momentum via the diaphragm to the pumped fluid. Alternatively, a mechanical actuator such as a shape-memory alloy, relying on thermal deformation (D. Xu et al., 1999), can be utilized to impart a reciprocating force on the pump diaphragm. Table 5-1 compares the manner of pumping and the relevant properties, listed above, for a number of actuation mechanisms, both dynamic and mechanical, presented in the literature.

Electromagnetics that rely on an external magnets (Feldmann, et al., 2008) can be attractive because the power and control electronics required for actuation are provided externally, eliminating the need for integrated control electronics and power source. However, the required sequencing of diaphragm deflection for peristalsis is impossible to achieve with an externally applied magnetic field.

Table 5-1: Micropump Actuation Mechanisms

Actuator	Method	Voltage	Pump rate	Pressure	Issues	Reference for listed device
Composite/Polymer materials	Heat or Voltage Deformation	6 V	1000 µL/min	1h Pa	75 °C required to deform	(D. Xu, et al., 1999)
Electro-static	Diaphragm driven by electrostatic forces	200 V	850 µL/min	31 kPa	High Voltage	(Zengerle, Ulrich, Kluge, Richter, & Richter, 1995)
Piezo-electric	Diaphragm driven by piezo material	100 V	NR	520 Pa	High Voltage	(L.-S. Jang et al., 2007)
Electro-magnetic	Magnet incorporated on diaphragm driven by electromagnet	NR	NR	NR	Requires valves *	(Feldmann, et al., 2008)
Electro-Osmosis	Ions drag water across an ion-specific membrane between two chambers	62 mV	146 µL/min	69 kPa	Complex fabrication	(Uhlig, Graydon, & Zingg, 1983)
Electrolysis	Pressure of gas bubbles from electrolysis of water	4.5 V	24 nL/min	110.1 kPa	control issues, sensitive to backpressure	(D. A. Ateya, et al., 2004)
Magneto Hydro-Dynamic	Voltage source generates distributed force; external magnetic field motivates conducting fluid.	1-2 Vpp	1.54 µL/min	NR	Limited lifetimes, electrolysis affects flow rate	(Sadler et al., 2001)
Thermopneumatic	Joule Heating causes volumetric change in material	5 V	8.74 µL/min	NR		(Chia, Hsin-Hung, & Yao-Joe, 2011)
Phase Change	Pressure from the change of phase volumetric	2 V	0.75 µL/min	5 MPa		(Boden, et al., 2008)
Continuous Electro-Wetting	Electric fields change the wetting of a surface which moves fluid	2.3 Vpp	63 µL/min	600 Pa	Complex fabrication	(Yun et al., 2001)

NR Not reported
* Chambers cannot be actuated out of sync and peristalsis is not an option

Electrolysis (D. A. Ateya, et al., 2004; Neagu, Jansen, Gardeniers, & Elwenspoek, 2000) can generate sufficient pressure (180 kPa) for the pump requiring greater than 26 kPa, from Section 4.5. However, none of the electrolysis pumps presented in the literature are capable of reversing the direction of the flow, a requirement for actuating, and de-actuating, a diaphragm, as they require the generated gas bubbles to be re-adsorbed. Actuators relying on the shape memory properties of composite/polymer materials (Guo, Nakamura, Fukuda, & Oguro, 1996) have not been shown to deliver sufficient pressure (0.1 kPa).

Actuation mechanisms with promise include magnetohydrodynamic (MHD), electro-osmotic (EO), thermopneumatic, and phase-change materials. Magnetohydrodynamic induces flow on a conducting fluid by applying both an electric field and a magnetic field, as shown in Figure 5-1. The flow direction is perpendicular to both fields, which can be either AC or DC. The directionality of the flow may be reversed by changing the polarity of just one of the fields. These suffer from gas forming (Woias, 2005) and low pumping pressure with DC current; (J. Jang & Lee, 2000) were only able to pump against 177 Pa (0.025 psi) at 60 V.

An electroosmotic (EO) mechanism is a good candidate as the parameters for flow rate and pressure are in line with the requirements for the system under design. Figure 5-2 is a diagram of an EO pump, showing the operation of such a device. The inner walls of the fluidic channel are positively charged attracting negative ions to form a dense charge layer, this layer in turn attracts a second positive layer called the diffuse layer. When a voltage is applied across the channel, the positive ions in the diffuse layer are motivated towards the anode dragging water

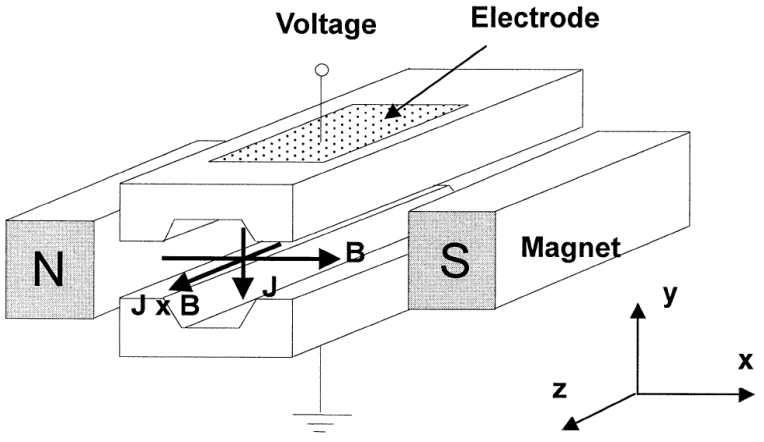

Figure 5-1: Drawing of Magnetohydrodynamic micropump. Flow of the conducting fluid is generated by the Lorentz forces acting perpendicular to the electric and magnetic fields (J×B) where J is the electric field, B is the magnetic field. Magnets may be permanent or electric. (J. Jang & Lee, 2000) used with permission from Elsevier Limited

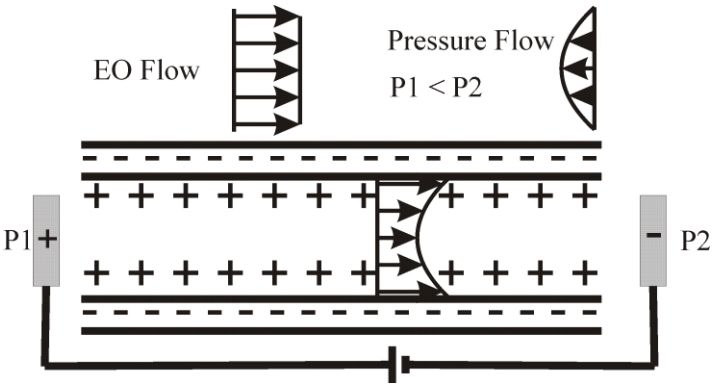

Figure 5-2: Schematic diagram of double charge layer leading to Electro-Osmotic (EO) flow.
The negative ions are drawn to the surface of the channel forming the first layer. The positive ions in the diffuse layer are motivated by the voltage across the channel, dragging water molecules with them. Adapted from (Nan-Chyuan & Sue, 2007)

molecules along the way. Flow can be reversed by switching the polarity of the applied voltage. A planar EO pump using an ion exchange membrane has been presented (Brask, Kutter, & Bruus, 2005), which was able to pump borate buffer (pH = 9.2, concentration of 1 mM to 100 mM) at 6 µL/min against 455 kPa with 30 V activation. By scaling down the voltage, pump rates, and pressures this actuation device may be able to be scaled to fit this project.

Micropumps with thermopneumatic actuators have been reported (Chia, et al., 2011) that have low temperature elevation, 22.9 ºC above the actuation diaphragms, and 88.8 ºC directly over the heaters. These pumps are unable to pump against backpressure greater than 0.072 psi (0.496 kPa), which is insufficient where the pump being designed needs to pump against 5 kPa of backpressure plus losses in the fluidic structures. This shortcoming can be overcome by careful design of the compression ratio of the pump chambers as described in Section 4.2.1. Pumps operating with phase-change materials such as that presented by (Boden, et al., 2008) using paraffin wax can produce over 5 MPa of pressure pumping at 1 µL/min with 60 mA (see Figure 5-3). The wax undergoes not only thermal expansion but also an additional expansion due to the change in phase. In the case of some materials, like wax, there is a significant increase in volume as the material melts (> 10 %/20 ºC). This device required a cooling flange to help extract heat from the wax indicating that excess heat is being generated to achieve these pressures and flow rates. As with the electroosmotic device, this phase-change device could be scaled to the flow rates of the system (< 100 nL/min) and reduce the required heat and current. While both the electroosmotic and thermal, including phase-change and thermopneumatic actuators, could be scaled and adapted to the pump, the relative simplicity of thermal actuation

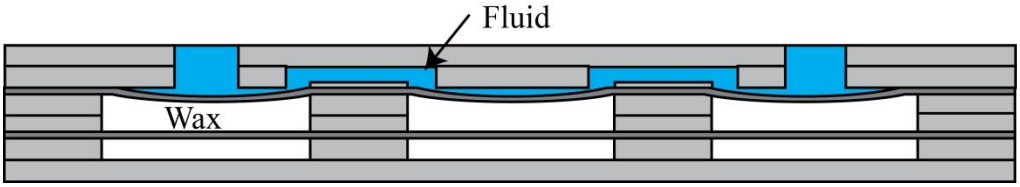

Figure 5-3: Illustration of cross-section of phase-change material actuated peristaltic pump.
The wax is heated from below and expands to push up on the diaphragm pushing fluid and closing the valve. High pressures are possible with this device (nearly 1 MPa) and a pump rate of 1 µL/min was reported.
Adapted from (Boden, Hjort, Schweitz, & Simu, 2008)

leads to the decision that this is best for integration with the peristaltic pump. Both thermal pneumatic and phase change actuation will be discussed.

5.2. Thermal Actuation

This section investigates thermal actuation mechanisms: Thermopneumatic and thermal phase change are compared for use with an underlying diaphragm chamber pump. All the devices investigated use the same design basics with the actuation energy supplied by joule heating to an integrated resistor. Thermal actuation uses the heat to increase the volume of a material by thermal expansion. The heated material in a sealed plenum expands forcing the diaphragm into the pump chamber based on the material's coefficient of thermal expansion.

The other type of thermal actuation being examined relies on the phase change of the material and not the single phase thermal expansion. Wax is an example of this type of actuation where the volume of the wax increases beyond that provided by the thermal expansion as it changes phases from solid to liquid. Most phase change materials increase in volume when transitioning from the solid phase to the liquid phase, but there are exceptions. Water, when it freezes into ice, increases in volume in an exothermic process. An exothermic process releases energy in the form of heat (e.g. negative enthalpy change, $-\Delta H$) and includes freezing water, condensing water vapor, and splitting of an atom. Gallium (Ga) also increases in volume when transitioning from a liquid to a solid. This material enables an exothermic phase change actuator, which means that the actuating force is initiated by the removal of heat from the gallium as opposed to an endothermic actuator that takes in energy to expand.

These three materials are considered suitable candidates for filling the plena and providing the pumping momentum. The first to be discussed is air, which relies on endothermic expansion of the gas. The second, paraffin wax, relies on the endothermic expansion during the solid to liquid phase change. Both of these materials have been used successfully to actuate pumps (Boden, et al., 2008; Grosjean, Xing, & Yu-Chong, 1999) and valves (Carlen & Mastrangelo, 2002; X. Yang, Grosjean, Tai, & Ho, 1998). The third material, gallium, relies on exothermic phase change expansion. This exothermic expansion will allow the actuator to hold the pump diaphragm in the closed position blocking flow with zero energy expenditure. The energy per pumped volume for the three materials was investigated using a parameterized finite element analysis (FEA) model using COMSOL 3.5a (COMSOL, Inc., Burlington, MA).

5.3. Validation of COMSOL Model for Thermal Analysis

The underlying diaphragm structure is comprised of a diaphragm-covered chamber with inlet and outlet channels. The chambers are approximately cylindrical in shape and the heater plenum is rectangular (see Figure 5-4). Equation (5-1) and (5-2) were used to find the plenum volume and the stroke volume, where *w*, *h*, and *l* are the width, height, and length of the plenum respectively.

(5-1)

(5-2)

C_E is the percentage the material expands, which for thermopneumatic actuation is simply the coefficient of thermal expansion and for phase change is the percentage of volume change due to thermal expansion and the phase change.

The temperature required to increase this volume of air by the stroke volume is calculated using the following equations.

(5-3)

(5-4)

P_2 is the pressure in the actuated plenum, P_1 is the pressure in the relaxed plenum, V_1 is the relaxed volume of the plenum, ΔV is the increase in plenum volume during actuation,

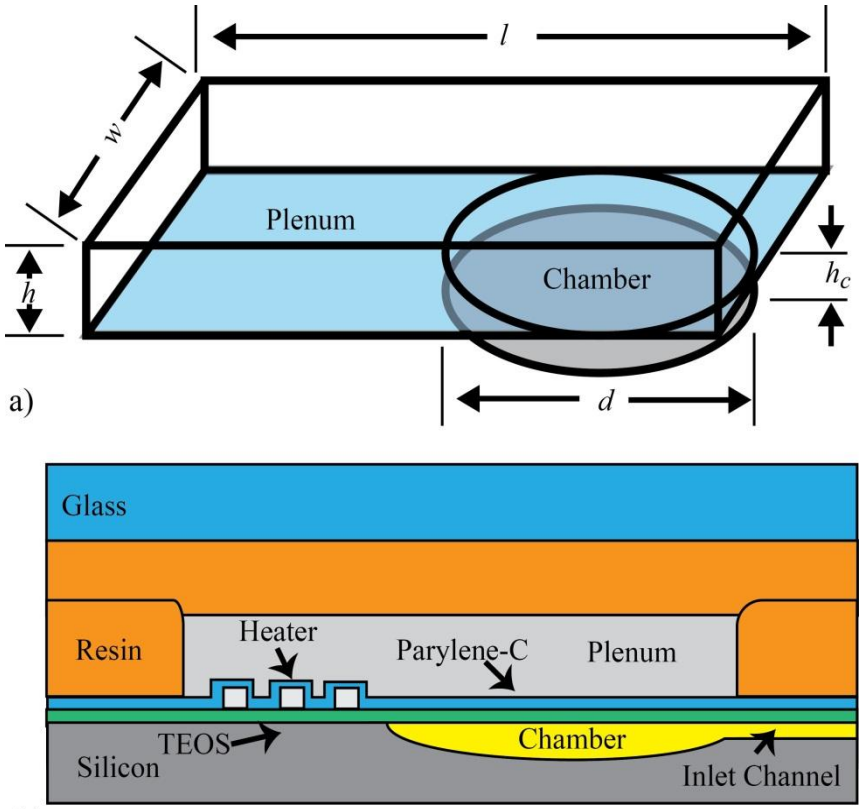

Figure 5-4: Drawing of heater plenum and pump-chamber.
(a) Drawing showing the geometry of the plenum and pump chamber. (b) Cross-section showing the working structure of the actuation. The material in the plenum volume expands to push a diaphragm spanning the chamber to push into the chamber volume. The momentum of the expanding material is transferred to the chamber volume pushing it out of a channel connected to the chamber.

T_1 is the temperature of the system, and ΔT is the change in temperature in the actuated plenum. Making $V_1 >> \Delta V$, decreases the temperature required to effect the required pressure change, where ΔV is the stroke volume. The energy, Q, needed to achieve this temperature rise, ΔT, in the air in the plenum is calculated with (5-5).

(5-5)

(5-6)

The specific heat, c, and the mass, m, of the air are given in Table 5-2. For phase change devices the thermal expansion is not sufficient to actuate the diaphragms, the phase change itself causes the necessary changes in volume. The energy needed to activate these devices includes the heat to raise the temperature of these materials and the energy to cause the phase change, the heat of fusion.

Table 5-2: Parameters for calculating the heat and energy for thermopneumatic actuation

Symbol	Quantity	Value	Units
P_1	Non-actuated plenum pressure	104	kPa
P_2	Pressure in actuated plenum	130	kPa
T_1	Temperature in animal model	37	°C
ΔV	Stroke volume	12	nL
m	Mass of air in plenum	1.35×10^{-10}	kg
c	specific heat of air	1.005	kJ/kg·K

Using (5-5) and the values in Table 5-2 gives the energy, $Q_{air} = 7.33 \times 10^{-3}$ mJ to heat a 120-nL air plenum to 363 K (90 ºC). The 120 nL plenum volume and 90 ºC temperature were chosen arbitrarily for the validation of the COMSOL model. The value calculated, $Q_{air} = 7.33 \times 10^{-3}$ mJ, is the energy to raise the temperature of the air in the plenum and the heater element only and does not account for heat lost to the surrounding device. This model was used to validate the use of COMSOL for modeling more complicated structures. The use of COMSOL for this analysis was validated with two simple systems representing aspects of the whole device.

A 2D COMSOL model (COMSOL 3.5a) of this insulated static analysis was constructed consisting of one domain, the air plenum (1 mm by 40 µm). The model used the material properties in Table B-1 with 672 triangular mesh elements. The FEA was performed and verified that 7.33×10^{-3} mJ for 1 second heats the plenum to an average temperature of 362.46 K (ΔT = 52.46 K), which is within 0.15% of the calculated value. This provides confidence that the geometry and thermal equations of the COMSOL model was configured correctly.

A transient thermal analysis was performed with the calculations for thermal heating in thermopneumatic actuation being shown indicating where additional work needs to be done for phase change. This transient thermal analysis employed the same physical model used above with the inclusion of new boundary conditions to simulate the heat transfer from the plenum into the device. The pressure in the pump chamber is equal to atmosphere, 101 kPa, plus the backpressure, 5 kPa, for a total pressure of P_1 = 106 kPa. This pressure exists inside the plenum above an open (non-activated) diaphragm, which is in fluidic contact with the biological system. The size of the air plenum is determined primarily by the expansion coefficient, C_E of the material and the need to keep the air temp low and at the same time reduce power usage.

Table 5-3: Calculated Values for Thermopneumatic Actuation

Diameter (μm)	500	800	1000
Act. Pressure (psi)	3	1.5	1
ΔV (nL)	2.95	7.54	11.78
Min. plenum, V (nL)	29.5	75.4	117.8
T for min. plenum (ºC)	172	93	74
T 120 nL (ºC)	75	74	74
T 240 nL (ºC)	59	58	58

P_1 = 101 kPa, P_2 = 108 kPa

Table 5-3 shows the temperature values calculated using (5.4) for three chamber diameters, 500 μm, 800 μm, and 1000 μm, and different plenum sizes. The table shows that keeping the temperature low is possible by increasing the plenum size, but the actuation temperature relies less on the diaphragm actuation pressure, which is controlled by the chamber diameter as large diaphragms require less pressure, $\Delta P_{D,}$ to actuate as discussed in Section 4.2.2.

Figure 5-5 shows how the plenum air temperature and the actuation power vary with the size of the plenum for pumps with 800-μm diameter diaphragms. This graph indicates that in order to reduce temperature, the size of the plena should be increased, but there is a trade off with power.

A MATLAB analysis of the one-dimensional diffusion/dissipation equations for heat in an air chamber is first considered (see Figure 5-6).

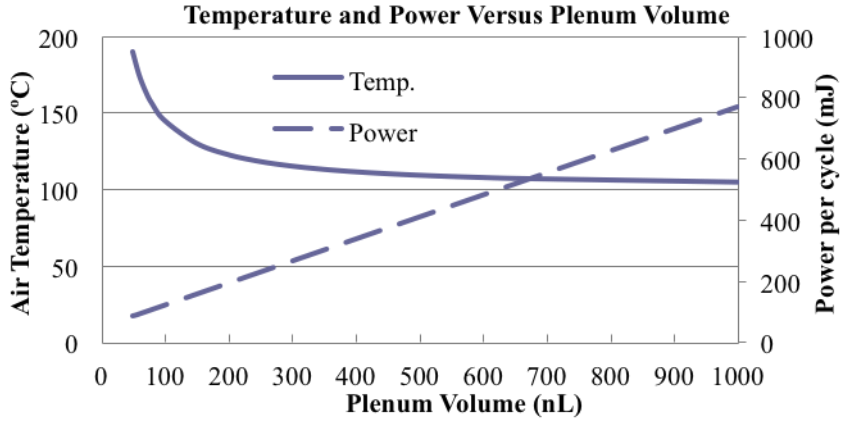

Figure 5-5: Graph showing the air temperature and power v. plenum volume.
Temperature in the expansion plenum needed to fully actuate an 800-μm diameter diaphragm and the power required to reach this temperature are graphed against the volume of the plenum. The temperature drops exponentially while the power increases proportionally. (values for 800-μm diameter diaphragms using (5-5) and (5-6))

(5-7)

(5-8)

(5-9)

(5-10)

(5-11)

In Equation (5-7), T is the temperature, α is the thermal diffusivity (19 mm^2/s). The analysis assumes that at time $t < 0$ the chamber is set to equilibrium with an average temperature of 90 ºC. The system has a bulk temperature of 37 ºC, the body temperature of the mouse model, so an offset of 37 ºC was used. This makes the temperatures at $x = 0$ and $x = h$, 0 ºC and 106 ºC respectively with an average temperature of 53 ºC. such that the equilibrium temperature is described by $T_0 = 106 \cdot x/h$. Separation of variables (5-8) for the one-dimensional problem leads to (5-9). *F(x)* and *G(t)* are the space and time dependent portions of the temperature, *T*, in the one dimensional system. Reagranging the time and space dependent variables and setting these equal to $-k^2$, (5-10), leads to the system of differential equations, (5-11) and (5-12). The basic solution is given in (5-13) and (5-14).

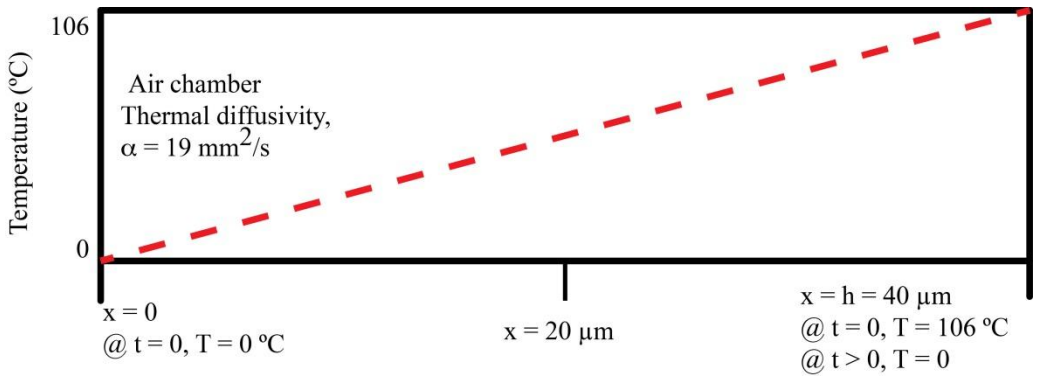

Figure 5-6: Schematic of MATLAB model to simulate thermal dissipation.
The time to dissipate the actuation energy of the pneumatic chamber is simulated

(5-12)

(5-13)

(5-14)

The analysis can be simplified to use the sine solution of (5-12), ignoring the cosine since these solutions would give non zero values for T at $x = 0$ and for the system, $T = 0$ at $x = 0$. Eliminating the cosine term and substituting $k = n\pi/h$ leads to (5-15) and (5-16).

(5-15)

(5-16)

At $t = 0$, $T = T_0 = 106 \cdot x/h$ (allowing for the 37 °C offset). This gives the Fourier series for the sine.

(5-17)

(5-18)

At $t = 0$ the dissipation of the heat over time is calculated from the analytical solution. This analysis shows that the temperature in the central region will be below 40 °C after 8.5 ms.

This analytical solution of a simplified system was compared to the results from a COMSOL model to validate use of the COMSOL model for more complicated systems. A simple COMSOL model was used to ascertain the heat dissipation profile of the plenum and heater into the animal model at 37 ºC. Figure 5-7 shows a comparison of the analytical solution with a COMSOL model, showing the same form (the time to 40 ºC was 7 ms, 18% error) and providing assurance that the FEA modeling of the physical system was configured correctly.

5.4. COMSOL Model for Air, Wax, and Gallium

The chamber-based peristaltic pump was designed to have adjacent diaphragm actuations overlap such that one chamber of any adjacent pair is closed at all times. This prevents pressure external to the pump from inducing flow within the pump. Figure 5-8

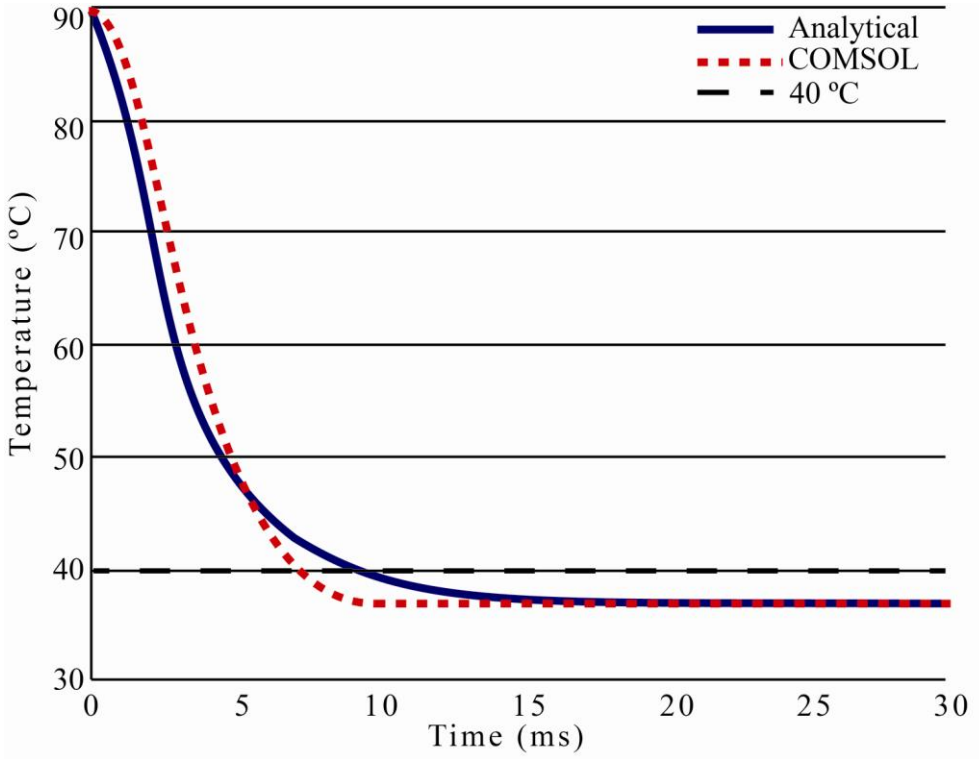

Figure 5-7: Graph of Simple Heat Dissipation Model.
Analytical solution to heat dissipation compared to COMSOL model, validating the use of COMSOL for the heat dissipation modeling in more complex systems.

shows the overlapping heat cycles of a generic thermally actuated four-chamber peristaltic pump. The third model is a simplified version of this, containing two pump chambers, each chamber with a plenum and heater element, the silicon substrate, the TEOS and Parylene C diaphragms, the UV resin, and upper glass layer.

Figure 5-9 is a drawing of one chamber and plenum with false coloring from the COMSOL model. The geometry of the model was parameterized to allow different volumes to account for the plenum volume requirements for the three different materials. See Appendix B for model details including the material properties. The size of the air plenum is determined primarily by the expansion coefficient, C_E of the material and the need to keep the temperature low and at the same time reduce power usage. Air and wax are both capable of expanding by C_E = 10%, but for gallium, C_E = 3%, which calls for a larger volume of gallium by a factor of $3^1/_3$. As mentioned in Section 5.3, the volume of the air plenum was chosen as 120 nL, the volume of wax is also 120 nL, and the gallium volume is 400 nL, for chamber volumes of 12 nL. For wax, both thermal expansion and

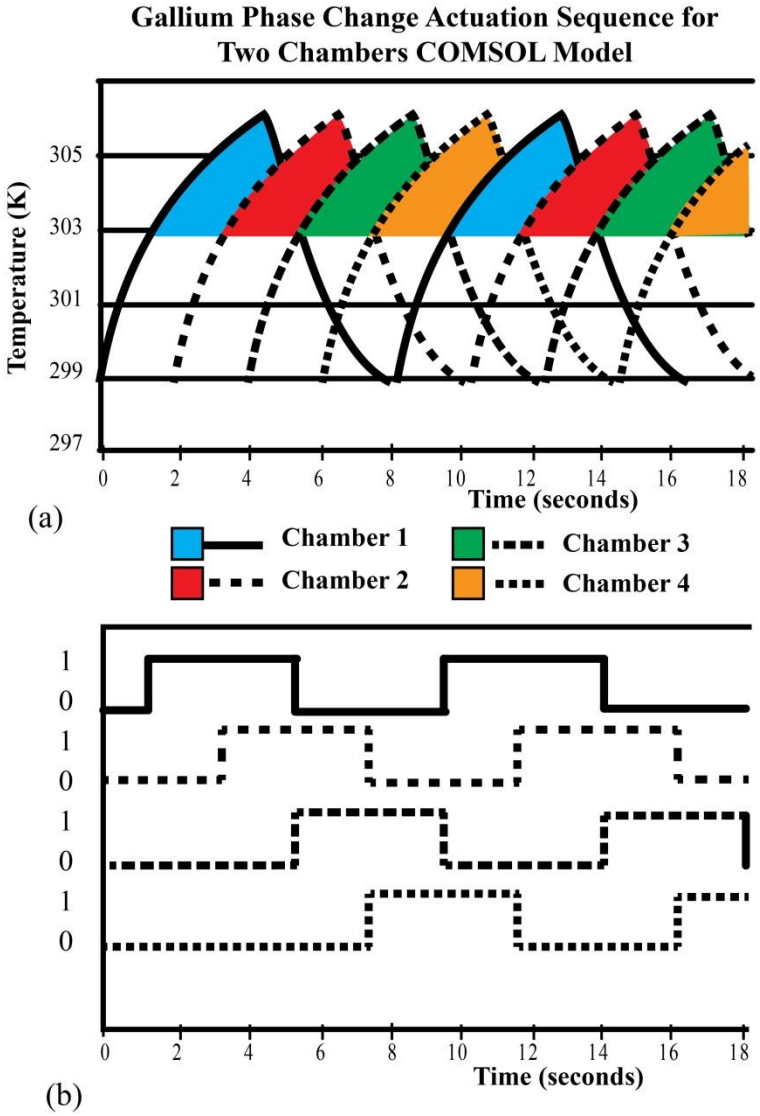

Figure 5-8: Overlapping heat cycles to achieve peristalsis in four-chamber pump.
(a) The colored areas, for this generic device, show the times when the plenums are heated and the chambers are actuated. In the case of air and was, this means the chambers are closed by the diaphragm. In the case of gallium, the chambers are opened with the diaphragms pulled up out of the chamber. Notice that at any time exactly two chambers are activated and two are not. (b) shows the resulting open (0) and closed (1) states. The control signals take a similar form but are shifted towards time = 0.

phase change expansion increases the volume as the temperature rises. For gallium, the expansion occurs during the exothermic phase change.

To compare the three actuation types, two pump chambers of a four-chamber peristaltic pump were simulated. In this manner, simulations of two chambers can be used to find efficiency numbers to compare the devices without the need to simulate all four

chambers. A four-chamber peristaltic pump requires four actuations, one for each chamber, to deliver two boluses of fluid, where each bolus is equal to the stroke volume. For each of the materials, the power for each actuation from the COMSOL model was derived and from this the total power in mJ delivered to the heaters to pump 1 nL of fluid was calculated. This efficiency related to the actuation device not the control circuitry and is used to compare the three actuators.

5.4.1. Thermopneumatic (Air)

The 2D COMSOL model was configured with two air-filled plena (1 mm x 40 µm) and heaters (1 mm x 0.3 µm). Using (5-5) the power to heat an isolated air plenum is 5.43 µJ (c = 1.005 J/Kg, m = 1.35x10^{-7} g, ΔT = 40 K). However, the energy to heat the plena is balanced with the thermal dissipation time and the value derived from the model was 233 mJ (46.6 mW, time = 5 s). Figure 5-9 shows the timing diagram for sequential thermopneumatic actuation of two chambers. The chambers are heated in 5 seconds (t) and can be switched at a rate of 0.1 Hz, which delivers 144 nL/min.

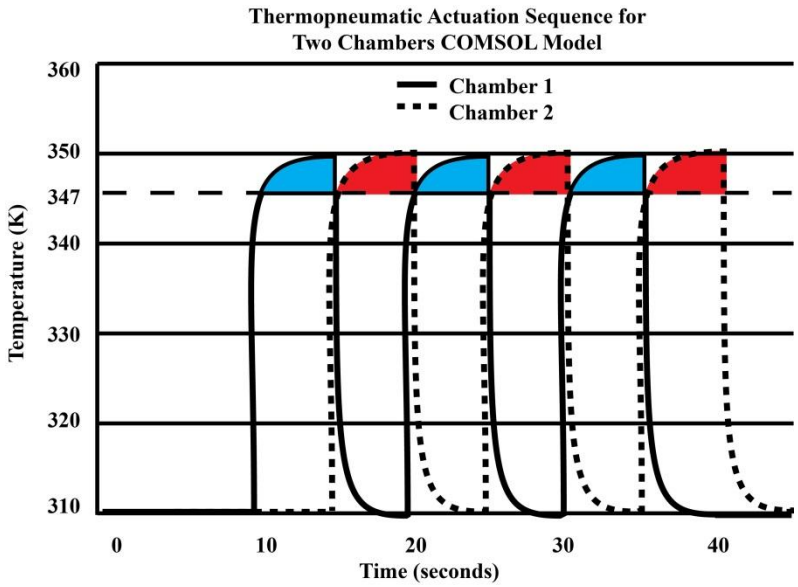

Figure 5-9: Heat calculations from COMSOL simulation.
Graph shows pulsatile heat calculations from a simulation for a air filled plena. The colored areas show times when the chambers are being pushed down (closed). 310K is the murine basal temperature, 347 K (74 °C) is the temperature at which the air has expanded by 10%.

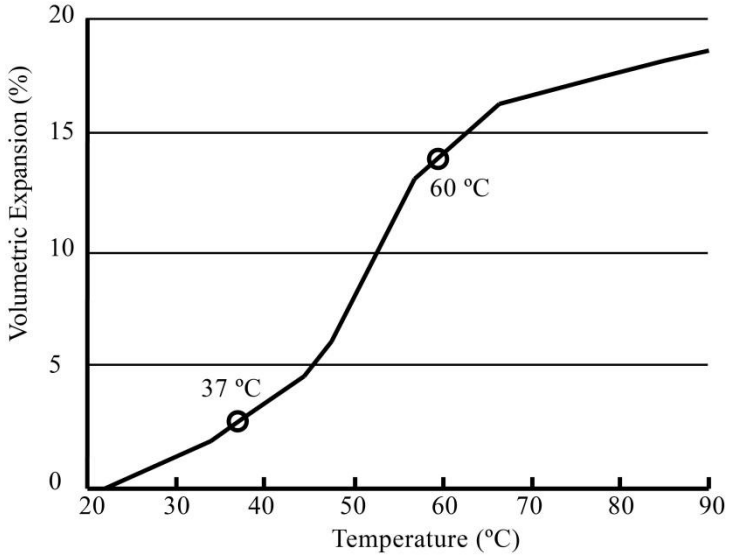

Figure 5-10: Volumetric expansion of wax.
Raising the temperature of the wax from 37 °C, the temperature of the animal model, to 60 °C, ensures the wax will expand by 10% Adapted from (Long & Loveday, 2007)

Equation (5-19), using the values for each of n = 4 actuations, P = 46.6 mW and a delivered volume of V = 24 nL, gives an efficiency of 38.8 mJ/nL.

(5-19)

5.4.2. Phase Change (Wax)

Similar calculations were performed for paraffin. The temperature required to expand the wax by 10% of its implant volume, 60 °C, is taken from Figure 5-10. The temperature of the device starts at 37 °C because it is to be implanted in the animal. For a 12 nL stroke volume the 120-nL plenum would need to expand 10% requiring the wax to be raised from 37 °C to 60 °C. The energy required to heat the wax includes the energy to raise the temperature as described in (5-5) and the heat of fusion, ~ 200 J/g, which is the energy needed for the phase change. The energy to raise the temperature and melt the 120 nL of wax taken from the COMSOL model is 19.2 mW for 1.5 s or 28.8 mJ.

Figure 5-11 shows an example of the timing needed to achieve peristalsis. After the initial heat up of 5 seconds, the chambers can be switched at a rate of 0.1 Hz (t = 1.5 s). This leads to a flow rate of 144 nL/min. The power of actuation, P = 19.2 mW/actuation and using (5-19) gives an efficiency of E = 4.8 mJ/nL.

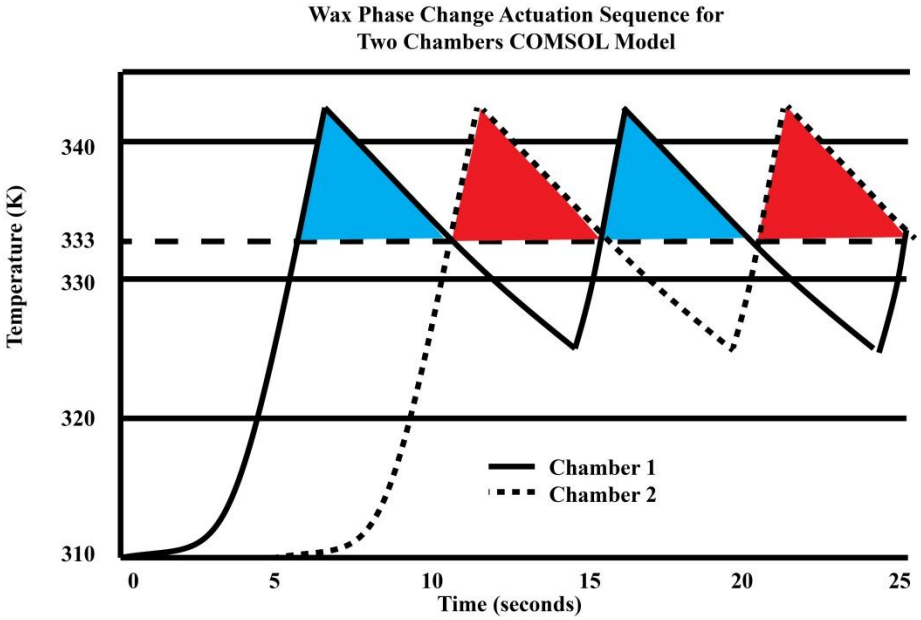

Figure 5-11: Graph of heating/cooling cycles for two wax-filled chambers. The solid colors represent the actuated time of each chamber, when the wax has expanded sufficiently to fill the entire chamber volume and they are closed. The timing of this graph yields an overlapping actuation but staggered actuation is as easily achievable. 310 °C is the murine basal temperature.

5.4.3. Exothermic Phase Change (Gallium)

The density of Ga in the solid phase, ρ_{solid}, is 5.91 g/mL. In the liquid phase, ρ_{liquid} = 6.095 g/mL. Therefore gallium expands by 3% when solidifying so for an increase in volume of 12 nL, 400 nL of molten gallium is required. Section 5.5.3 describes how the gallium was measured.

The melting point of pure Gallium is 303 K (30 ºC) requiring a temperature rise of 10 ºC from room temperature of 293 K. This low melting point is a hindrance for implantation into biological systems with a temperature of 310 K (37 ºC). Instead, a material, such as an alloy of Ga, with a higher melting point would be needed. Many alloys of gallium are known with higher melting points, for example indium (see Figure 5-12). (T. J. Anderson & Ansara, 1991) showed that gallium-indium alloys have been formed with melting points from 288.5 K (15.3 ºC) to 429.75 K (156.6 ºC). Therefore an alloy can be developed that would raise the melting point to between 310 K and 320 K making this actuator feasible for implantation. For example, to achieve a melting point of 313 K (40 ºC) would require ~23 weight percent indium. The melting

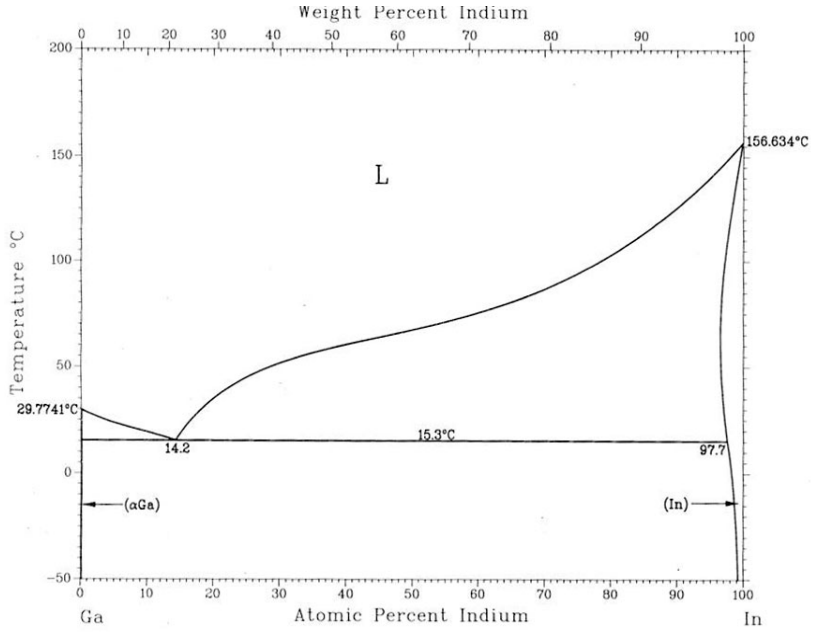

Figure 5-12: Phase diagram of Gallium Indium alloys.
The melting point of gallium can be raised significantly by creating an alloy. An alloy that is 23% (wt) indium and 77% (wt) gallium would have a melting point of 313 K (40 ºC).
(T. J. Anderson & Ansara, 1991)used with permission from Elsevier Limited and Springer

point of indium (429.75 K) is low enough to allow the alloy to be produced on a hot plate.

An actuator using pure gallium was modeled and designed; the analysis will translate to alloys of gallium that require a similar temperature rise to produce the same volume change. The parameters of the COMSOL model can be adapted to the new material to calculate the new power requirements. The COMSOL model was used to determine the lowest power required to maintain a 0.1 Hz actuation cycle. The value was found to be 8.4 mW for 5 s (42 mJ). The Gallium remains actuated as the temperature remains above 303 K. The actuators can be switched at a rate of 0.1 Hz, this leads to a pump rate of 144 nL/min. The power of actuation with (5-19) gives an efficiency of 7.0 mJ/nL (t = 5 s, n = 4, V = 24 nL, P = 8.4 mW). The timing is shown in Figure 5-13 with an actuation period of 10 s. The control circuitry is a binary power control system where one set current is used to heat the gallium. This caused the temperature to overshoot the target temperature by several degrees. A system designed to deliver reduced current once the

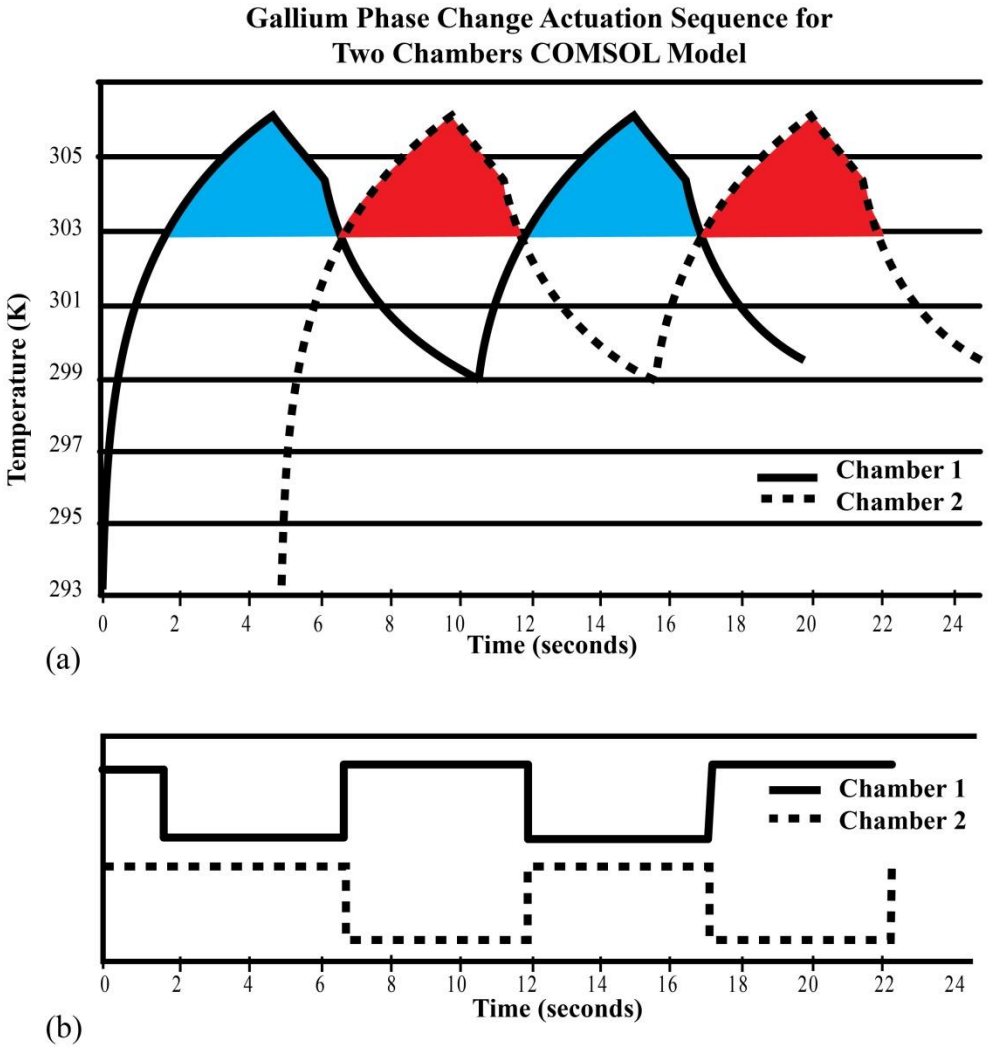

Figure 5-13: Graphs of thermal cycle and heat pulse signals.
(a) Graph of COMSOL derived temperatures in Gallium chamber showing timing of two pump chambers. Note: colored areas above 303 K are times when the chamber is open, unlike the graphs for air and wax (b) Timing of heat pulses to enable the actuation of two alternately actuated chambers. When the heat to a chamber is turned on (signal high) the Ga melts and 'opens' the pump chamber. When the heat is dissipated the chamber 'closes'. 293°C is room temperature

melting temperature is reached could reduce the power consumption of the heaters by more than 30%.

Table 5-4 shows a comparison of the energy required, per pumped volume, of the three materials discussed, air, paraffin, and gallium. For the simulated pump rate, 144 nL/min, gallium and wax are an order of magnitude more efficient than air. The paraffin wax actuator is almost twice as efficient as gallium. However, both air and wax need to have continuously added heat in order to prevent back-flow of fluid from the biological system when not pumping. Gallium expands when it solidifies so the natural state at its unheated

Table 5-4: Calculated Efficiency of Actuation Material by Flow Rate

Material	Frequency	Watts/Actuation	Energy/Actuation*	Efficiency†
Air	0.1 Hz	46.6 mW	233 mJ	38.8 mJ/nL
Paraffin wax	0.1 Hz	19.2 mW	28.8 mJ	4.8 mJ/nL
Gallium	0.1 Hz	8.4 mW	42 mJ	7.0 mJ/nL

Assuming ΔV = 12 nL
* Values derived from COMSOL model.
† Equation (5-19)

temperature will hold the diaphragms in the actuated state and the flow channel will be closed. This zero energy expenditure for the non-pumping state is a key benefit to this new actuator design.

Another difference between the gallium actuator and either the thermopneumatic or wax phase-change actuators is that the stroke of the pump is not determined by the volume of the pump chamber. For gallium, the stroke volume is defined by the volume reduction of the heated gallium. The stroke volume can be more than the volume of the chamber since the diaphragm can be deflected up past the horizontal relaxed state (see Figure 4-2).

The ability of phase change actuators to generate pressure is not related to the input power but to the physical properties of the material. Paraffin wax actuators have been shown to pump against as much as 5 MPa (Boden, et al., 2008); gallium solidification can generate pressure as high as 10 MPa (Inglesfield, 1968). Therefore, the gallium actuator should be able to pump against pressures of up to10 MPa.

5.5. Pachygraphical Fabrication of Actuation Devices

The actuation device and test structures were fabricated by writing pachygraphically (from the Greek for thick writing παχύ·γραφία pachy grafia) with thick films on top of the pump chambers. The presented method uses a direct write system, a Tabletop Series micro dispense pump dispensing system (nScrypt, Orlando, FL, USA).

5.5.1. Materials

Gallium's main advantage over air or wax for the actuation mechanism is the zero-power off state. Therefore the actuation mechanism chosen for this project is a gallium phase-change material pump (PCM). The PCM pump was fabricated with a three-dimensional direct-write dispensing technique. In this manner, the actuator can be fabricated directly on top of the diaphragm device. The direct write process also allows

prototyping and structures with large features (> 100 µm) to be easily fabricated. Fluidic channels and cavities can be formed with sacrificial materials and resins. Materials available for printing also include dielectrics and silver.

5.5.2. Resistors

Resistances between 10 Ω and 100 Ω are easily fabricated with the standard CMOS processes using evaporated aluminum (Al). Higher resistances require either narrower lines, which are more difficult to deposit uniformly and current densities may become problematic, or longer traces, which take up valuable real estate (also requiring larger plenum foot prints.) Resistors were formed on top of the TEOS layer of the chip adjacent to the diaphragm patterns then coated with Parylene C during the diaphragm formation. This electrically insulated the heaters from the gallium, which is highly conductive. The resistance of the heaters was calculated using (5-20).

(5-20)

R is the resistance, ρ is the resistivity of the evaporated Al, L is the length of the trace and A is the cross-sectional area.

5.5.3. Gallium

The amount of Gallium needed to fully actuate the underlying diaphragms of the peristaltic pump is 412 nL. To facilitate the precise measuring of gallium, lengths of long flat ‘ingots’ were formed. A micromolding method was developed using a PDMS stamp-mold to cast the gallium micro-ingots.

To create the positive mold, a 100 mm silicon wafer was cleaned and dried (RCA clean, spin rinse and dry (SRD), dehydration bake 250 ºC hotplate). SU-8 2050 (Micro-Chem Inc., Santa Clara, California) was spun on at 1750 rpm, left to self-planarize for 5 min, and baked at 95 ºC for 10 min on a hot plate before exposure using Karl Suss contact aligner (Energy = 230 mJ/cm^2). Post exposure bake was at 65 ºC on hotplate for 5 min then 95 ºC for 10 min on hot plate. The wafer was left to cool for 15 min before developing in RER 600 (100% PGMEA) developer, for 8 min with constant vigorous agitation. The wafer was rinsed with isopropyl alcohol and spun dry. SU-8, 105 µm thick, was measured optically after coating with gold in a Denton Desk II Sputter coater (Denton Vacuum, LLC, Moorestown, NJ).

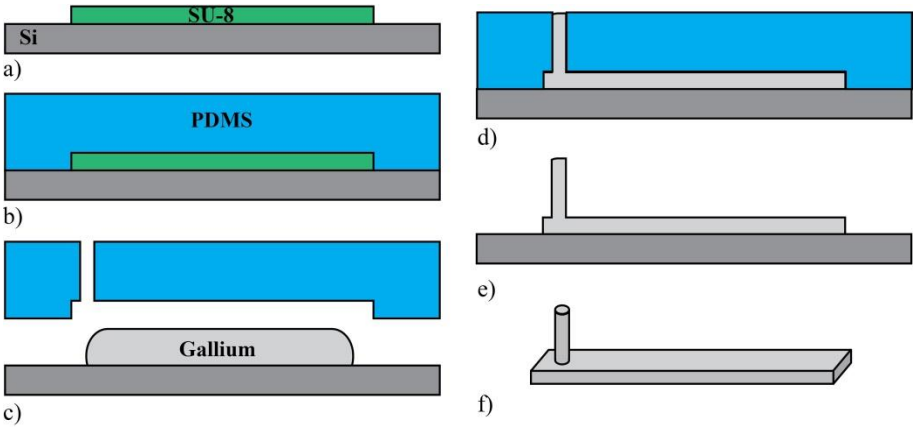

Figure 5-14: Images of micro-contact mold process.
(a) SU-8 patterned lithographically on top of Si substrate. (b) PDMS poured over positive SU-8 mold, cured, then lifted free. (c) PDMS mold pressed against molten gallium on Si substrate prepared with release agent (Micro-90). (d) Gallium was allowed to solidify by cooling with ice pack (e) PDMS mold pulled off leaving gallium on substrate. (f) Free standing gallium ingot ready for measuring and cleaving to provide measured volume of solid gallium

A negative mold was cast from the silicon mold using PDMS as shown in Figure 5-14. PDMS, 25 g, was mixed with cross linker, 2.5 g, and poured into the mold made of the silicon wafer with a retaining wall of aluminum foil. The mold was placed under vacuum for 60 minutes to remove bubbles and baked at 70 ºC for 60 minutes. Once cured, individual stamps were cut out with a razor blade and vents punched with a metal cylinder (see Figure 5-14 (c)). Gallium was placed on a clean silicon wafer and melted on a hot plate, 100 ºC. The stamp was pressed down on top of the molten gallium and held with a small weight. The wafer was placed on an ice pack to speed cooling.

The solidified gallium was easily removed from the pliable PDMS mold. In this way, gallium micro-ingots are formed as shown in Figure 5-15. The micro-printed ingots were

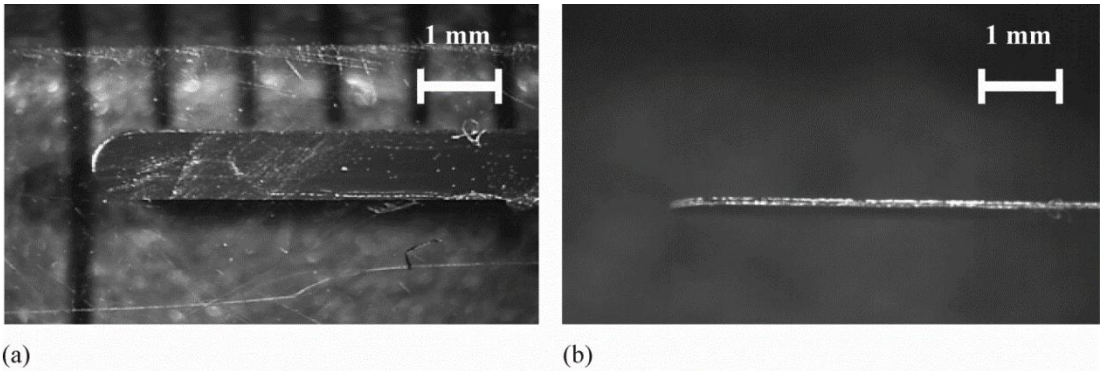

Figure 5-15: Images of micro-contact molded gallium ingots.
(a) Top view of micromold-printed gallium ingot (b) side view of gallium ingot. Low aspect ratio facilitates ease of cutting with razor blade to precise lengths.

measured to be 0.8 mm wide, 90 µm thick, and 20 mm long. This gives the ingots a volume of 72 nL per 1 mm in length. Ingots were cut with a razor blade under a 40x microscope. Measuring 412 nL requires a length of 5.72 mm with an estimated cutting error of ± 7.2 nL.

5.6. Test Structure Fabrication

Figure 5-16 is a cross-sectional drawing of the gallium phase change actuator. The plena and channels were designed for direct-write on top of diaphragms formed *in situ*. UV curable resin gel F-134 (Art Clay World, Jacksonville, TX USA) was printed in a 100-µm thick layer. Plena 1.5 mm wide by 2.75 mm long allowed for 400 nL of gallium. The plenum volume is 400 nL, the chamber volume is 12 nL bringing the solid gallium volume to 412 nL. The pump chambers were fabricated on silicon wafers with more traditional MEMS techniques as described in Chapter 4. Test structures were formed using the nScrypt direct write tool to verify the actuation of the underlying diaphragms by the expansion of gallium. 10.5-Ω heaters (σ = 0.43, N = 16) were defined lithographically on top of the TEOS structure (0.3 µm Al deposited by evaporation.)

The resistors were covered with Parylene C (4 µm thick) during the diaphragm formation process in the room temperature deposition tool described in Section 2.1.1. Plena were formed with UV curable resin with the nScrypt. A tool path was defined in a text file to describe a path along the surface of the device and regulate the flow of the resin out of the narrow tip (75 µm ID) by controlling the dispensing pressure to a resin-filled syringe (20.1 psi) and by controlling the writing speed

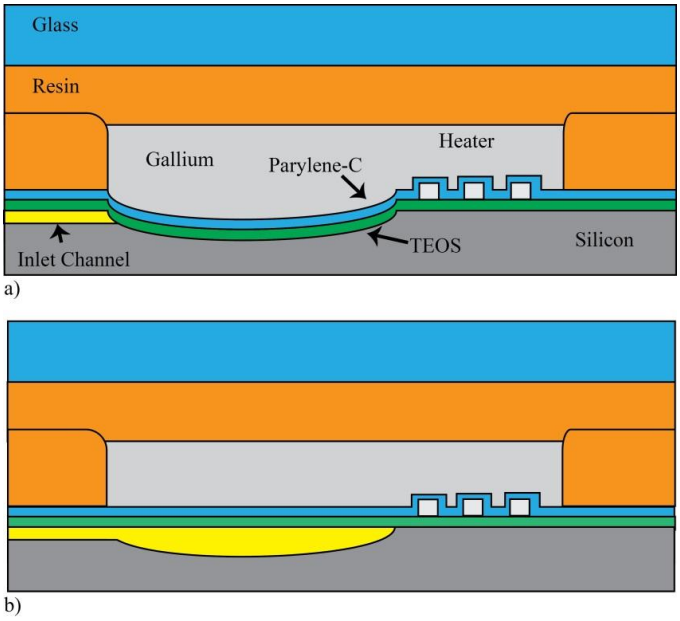

Figure 5-16: Cross-sectional diagram of Gallium actuator over diaphragm chamber.
(a) actuator in 'off' state with cooled and solidified gallium filling the chamber volume.
(b) smaller volume of heated gallium allowing fluid to be sucked into the chamber from inlet channel to the left of the chamber

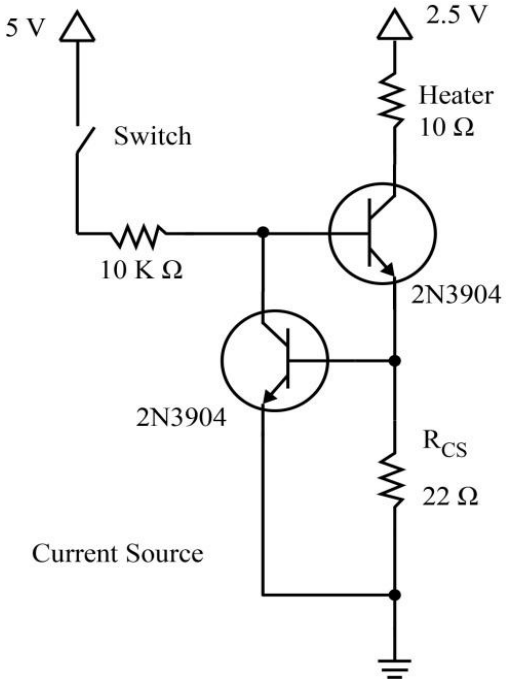

Figure 5-17: Current source circuit. Manual switch operated current source supplies 32 mA to heater ($I = R_{CS}/0.7$).

(5 mm/s). The resin was cured under a Blak-Ray B-100 UV lamp (UVP, LLC, Upland, CA) with 365-nm long wave UV for 10 minutes. Gallium ingots, 5.72 mm long, were placed manually in each of the four plena. The device was warmed on a hotplate at 50 ºC, to melt the gallium, and placed in a fixture that supplied compressed air (20 psi) above the plenum, forcing molten gallium downward, pressing the diaphragm into their actuated positions where it was allowed to cool, solidifying the gallium.

The device was removed from the fixture and covered manually with a layer of UV curable resin. The heaters were connected to a current source circuit (see Figure 5-17), via silver conducting ink, 40-3920 (SRA, INC, Foxboro, MA). Raising the temperature of the gallium through the resistive heaters caused the diaphragm to relax pulling liquid into the chamber. Cooling allowed it to expand back into the chamber expelling the liquid from the device.

5.7. Conclusion

A gallium based exothermic phase change actuator was developed for integration with a microfluidic diaphragm pump device via pachygraphical fabrication. The exothermic phase change actuation provided by the gallium allows the actuator to hold the pump diaphragm in the closed position blocking flow with zero energy expenditure. This is a significant improvement over the conventional normally open actuator/pump chamber devices previously presented. Another benefit of the gallium actuator is the increase in supplied pressure. According to (Inglesfield, 1968) the pressure available from the solidification of gallium can exceed 10 MPa.

Results of actuation testing, including chamber pump volumes and actuation power, are reported in Chapter 6. A single actuator / pump chamber was assembled and heated

resistively showing that the expansion pressure of the solidifying Ga is transferred to the pump fluid via the chamber diaphragm.

Chapter 6 Micropump System Component Integration

Science is the century-old endeavor to bring together by means of systematic thought the perceptible phenomena of this world into as thorough-going an association as possible.
Albert Einstein

In the previous chapters, the necessary integration technologies have been developed, low-volume in-plane fluidic interconnects, micro-molded cannulae stops, *in situ* pump diaphragm formation, flow-control, and a low-power actuation mechanism. The next step was to integrate all of the techniques for forming channels, chamber, interconnects, and actuation into a four-chamber peristaltic micropump. Putting these together to form a micropump suitable for murine implantation is the subject of this chapter. This implantable, variable flow micropump platform has been developed, specifically for intracochlear drug delivery in the mouse model for deafness therapy research. Figure 6-1 is a conceptual drawing of one configuration of an implantable system incorporating

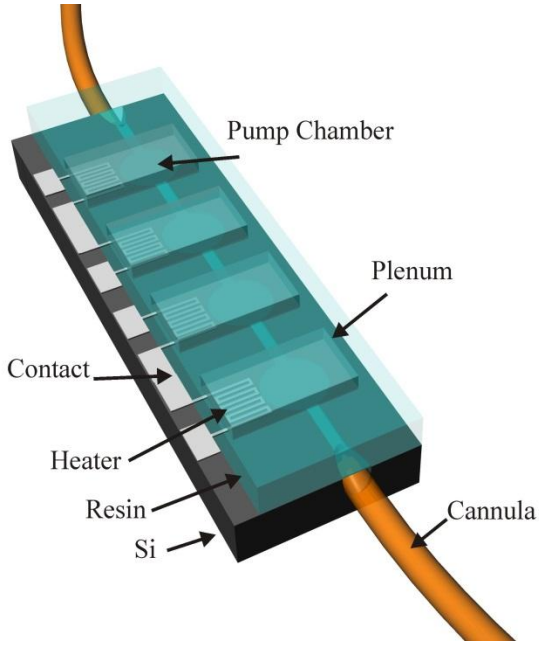

Figure 6-1: Drawing of a four-chamber peristaltic pump concept.
This form factor is 10 mm x 4 mm x 1 mm (40 mm^3) Pump with phase change actuation mechanism and coupled to small diameter capillary tubing.

these technologies. The volume of the pump (40 mm^3) is much smaller than the volume of the smallest osmotic pump available from Alzet, 0.5 cm^3 (500 mm^3). These technologies have been integrated into an implantable micropump platform.

6.1. Fabrication

Figure 6-2 shows a cross-sectional drawing of the pump fabrication process. Chapter 4 presented a fabrication process for creation of deformable diaphragms over pump chambers with simultaneous coating of the microfluidic channels allowing for the integration of a biocompatible fluid flow path. The integration of the in-plane interconnects was also described in Chapter 4. Pump fabrication begins with the process developed in that chapter. Wafers were cleaned (RCA) and a film of TEOS SiO_2, 0.5 µm, was deposited with a plasma-enhanced vapor deposition (PVD) (P5000, 290 W, 68 s). The TEOS was patterned, via an O_2 plasma etch (Drytek Quad, Ar: 35 sccm, CHF_3: 65 sccm, O_2: 5 sccm, 200 W, 70 mtorr), with 1-µm openings to define the pump features, fluid channels, interconnects, and diaphragms. The 1-µm openings require only a 3-µm thick deposition of Parylene C to fill and strengthen the diaphragm where a 4.5-µm thick film was required for the larger 4-µm openings used in the actuation test structure fabricated in Chapter 4. A 0.3-µm film of aluminum was evaporated onto the surface in a CHA flash evaporator system. A contact mask, printed on a transparency was aligned manually, under a microscope, to the patterned TEOS. Exposure (22 s) was performed on a Karl Suss MA-150 contact aligner (Karl Suss America, Waterbury, Vermont). Heaters and contacts were patterned in the aluminum with wet etching in Aluminum Etch 16-1-1-2 (Fujifilm Corporation, Tokyo, Japan) and a protective coating of photoresist. The TEOS SiO_2 film thickness used in the deflection and long term robustness test was 1.0 µm. The thickness was reduced to 0.5 µm for the integrated pump assembly as part of process improvement. Thinning the diaphragm enables actuation by a wider variety of dynamic mechanisms requiring a reduced actuation pressure. This also will allow for future design iterations to incorporate smaller diameter chambers without increased actuation pressure requirements.

The integration of the deeply etched interconnects with the shallowly etched channels necessitates a two-step process as described in Section 4.3 (see Figure 6-2 (a) to (c)). To

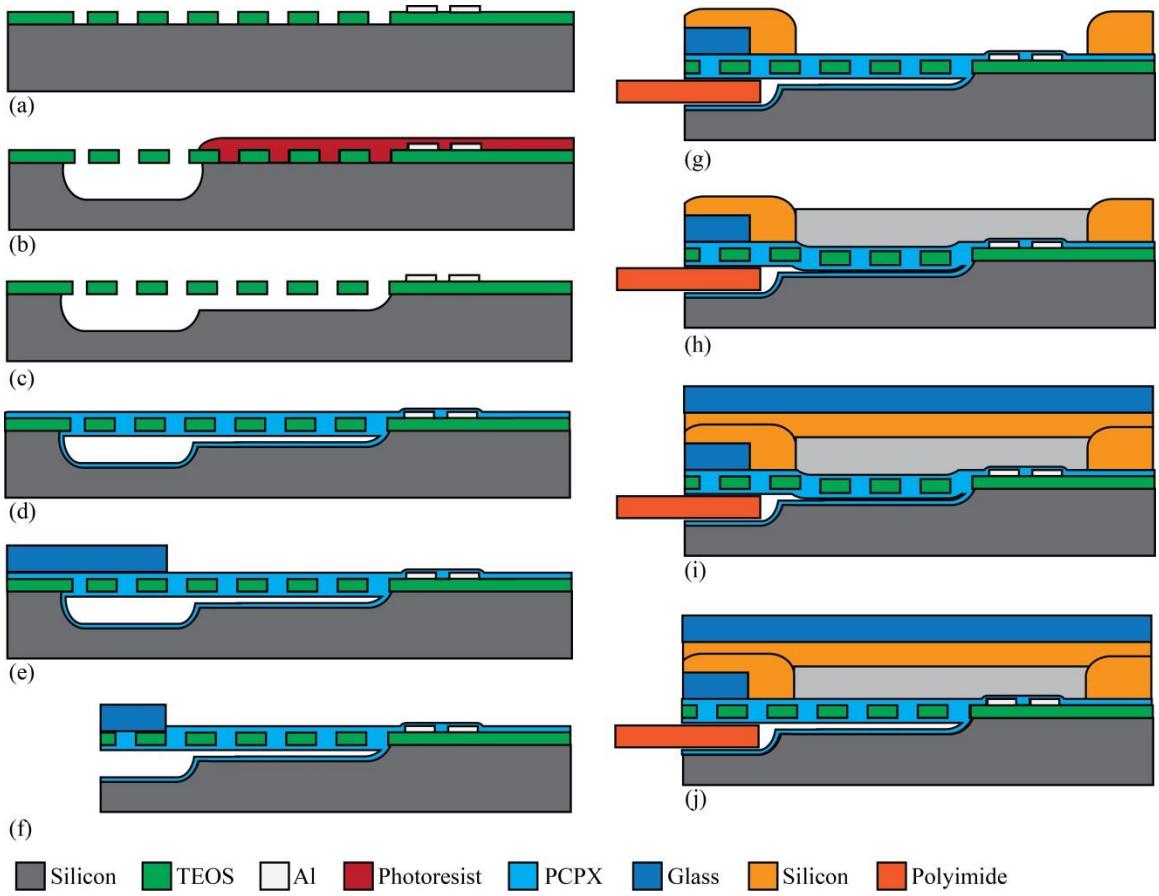

Figure 6-2: Micropump fabrication process. (Not drawn to scale)
(a) 1 µm TEOS deposited with P5000, patterned to define channels and chambers, 0.3 µm Aluminum evaporated and wet etched to define heaters and contact pads
(b) Photoresist (PR), 1.2 µm, spun on and patterned to protect chamber areas, XeF_2 etch, 130 µm, for interconnects
(c) PR removed in O_2 plasma, second XeF_2 etch to create channels and chambers
(d) Parylene C, 3 µm, deposited to form diaphragms, cover channels, and coat flow path
(e) Cover glass (18 mm x 18 mm x 0.17 mm) secured with cyanoacrylate covers interconnect area
(f) Wafer diced with K&S wafer saw to reveal interconnect openings
(g) UV curable resin written with nScrypt tool to create actuation plena, capillary tubing (140 µm OD) inserted and captured with Parylene C deposition, 40 µm, (plenum protected with polyimide tape during deposition, not shown)
(h) Capillaries connected to vacuum with nanotight fittings to drawn down the diaphragms, gallium ingots (412 nL) placed in the four plena, melted, and re-solidified to hold the diaphragms before removing vacuum
(i) A Cover glass was manually coated with UV curable resin and lowered onto gallium filled plena to prevent bubble formation.
(j) When heated the gallium withdraws from the pump chamber pulling in fluid

make this possible, an additional masking material is required to protect the shallow channels from the deep etch process. Therefore, the second mask must withstand the long etch time of the interconnects. In addition, as the mask must be removed after the

interconnect areas of the TEOS are 'released' only a dry removal method will work. XeF_2 will etch Si isotropically and both TEOS and photoresist are good masking materials. The channel areas of the device can be protected by a pattern of photoresist, which then can be removed in an O_2 plasma. The underlying silicon is etched in XeF_2, with this two-step process to achieve different depths for the flow path, deep interconnects (140 µm) and shallow channels (15 µm). The diaphragms are formed with a 3-µm deposition of Parylene C. A deposition tool, constructed at RIT, was used to deposit Parylene C at room temperature. The 3-µm thick film is sufficient to fill the 1-µm wide openings in the TEOS and form continuous diaphragms. The thickness of the PCPX deposition is controlled by the amount of dimer placed in the evaporator at the start of the process. One gram of dimer deposits approximately 0.8 µm of polymer.

An exothermic phase change actuator was developed in Chapter 5. Four such actuators were used in this pump to motivate the fluid peristaltically by transferring the momentum to the underlying TEOS/Parylene C diaphragms. Resistors were formed on top of the TEOS adjacent to the diaphragm patterns then coated with Parylene C during the diaphragm formation described above, the resistance is calculated using (5-20) with L = 21 mm, A = 60 µm^2 (200 µm by 0.3 µm), and ρ = 2.86 µΩ·cm (pure aluminum) gives a value of R = 10 Ω. Figure 6-3 shows the layers used to fabricate the actuator starting with the silicon chip carrying the chambers, channels, interconnect channels, and heaters, which were formed as described in Chapter 4 (see Figure 6-2 (a) to Figure 6-2 (d)).

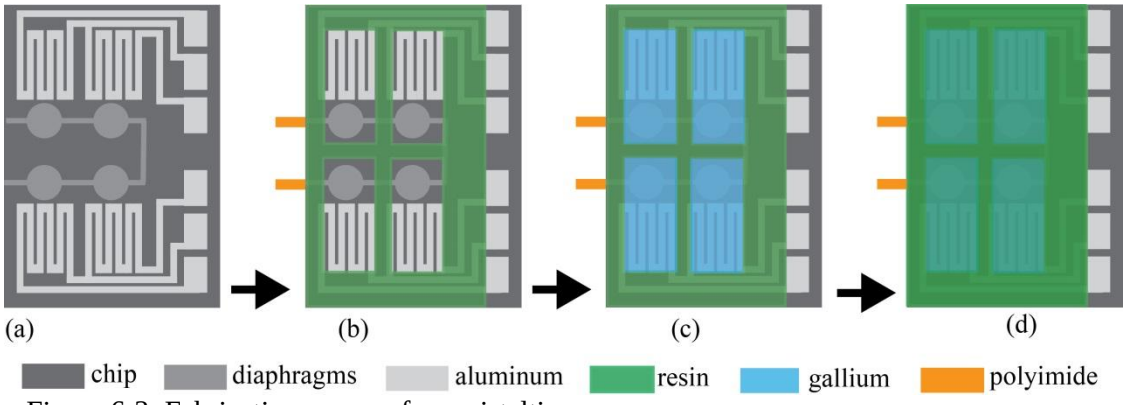

Figure 6-3: Fabrication process for peristaltic pump.
(a) Underlying pump chambers, channels, heater elements, and contact pads formed with CMOS compatible processes. (b) Direct write resin forms the actuation plena and capillary tubing (140 OD) is inserted and captured with Parylene C (c) Gallium deposited into plena as diaphragms being held down by vacuum applied to the capillary tubing (d) Additional layer of resin and glass seal the plena

An 18 mm by 18 mm by 0.17 mm cover glass was adhered to the chip along the interconnect edge to prevent resin from flowing into the microchannels during the direct write step and to provide a clean opening for the insertion of the capillary tubing. The wafer was diced with a K&S 780 wafer saw (Kulicke & Soffa Pte Ltd, Singapore) to expose the microchannel interface. Using a direct write system (nScrypt, Orlando, FL, USA) the actuators were printed directly on top of the diaphragm device. UV curable resin was printed pachygraphically with the nScrypt to define the gallium wells. The resin is dispensed from a pneumatically controlled syringe (20.1 psi) through a 75 µm ID tip to control the width and height of lines defined in a tool path text file. The device is held onto the tool's platen with vacuum and moved along the path at 5 mm/s. The resin gel, F-134 (Art Clay World, Jacksonville, TX USA), was cured under a 365 nm UV light for 10 min. Small diameter capillary tubing (140-µm OD) was inserted into the interface openings and sealed with a thick (40 µm) deposition of Parylene C. Polyimide tape was applied to the tops of the plena and the resistor contact pads to keep these free of Parylene C.

Figure 6-4 shows the device with the underlying microfluidics, heaters, printed plena, and the captured capillary tubing in place. The capillary tubing was connected with Nanotight fittings (Upchurch, Scientific, Oak Harbor, WA, USA) to vacuum of less than 240 torr (providing a trans-diaphragm pressure of > 10 psi).

Gallium micro ingots were placed in the plena and melted on a hot plate at 100 °C, such that they would conform to the shape of the actuated diaphragms while the pumps were under vacuum of greater than 10 psi. This held the diaphragms in the down, closed position in order to

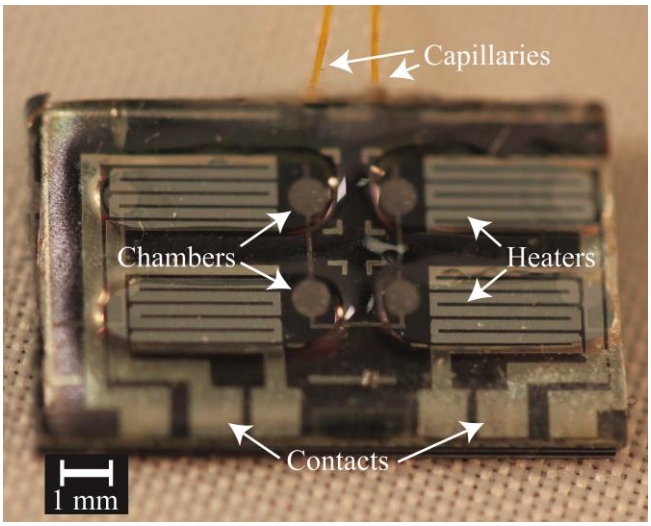

Figure 6-4: Photograph of pump with plena and capillary tubing.
Visible are the interconnected capillary tubes, the heaters, the diaphragm chambers, the plena and the heater contact pads. The heaters were designed to be fabricated with a mask printed on a transparency. Utilizing standard lithographic mask will allow for resistor geometries in line with design parameters.

deposit the gallium so that the diaphragms are actuated by the solidified metal. Gallium ingot formation was completed with the micro printing technique described in Section 5.5.3. As the metal cooled it expanded keeping the diaphragms pushed down when the vacuum was released. A glass cover slip (18-mm by 18-mm by 0.17-mm) was covered with UV curable resin, pushed onto the device to cover the actuation plena, sealing in the gallium in the actuation chambers and cured for 10 minutes under a 365 nm wavelength UV light.

6.2. Integration

Section 2.1.3 discussed the design of the interconnect tapers using a SF_6-O_2 plasma etch. SF_6-O_2 leaves a very smooth and even surface; the XeF_2 can leave a pitted surface that may impede the complete insertion of the tubing into the tapered channels or the complete filling of the tapers with Parylene C. The additional surface roughness caused no issues with tubing insertion or gap filling for this process. If, on the other hand, the roughness had posed a problem as it might for deeper interconnects for larger capillary tubing, its effect could have been ameliorated by following the XeF_2 etch with a short SF_6-O_2 etch to round the pit edges. (Sugano & Tabata, 2002) reduced the surface roughness and aperture affects by heating the substrate. This could be accomplished in the Xactix Si etcher by placing the wafer on a preheated plate in the tool. Another solution would be to use only an SF_6-O_2 etch for the interconnects but this method requires an additional mask layer, which could introduce an additional source of alignment error.

The pump chambers of the fabricated system were arranged in a two by two configuration instead of inline putting both interconnects on one side to the device so that only one precision cut was needed to establish the interconnect interface. In order to expedite fabrication, a contact mask was prepared on a transparency necessitating the widening of the resistors (200 μm) in order to avoid opens caused by the poor optical quality of the mask film. A wide trace with a serpentine shape was therefore utilized to create the desired resistance and although this did increase the size of the device (7 mm x 13 mm x 1 mm). Using a standard lithographic mask will allow for a smaller device (7 mm x 7 mm x 1 mm).

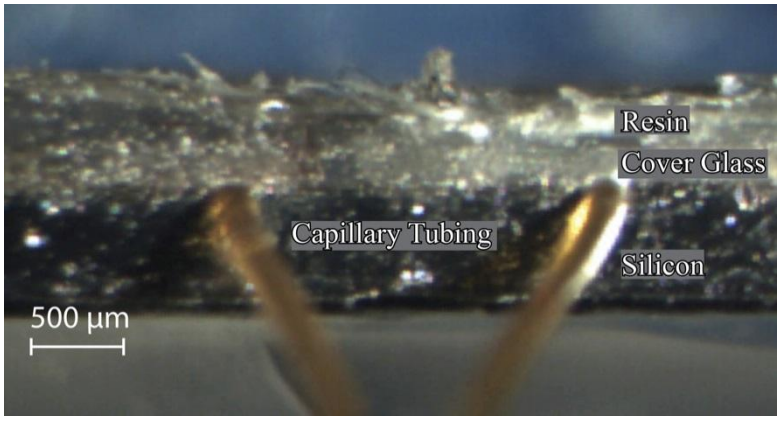

Figure 6-5: Image of interconnect interface using cover glass. Cover glass was adhered to the surface of the silicon to form the interconnect channels for the micro capillary tubing (140-µm OD). The entire device is coated with a thick film (>20 µm) Parylene C. The rough edge along the top of the resin is where a protective layer of tape has been removed to reveal the uncoated plena.

The robust interconnect technology presented in Chapter 2 was developed using anodically bonded glass, which allows both a clean precise cut at the outboard edge of the chip and visual inspection of the tubing during insertion, both of which ease the task of tube insertion. A top layer of glass is not an option as anodic bonding is not possible with Parylene C coating the bottom substrate. However, as an alternative to the bonded glass of chapter 2, micro cover glass (18 mm x 18 mm x 0.17 mm) was secured with cyanoacrylate to the chip over the out board edge of the diaphragm chips covering the interconnect channels, but not the shallow channels or chambers, prior to the direct write application of the UV curable resin. The chip/glass/resin sandwich was diced with a wafer saw creating the same clean precise openings for the insertion of the capillary tubing as had the bonded glass (see Figure 6-5) where the two interconnects are shown on the same side of the device.

6.3. Testing

The individual subcomponents, cannulae insertion stops, in-plane interconnects, and diaphragms have already been characterized and evaluated in previous chapters. Therefore the focus of this section is on testing the actuator and the pump as a whole. The resistors were measured with a multimeter, Agilent 34401A, (Agilent, Santa Clara, CA) and have an average value of 10.7 Ω (σ = 1.1, n = 4). To actuate the chambers

peristaltically, a control circuit was designed using 555 timers, flip-flops, and logic circuits to regulate the power applied to the actuation heaters (see Figure 6-6). The power was supplied with four current sources each using two NPN transistors (2N3904). The resistor R_{CS} is a current sense resistor where the current (A) to the heaters is kept to $0.7/R_{CS}$. Selecting R_{CS} = 22 Ω gives a current of 32 mA that supplies 10.96 mW of power to the10.7-Ω resistors, which is greater than the power derived from the COMSOL model. Lower average power values may be supplied to the heaters by controlling the duty cycle of the signal to the current sources.

The current sources are turned on by a signal generated by the timers and flip flops. One timer controls the frequency of the actuation sequence and the other has the ability to

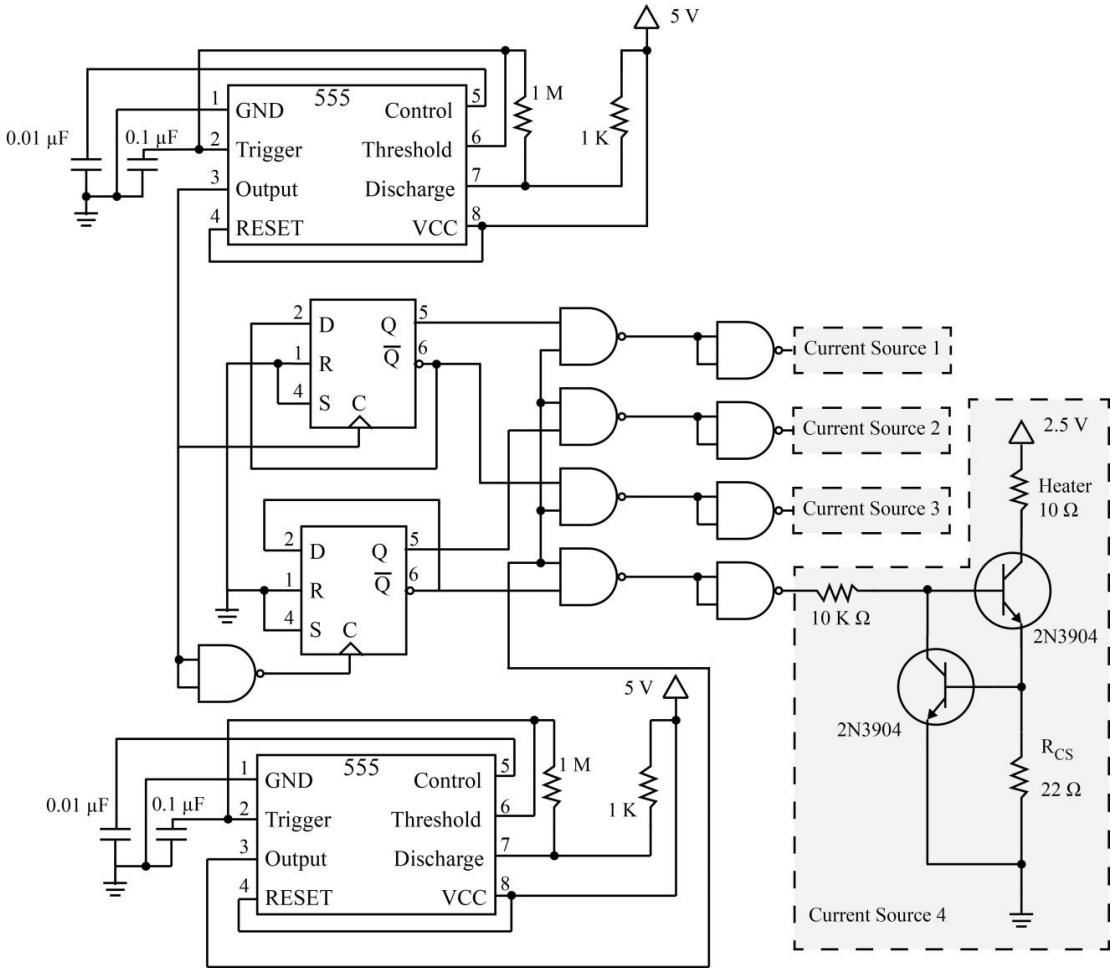

Figure 6-6: Schematic drawing of peristaltic heater control circuit.
555-timers generate the pump clock and the heater energizing pulses. The above design uses a 555-timer to modulate the current source signal thus controlling the energy supplied to the heaters. The current source circuits in the final project used 2N3904 transistors, and R_{CS} = 22 Ω

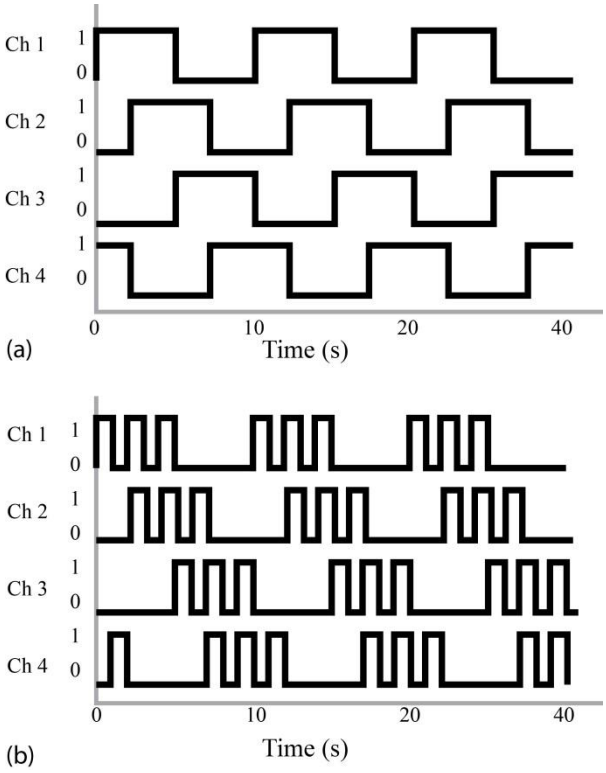

Figure 6-7: Heater current control signals.
(a) Heater current control signal sequence to control peristalsis with maximum current.
(b) Modulated heater control sequence to deliver less energy per activation cycle than full-power signal.

switch the control signal on and off within the envelope of the actuation sequence (see Figure 6-7). In order to deliver 8.4 mW to the 10.7-Ω heater resistors (28 mA) the current can be modulated with a duty cycle of 0.77. The control circuit was designed to drive the device with a known current for the purpose of demonstrating the pump. This is not intended to represent an optimal solution for maximum efficiency. Therefore, the drive circuit is not included in efficiency calculations.

Current was applied to all of the actuator elements simultaneously to open the fluidic path allowing flow through the entire device. A syringe was used to pull fluid through the device and capillary tubing. The setup in Figure 6-8 was used to measure directional flow. The fluid pumped out of the device flows through a capillary tube laying on top of a ruled surface. The syringe was disconnected from the capillary tubing and the fluid front monitored. While the gallium was still being heated, no flow was detected indicating no flow. Once the device cooled and the gallium actuators closed the diaphragm chambers, the fluid front was observed to be static indicating that no fluid flowed through the pump in the off state. Chamber volumes and the flow rate of the pump were measured by taking time-lapse photographs of the fluid moving through the capillary tube as in (O'Brien 2009). The inner diameter of the tubing is 112 μm and each 1 mm of tubing holds 9.86 nL of fluid. Figure 6-9 shows a series of captured images of the fluid/air interface, the fluid front, as it moves from right to left between mm markings.

The first test was to determine the volume of fluid pushed by each of the four chambers by actuating and de-actuating and measuring the distance the fluid front moved along the

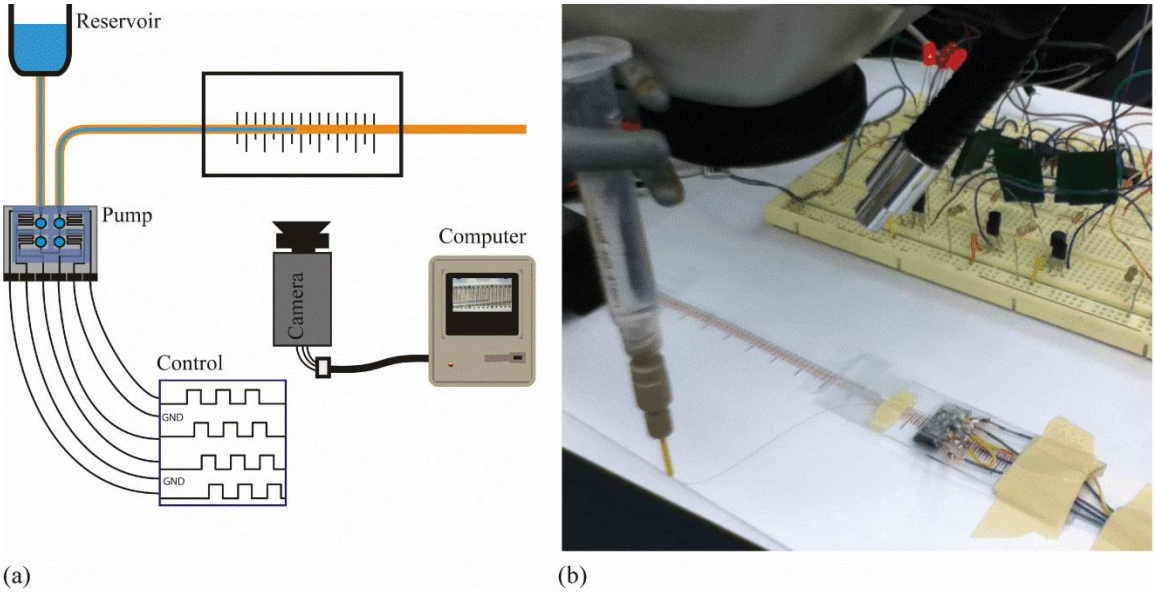

Figure 6-8: Experimental setup for gallium thermal actuation peristaltic pump.
A camera is set up to record the movement of fluid through a capillary tube. Fluid is pumped from a reservoir to the outlet capillary tubing. A computer captures the images for later analysis. Reservoir (syringe body) supplied fluid to inlet. Control circuit supplies current to actuation heaters to move fluid peristaltically through outlet capillary along ruled markings. Camera on microscope captures time-lapse images for flow rate analysis.

capillary tubing. The outboard chambers could be opened and closed independently but the inner two chambers needed the nearest outboard chamber to be opened during the inner chambers actuation. To measure the outboard chambers, those adjacent to the interconnects, required heating the associated plena (5 s) and measuring the fluid pushed through the capillary tube as the gallium cooled and re-solidified. Measuring the two inner chambers required a two-step actuation sequence. First, both an outboard and adjacent inner plenum were heated (5 s). The inner heater was then turned off and the fluid moved by the gallium cooling was measured

As discussed in Section 5.4.3 the pumped volume of a chamber is controlled by the

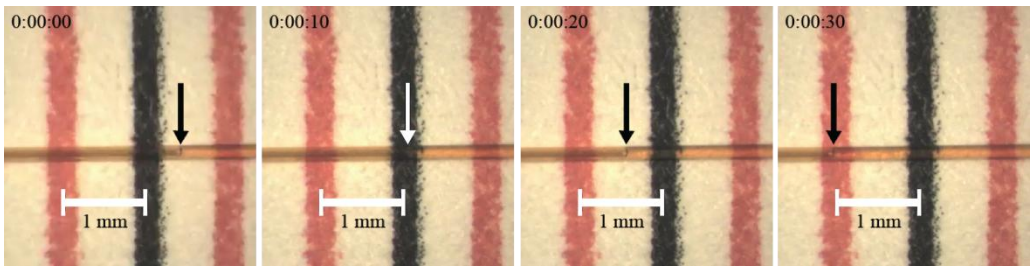

Figure 6-9: Time-lapse photographs of the fluid front passing over a ruler.
Actuation frequency 0.025 Hz. Images were captured from which the flow rate data was extracted. For the capillary tubing used (112 µm ID) each 1-mm mark represents 9.86 nL of fluid. The above sequence shows 1.5 mm (14.79 nL) over 30 seconds, for a rate of 29.58 nL/min.

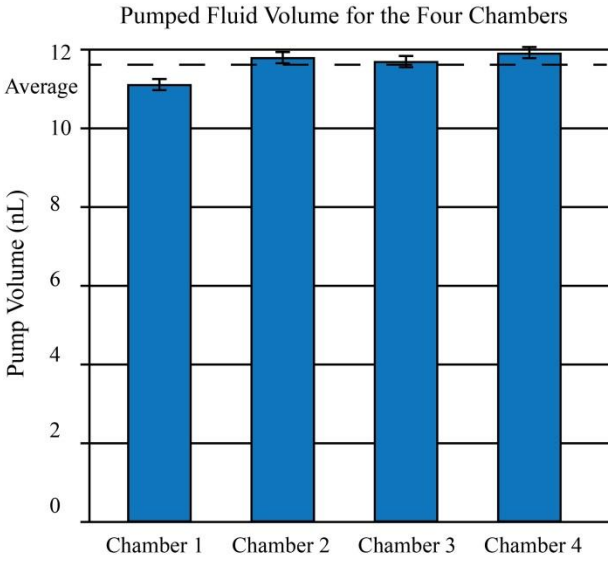

Figure 6-10: Pumped fluid volume for the four chambers of the pump.
Designed value = 12 nL, average value = 11.1 nL (shown as dashed line) (n = 4, σ = 0.35)

change in volume of the gallium and may be different than the volume of the chamber itself. The volume of the 800 µm diameter chambers with a depth of 15 µm is 7.5 nL, but with 412 nL of gallium, the change in volume and thus the pumped volume should be 12 nL. The data shown in Figure 6-10 shows that the average pumped volume is 11.1 nL so every pump actuation results in nearly 1 nL less fluid pumped than expected.

As the pumped fluid is controlled directly by the contraction of the gallium the majority of the error is likely attributable to the volume of gallium. The cutting error of the gallium was estimated to be ± 7.2 nL, this would lead to a pumped volume error of ± 0.01 nL. Molding errors could have resulted from voids and irregularities in the molding process, every 10 nL void would give a reduction of ΔV of 0.31 nL. There is also possible fluid flow measurement error and fluidic capacitance of the system.

As discussed in Section 5.4.3, the chambers can be actuated at 0.083 Hz (period T = 12 seconds, 0.5 duty cycle). The peristaltic pump was design to deliver two ‘pump chamber’ volumes of fluid (24 nL) every period (12 s) or 120 nL/min. From the pump chamber volume measured above (11.1 nL), the pump rate drops to 103.8 nL/min for 0.083 Hz. It was found that pumping was achieved with an activation power of 10.1 mW delivered at 0.083 Hz. The 10.1 mW was accomplished with a 0.92 duty cycle. Each pump cycle takes 4 actuations of 6 seconds at 10.1 mW to deliver 22.2 nL. This translates to an efficiency of 11 mJ/nL. The efficiency calculation considers the power delivered to the actuation heaters and not the losses in the control circuitry. Flow rates were measured as above for actuation frequencies from 0.02 Hz to 0.083 Hz (T = 50 s to 12 s) with the same power.

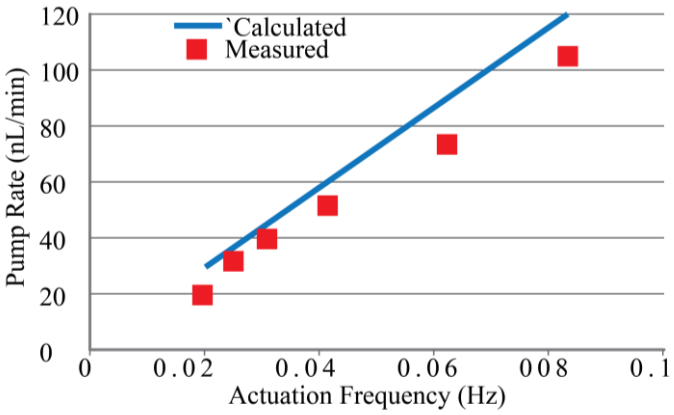

Figure 6-11: Graph of pump rate by actuation frequency compared to calculated values.
Ideal values calculated based on pump chamber volume and actuation frequency. Pump rates above 100 nL/min should be possible if the control circuit was designed to modulate the power once the actuator was melted in order to reduce the heat introduced to the system.

Figure 6-11 is a graph of the results; pump rates below 16 nL/min are possible if the control circuit was designed such that the power is modulated once the gallium has liquefied in order to reduce the heat introduced to the system. Lower rates are also possible by pausing the pump with all chambers closed. Pump rates greater than 100 nL/min are also be possible with an increase in actuation current to shorten the actuation time.

6.4. Conclusion

The implantable planar micropump developed is biocompatible, low-volume, low-power, controllable, with low fabrication complexity, and will work with fluids commonly used for murine intracochlear infusions. A pump with dimensions 7 mm x 13 mm x 1 mm, which is less than 100 mm^3, was fabricated and pumped between 18 µL/min and 104 µL/min. Fluid pumping at 0.083 Hz actuation required 10.1 mW/actuation (60.6 mJ) where the COMSOL model predicted that 8.4 mW/actuation (50.5 mJ) would be required (20% error). Potential sources of this error include differences in the model geometry and the actual fabricated geometry, errors from the application of a 2D analysis of a 3D system, and discrepancies in the values used for material properties. One of the key benefits of the gallium phase change actuation is the zero-power off state. This allows the pump to prevent flow to and from the biological system without consuming energy.

The pump dimensions can be reduced to less than 120 mm^3 by reducing the heater area as discussed in Section 6.1. Pump rates both above and below those tested are achievable with modifications to the control circuitry, or by changing the size of the chambers. This

micropump will enable chronic, calibrated delivery of therapeutic agents that is not possible with existing pump technologies. Key integration technologies have been developed to address these unique requirements: low-volume in-plane fluidic interconnects and micro-molded cannulae stops, other necessary technologies have been designed: *in situ* pump diaphragm formation over Parylene C coated fluidic micro chambers and channels, and integration of a low-power actuation mechanism with a zero-power off state.

6.5. Future Work

Long-term robustness testing and diaphragm deflection testing were performed pneumatically. Performing these tests with the gallium actuator would be beneficial and should include the thinner TEOS and Parylene C layers used in the integrated micropump.

The large diaphragm diameter of the integrated pump was designed to accommodate either phase change actuation or thermopneumatic actuation. As the pressure from the gallium phase change is much greater than that available from thermopneumatic, smaller diaphragms, which require larger actuation forces could be used with no additional energy expenditure. The device as designed can pump above the target maximum of 100 nL/min therefore pumps designed with smaller chambers to be operated at higher frequencies could significantly reduce the power requirements. This improvement in power comes from the reduction of the energy needed to liquefy the smaller amounts of gallium required to actuate lower volume chambers. The time to actuation can thus be reduced giving less time for heat to dissipate into the surrounding materials improving efficiency. COMSOL simulations analyzing the trade offs between large chambers actuated at low frequencies and smaller chambers actuated at higher frequencies would be advantageous. Additionally, more complex control of the heat-signal circuit can be designed with incorporation of thermistors to signal when the plena reach the desired temperature. These more advanced control circuits should be designed with closed-loop control. In this way the melting temperature of the gallium could be reached quickly at one power setting, then maintained at a lower power setting.

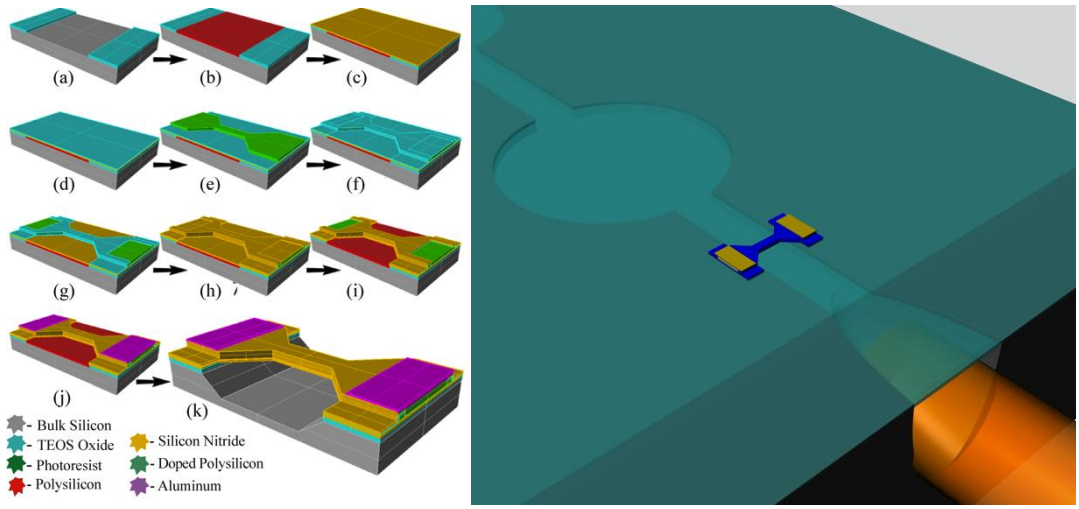

(a) (b)

Figure 6-12: Hot wire anemometry
(a) Fabrication process of one-wire anemometer developed to measure low flow rates.
(b) Drawing showing placement of anemometer in fluid channel. Current fabrication is incompatible with the pump presented in this dissertation and another process would need to be developed to make it compatible. (a) ©2010 Reprinted, with permission, from (Johnson, et al., 2010)

The presented pump was designed with gallium actuators, whose melting point of 303 K renders it useless for implantation into biological systems; the temperature of the mouse model is 310 K. Implantation into the mouse model will require an alloy of gallium and indium that would raise the melting point to between 310 K and 320 K. The melting point of the alloy can be tuned to minimize power consumption.

Sensors and other Lab-On-A-Chip technologies can be added to the fluidic chip such as modules for fluid separations and mixing (Shen, Mokkapati, Pham, & Sarro, 2012) or for detection of compounds of interest (Stemple, Hyuck-Jin, & Jeong-Yeol, 2012). In this way the basic pump could be used to sample the biologic system to test for antigens in the blood. (Johnson, et al., 2010) designed a low flow rate hot wire anemometer that could be integrated into flow channels as shown in Figure 6-12. A compatible process would need to be developed to combine the fabrication of the pump and the sensor in the same flow path.

References

Abe, Y., Chinzei, T., Imachi, K., Mabuchi, K., Atsumi, K., & Fujimasa, I. (1990). An artificial heart driven by liquid gas. *ASAIO Transactions, 36*(Compendex), M261-M263.

Akil, O., Seal, R. P., Burke, K., Wang, C., Alemi, A., During, M., et al. (2012). Restoration of Hearing in the VGLUT3 Knockout Mouse Using Virally Mediated Gene Therapy. *Neuron, 75*(2), 283-293.

Alzet. (2013). Alzet pumps: How does it work. Retrieved 1/1/2013, 2013, from http://www.alzet.com/products/ALZET_Pumps/howdoesitwork.html

Anderson, J. R., Chiu, D. T., Jackman, R. J., Cherniavskaya, O., McDonald, J. C., Wu, H., et al. (2000). Fabrication of topologically complex three-dimensional microfluidic systems in PDMS by rapid prototyping. *Analytical Chemistry, 72*(14), 3158-3164.

Anderson, T. J., & Ansara, I. (1991). The Ga-In (Gallium-Indium) System. *Journal of Phase Equilibria, 12*(1), 64-72.

Ateya, D. A., Shah, A. A., & Hua, S. Z. (2004). An electrolytically actuated micropump. *Review of Scientific Instruments, 75*(Compendex), 915-920.

Ateya, D. A., Shah, A. A., & Hua, S. Z. (2004). An electrolytically actuated micropump. *Review of Scientific Instruments, 75*(Copyright 2004, IEE), 915-920.

Bendib, S., & Francais, O. (2001). *Analytical study of microchannel and passive microvalve: application to micropump simulator.* Paper presented at the Design, Characterization, and Packaging for MEMS and Microelectronics II, 17-19 Dec. 2001, USA.

Bergman, T. L., & Incropera, F. P. (2011). *Fundamentals of heat and mass transfer* (7th ed.). Hoboken, NJ: Wiley.

Boden, R., Hjort, K., Schweitz, J. A., & Simu, U. (2008). A metallic micropump for high-pressure microfluidics. *Journal of Micromechanics and Microengineering, 18*(Copyright 2008, The Institution of Engineering and Technology), 115009 (115007 pp.).

Borkholder, D. (2008). State-of-the-art mechanisms of intracochlear drug delivery. *Curr Opin Otolaryngol Head Neck Surg, 16*(5), 472-477.

Bowie, W., & Zhao, Y. P. (2004). Monte Carlo simulation of vapor deposition polymerization. *Surface Science, 563*(1), 245-250.

Brask, A., Kutter, J. P., & Bruus, H. (2005). Long-term stable electroosmotic pump with ion exchange membranes. *Lab on a Chip, 5*(7), 730-738.

Brayden, D., Oudot, E., & Baird, A. (2010). Drug delivery systems in domestic animal species. *Handb Exp Pharmacol, 199*, 79-112.

Brazzle, J. D., Dokmeci, M. R., & Mastrangelo, C. H. (2004). *Modeling and characterization of sacrificial polysilicon etching using vapor-phase xenon difluoride.* Paper presented at the 17th IEEE International Conference on Micro Electro Mechanical Systems. Maastricht MEMS 2004 Technical Digest, 25-29 Jan. 2004, Piscataway, NJ, USA.

Broer, D. J., & Luijks, W. (1981). Penetration Of P-Xylylene Vapor Into Small Channels Prior To Polymerization. *Journal of Applied Polymer Science, 26*(7), 2415-2422.

Brown, J. N., Miller, J. M., Altschuler, R. A., & Nuttall, A. L. (1993). Osmotic pump implant for chronic infusion of drugs into the inner ear. *Hearing Research, 70*(Copyright 1993, IEE), 167-172.

Cale, T. S., Bae, D.-L., Jezewski, C., & Senkevich, J. J. (2005). *Pore sealing for low-k delectric integration into integrated circuits.* Paper presented at the 207th Meeting of the Electrochemical Society, May 15-20 2005, Quebec, Canada.

Carlen, E. T., & Mastrangelo, C. H. (2002). Surface micromachined paraffin-actuated microvalve. *Journal of Microelectromechanical Systems, 11*(5), 408-420.

Carlson, G. A., Bair, R. E., & Gaona, J. I. (1982). An implantable, remotely programmable insulin infusion system. *Medical Progress through Technology, 9*(Compendex), 17-25.

Carson, B. S., Wu, Q., Tyler, B., Sukay, L., Raychaudhuri, R., DiMeco, F., et al. (2002). New approach to tumor therapy for inoperable areas of the brain: chronic intraparenchymal drug delivery. *J Neurooncol, 60*(2), 151-158.

Chen, C.-L., Selvarasah, S., Chao, S.-H., Khanicheh, A., Mavroidis, C., & Dokmeci, M. R. (2007). *An electrohydrodynamic micropump for on-chip fluid pumping on a flexible parylene substrate.* Paper presented at the 2007 2nd IEEE International Conference on Nano/Micro Engineered and Molecular Systems, IEEE NEMS 2007, January 16, 2007 - January 19, 2007, Bangkok, Thailand.

Chen, L., Lee, S., Choo, J., & Lee, E. K. (2008). Continuous dynamic flow micropumps for microfluid manipulation. *Journal of Micromechanics and Microengineering, 18*(Compendex).

Chen, Z., Mikulec, A. A., McKenna, M. J., Sewell, W. F., & Kujawa, S. G. (2006). A method for intracochlear drug delivery in the mouse. *Journal of neuroscience methods, 150*(1), 67-73.

Chia, B. T., Hsin-Hung, L., & Yao-Joe, Y. (2011). A novel thermo-pneumatic peristaltic micropump with low temperature elevation on working fluid. *Sensors and Actuators: A Physical, 165*(1), 86-93.

Christensen, A. M., Chang-Yen, D. A., & Gale, B. K. (2005). Characterization of interconnects used in PDMS microfluidic systems. *Journal of Micromechanics and Microengineering, 15*(5), 928-934.

Cosens, M. E. (1983). Parylene conformal coatings [PCB protection]. *Electronic Production, 12*(3), 12-13.

Dash, A., & Cudworth, G. n. (1998). Therapeutic applications of implantable drug delivery systems. *J Pharmacol Toxicol Methods, 40*(1), 1-12.

Deng, Y., Liu, Z., Zhang, P., Wu, Y., & Korvink, J. G. (2010). *Optimization of no-moving part fluidic resistance microvalves with low Reynolds number.* Paper presented at the 23rd IEEE International Conference on Micro Electro Mechanical Systems, MEMS 2010, January 24, 2010 - January 28, 2010, Hong Kong, China.

Deshpande, M., Gilbert, J. R., Bardell, R. L., & Forster, F. R. (1998). *Design analysis of no-moving-parts valves for micropumps.* Paper presented at the Proceedings of the 1998 ASME International Mechanical Engineering Congress and Exposition, November 15, 1998 - November 20, 1998, Anaheim, CA, USA.

Dong, X., Bingchu, C., Guifu, D., Yong, Z., Aibing, Y., Li, W., et al. (1999). *A novel micropump actuated by thin film shape memory alloy*, Gold Coast, Qld., Australia.

Dow, C. (2007). SILASTIC® MDX4-4210 BioMedical Grade Elastomer.

Eckenhoff, B. (1981). Osmotically driven pumps for rate-controlled delivery of solutions and viscous suspensions. *AIChE Symposium Series, 77*(Compendex), 1-9.

Fadl, A., Zhang, Z., Geller, S., Tolke, J., Krafczyk, M., & Meyer, D. (2009). The effect of the microfluidic diodicity on the efficiency of valve-less rectification micropumps using Lattice Boltzmann Method. *Microsystem Technologies, 15*(Compendex), 1379-1387.

Fan, Z., Engel, J. M., Chen, J., & Liu, C. (2004). Parylene surface-micromachined membranes for sensor applications. *13*(3), 484-490.

Feldmann, M., Demming, S., Lesche, C., & Buttgenbach, S. (2008). *Novel electro magnetic micro pump.* Paper presented at the BioMEMS and Nanotechnology III, December 5, 2007 - December 7, 2007, Canberra, ACT, Australia.

Feng, G.-H., & Kim, E. S. (2005). Piezoelectrically actuated dome-shaped diaphragm micropump. *14*(2), 192-199.

Fiering, J., Mescher, M. J., Leary Swan, E. E., Holmboe, M. E., Murphy, B. A., Chen, Z., et al. (2009). Local drug delivery with a self-contained, programmable, microfluidic system. *Biomedical Microdevices, 11*(Compendex), 571-578.

Gerlach, T., & Wurmus, H. (1995). *Working principle and performance of the dynamic micropump.* Paper presented at the Proceedings of the 1995 IEEE Micro Electro Mechanical Systems Conference, January 29, 1995 - Febrary 2, 1995, Amsterdam, Neth.

Ghalichechian, N., Modafe, A., Beyaz, M. I., & Ghodssi, R. (2008). Design, fabrication, and characterization of a rotary micromotor supported on microball bearings. *Journal of Microelectromechanical Systems, 17*(Compendex), 632-642.

Giacchino, L., & Yu-Chong, T. (2008). *Parylene-membrane piezoresistive pressure sensors with XeF2-etched cavity*, Piscataway, NJ, USA.

Gonzalez, C., Collins, S. D., & Smith, R. L. (1997a, 1998). *Fluidic interconnects for modular assembly of chemical micro systems.* Paper presented at the *9th International Solid State Sensors and Actuators Conference (Transducers '97)*, Chicago, IL, USA.

Gonzalez, C., Collins, S. D., & Smith, R. L. (1997b, 1998). *Fluidic interconnects for modular assembly of chemical micro systems.* Paper presented at the 9th International Solid State Sensors and Actuators Conference (Transducers '97), 16-19 June 1997, Chicago, IL, USA.

Gray, B. L., Jaeggi, D., Mourlas, N. J., van Drieenhuizen, B. P., Williams, K. R., Maluf, N. I., et al. (1999). Novel interconnection technologies for integrated microfluidic systems. *Sensors and Actuators A (Physical), A77*(1), 57-65.

Grosjean, C., Xing, Y., & Yu-Chong, T. (1999). *A practical thermopneumatic valve.* Paper presented at the Proceedings of 12th International Workshop on Micro Electro Mechanical Systems - MEMS, 17-21 Jan. 1999, Piscataway, NJ, USA.

Grytsenko, K. P., & Tolstopyatov, E. M. (2004). *Thickness distribution of gas phase coatings in confined channels.* Paper presented at the Symposium G on Protective Coatings and Thin Films, of the E-MRS 2003 Spring Conference, 10-13 June 2003, Strasbourg, France.

Gulley, R. J., & Buckman, S. J. (1999). Absolute elastic electron scattering from benzene. *Journal of Physics B (Atomic, Molecular and Optical Physics), 32*(14), 405-409.

Guo, S., Nakamura, T., Fukuda, T., & Oguro, K. (1996). *Design and experiments of micro pump using ICPF actuator*, Nagoya, Jpn.

Hong-Seok, N., Yong, H., & Hesketh, P. J. (2004). Parylene micromolding, a rapid and low-cost fabrication method for parylene microchannel. *Sensors and Actuators B (Chemical), B102*(1), 78-85.

Hongbin, W., Krampe, E., Schlicht, H., & Wintermantel, E. (2009). *Application of a microcellular injection molding process (MuCell) to produce an implant with porous structure.* Paper presented at the 11th International Congress of the IUPESM. Medical Physics and Biomedical Engineering. World Congress 2009. Biomaterials, Cellular and Tissue Engineering, Artificial Organs, 7-12 Sept. 2009, Berlin, Germany.

Hwang, I.-H., An, J.-Y., Ko, K.-H., Shin, S.-M., & Lee, J.-H. (2007). A novel micropump with fixed-geometry valves and low leakage flow. *Journal of Micromechanics and Microengineering, 17*(8), 1632-1639.

Inamoto, R., Miyashita, T., Akiyama, K., Mori, T., & Mori, N. (2009). Endolymphatic sac is involved in the regulation of hydrostatic pressure of cochlear endolymph. *Am J Physiol Regul Integr Comp Physiol, 297*(5), R1610-1614.

Inglesfield, J. E. (1968). The structure and phase changes of gallium. *J. Phys. C, 1*, 1337-1346.

Izumikawa, M., Minoda, R., Kawamoto, K., Abrashkin, K. A., Swiderski, D. L., Dolan, D. F., et al. (2005). Auditory hair cell replacement and hearing improvement by Atoh1 gene therapy in deaf mammals. *Nat Med, 11*(3), 271-276.

Jang, J., & Lee, S. S. (2000). Theoretical and experimental study of MHD (magnetohydrodynamic) micropump. *Sensors and Actuators A (Physical), A80*(1), 84-89.

Jang, L.-S., Li, Y.-J., Lin, S.-J., Hsu, Y.-C., Yao, W.-S., Tsai, M.-C., et al. (2007). A stand-alone peristaltic micropump based on piezoelectric actuation. *Biomedical Microdevices, 9*(2), 185-194.

Jang, L.-S., & Yu, Y.-C. (2008). Peristaltic micropump system with piezoelectric actuators. *Microsystem Technologies, 14*(2), 241-248.

Jeong, O. C., & Konishi, S. (2008). Fabrication of a peristaltic micro pump with novel cascaded actuators. *Journal of Micromechanics and Microengineering, 18*(Compendex).

Jero, J., Tseng, C. J., Mhatre, A. N., & Lalwani, A. K. (2001). A surgical approach appropriate for targeted cochlear gene therapy in the mouse. *Hearing research, 151*(1-2), 106-114.

Johnson, D. G., Frisina, R. D., & Borkholder, D. A. (2011). In-plane Biocompatible Microfluidic Interconnects for Implantable Microsystems. *IEEE Transactions on Biomedical Engineering, 58*(Copyright 2011, The Institution of Engineering and Technology), 943-948.

Johnson, D. G., Waldron, M. J., Frisina, R. D., & Borkholder, D. A. (2010, 2010). *Implantable Micropump Technologies for Murine Intracochlear Infusions.* Paper presented at the 2010 32nd Annual International Conference of the IEEE Engineering in Medicine and Biology Society (EMBC 2010), 31 Aug.-4 Sept. 2010, Buenos Aires, Argentina.

Johnson, D. G., Zhu, X. X., Frisina, R. D., & Borkholder, D. A. (2007). *Micro-molded cannulae for intracochlear infusions in small rodents.* Paper presented at the 29th Annual International

Conference of IEEE-EMBS, Engineering in Medicine and Biology Society, EMBC'07, August 23, 2007 - August 26, 2007, Lyon, France.

Jung Ho, K., King Tong, L., & Diamond, D. (2008). *Fabrication of microfluidic pump using conducting polymer actuator*, Taichung, Taiwan.

Kawamoto, K., Oh, S.-H., Kanzaki, S., Brown, N., & Raphael, Y. (2001). The Functional and Structural Outcome of Inner Ear Gene Transfer via the Vestibular and Cochlear Fluids in Mice. *Molecular therapy : the journal of the American Society of Gene Therapy, 4*, 575-585.

Kim, H., & Najafi, K. (2007). Characterization of aligned wafer-level transfer of thin and flexible parylene membranes. *16*(6), 1386-1396.

Kim, S., & Karrila, S. J. (1991). *Microhydrodynamics : principles and selected applications*. Boston: Butterworth-Heinemann.

Kingma, G. G., Miller, J. M., & Myers, M. W. (1992). Chronic drug infusion into the scala tympani of the guinea pig cochlea. *Journal of Neuroscience Methods, 45*(1-2), 127-134.

Komaromy, A. M., Varner, S. E., de Juan, E., Acland, G. M., & Aguirre, G. D. (2006). Application of a new subretinal injection device in the dog. *Cell Transplant, 15*(6), 511-519.

Komatsu, S., Binh-Khiem, N., Iwase, E., Matsumoto, K., & Shimoyama, I. (2009). *Peristaltic micropump fabricated by depositing parylene directly on liquid.* Paper presented at the TRANSDUCERS 2009 - 15th International Conference on Solid-State Sensors, Actuators and Microsystems, June 21, 2009 - June 25, 2009, Denver, CO, United states.

Korivi, N. S., & Li, J. (2007a). *A generic chip-to-world fluidic interconnect system for microfluidic devices.* Paper presented at the *Annual Southeastern Symposium on System Theory*, Macon, GA, United States.

Korivi, N. S., & Li, J. (2007b). *A generic chip-to-world fluidic interconnect system for microfluidic devices*, Macon, GA, United States.

Lacour, S. P., Atta, R., FitzGerald, J. J., Blamire, M., Tarte, E., & Fawcett, J. (2008). Polyimide micro-channel arrays for peripheral nerve regenerative implants. *Sensors and Actuators, A: Physical, 147*(2), 456-463.

Licari, J. J. (2003). *Coating materials for electronic applications :polymers, processes, reliability, testing*. Norwich, NY: Noyes Publications/William Andrew Publ.

Limited, T. D. C. (2007). Microfluidic Edge Connector. Retrieved June 22, 2009

Lo, R., & Meng, E. (2011). A modular heat-shrink-packaged check valve with high pressure shutoff. *Journal of Microelectromechanical Systems, 20*(5), 1163-1173.

Long, C. S., & Loveday, P. W. (2007). *A thermo-hydraulic wax actuation system for high force and large displacement applications.* Paper presented at the Industrial and Commercial Applications of Smart Structures Technologies 2007, 19 March 2007, USA.

Louisos, W. F., & Hitt, D. L. (2008). Viscous effects on performance of two-dimensional supersonic linear micronozzles. *Journal of Spacecraft and Rockets, 45*(Compendex), 706-715.

Loverich, J., Kanno, I., & Kotera, H. (2007). Single-step replicable microfluidic check valve for rectifying and sensing low Reynolds number flow. *Microfluidics and Nanofluidics, 3*(4), 427-435.

Majumdar, A., Satyanarayana, S., & McCormick, D. T. (2006). Parylene micro membrane capacitive sensor array for chemical and biological sensing. *115*(1), 494-502.

Marks, L. S. (1978). Marks' standard handbook for mechanical engineers (pp. v.). New York: McGraw-Hill.

McVittie, J. P., Rey, J. C., Bariya, A. J., IslamRaja, M. M., Cheng, L. Y., Ravi, S., et al. (1991). *SPEEDIE. A profile simulator for etching and deposition.* Paper presented at the Advanced Techniques for Integrated Circuit Processing, October 1, 1990 - October 5, 1990, Santa Clara, CA, USA.

Meng, G., Zhang, W.-M., Huang, H., Li, H.-G., & Chen, D. (2009). Micro-rotor dynamics for micro-electro-mechanical systems (MEMS). *Chaos, Solitons and Fractals, 40*(2), 538-562.

Metz, S., Bertzch, A., Bertrand, D., & Renaud, P. (2004). Flexible polyimide probes with microelectrodes and embedded microfluidic channels for simultaneous drug delivery and multichannel monitoring of bioelectric activity. *Biosensors & Bioelectronics, 19*(10), 1309-1318.

Mori, T., & Mizutani, T. (1992). High-electric field conduction and dielectric breakdown of modified poly-p-xylylene thin films. I. Improvement of insulation properties through using physical and chemical modifications. *Transactions of the Institute of Electrical Engineers of Japan, Part A, 112-A*(3), 173-179.

Morinigo, J. A., & Hermida-Quesada, J. (2010). Solid-gas surface effect on the performance of a MEMS-class nozzle for micropropulsion. *Sensors and Actuators, A: Physical, 162*(Compendex), 61-71.

Munson, B. R., Young, D. F., & Okiishi, T. H. (2005). *Fundamentals of fluid mechanics* (5th ed.). New York: Wiley.

Najafi, K. (2007). *Packaging of implantable microsystems.* Paper presented at the 6th IEEE Conference on SENSORS, IEEE SENSORS 2007, October 28, 2007 - October 31, 2007, Atlanta, GA, United states.

Nan-Chyuan, T., & Sue, C. Y. (2007). Review of MEMS-based drug delivery and dosing systems. *Sensors and Actuators A (Physical), 134*(2), 555-564.

Neagu, C., Jansen, H., Gardeniers, H., & Elwenspoek, M. (2000). Electrolysis of water: An actuation principle for MEMS with a big opportunity. *Mechatronics, 10*(4), 571-581.

NIDCD. (2012). Worksheet Summary for Inner Ear/Sensorineural Hearing Loss. Retrieved 12/29/2012, 2012, from http://www.nidcd.nih.gov/funding/programs/ot/pages/inner_ear_summary.aspx

Nisar, A., Afzulpurkar, N., Mahaisavariya, B., & Tuantranont, A. (2008). MEMS-based micropumps in drug delivery and biomedical applications. *Sensors and Actuators, B: Chemical, 130*(Compendex), 917-942.

Nuxoll, E., & Siegel, R. (2009). BioMEMS devices for drug delivery. *IEEE Engineering in Medicine and Biology Magazine, 28*(1), 31-39.

Ok Chan, J., & Konishi, S. (2007). Fabrication and drive test of pneumatic PDMS micro pump. *Sensors and Actuators A (Physical), 135*(2), 849-856.

Pararas, E. E., Borkholder, D. A., & Borenstein, J. T. (2012). Microsystems technologies for drug delivery to the inner ear. *Adv Drug Deliv Rev*.

Pasupuleti, A., & Sahin, F. (2007). *Soft computing techniques for determining the effective Young's Modulus of materials in thin films.* Paper presented at the 2006 IEEE International Conference on Systems, Man and Cybernetics, October 8, 2006 - October 11, 2006, Taipei, Taiwan.

Prakash, P., Grissom, M. D., Rahn, C. D., & Zydney, A. L. (2006). Development of an electroosmotic pump for high performance actuation. *286*(1-2), 153-160.

Prieskorn, D. M., & Miller, J. M. (2000). Technical report: chronic and acute intracochlear infusion in rodents. *Hearing Research, 140*(1-2), 212-215.

Puntambekar, A., & Ahn, C. H. (2002). Self-aligning microfluidic interconnects for glass- and plastic-based microfluidic systems. *Journal of Micromechanics and Microengineering, 12*(1), 35-40.

Rahman, M. A., Ahmed, F., Zhao, Y., & Gong, T. H. (2000). *Novel diffuser-nozzle micropump actuated by thermal bubble.* Paper presented at the Smart Structures and Materials 2000: Smart Electronics and MEMS, Newport Beach, CA, USA.

Ramachandran, A., Junk, M., Koch, K. P., & Hoffmann, K. P. (2007). A study of parylene C polymer deposition inside microscale gaps. *IEEE Transactions on Advanced Packaging, 30*(4), 712-724.

Richardson, R. T., Wise, A. K., Thompson, B. C., Flynn, B. O., Atkinson, P. J., Fretwell, N. J., et al. (2009). Polypyrrole-coated electrodes for the delivery of charge and neurotrophins to cochlear neurons. *Biomaterials, 30*(13), 2614-2624.

Richter, M., Linnemann, R., & Woias, P. (1998). Robust design of gas and liquid micropumps. *Sensors and Actuators, A: Physical, 68*(Compendex), 480-486.

Sadler, D. J., Changrani, R. G., Chou, C.-F., Zindel, D., Burdon, J. W., & Zenhausern, F. (2001). *Ceramic magnetohydrodynamic (MHD) micropump.* Paper presented at the Microfluidics and BioMEMS, October 22, 2001 - October 24, 2001, San Francisco, CA, United states.

Schütz, M., Scimemi, P., Majumder, P., De Siati, R. D., Crispino, G., Rodriguez, L., et al. (2010). The human deafness-associated connexin 30 T5M mutation causes mild hearing loss and reduces biochemical coupling among cochlear non-sensory cells in knock-in mice. *Hum Mol Genet, 19*(24), 4759-4773.

Sclafani, A., & Glendinning, J. (2003). Flavor preferences conditioned in C57BL/6 mice by intragastric carbohydrate self-infusion. *Physiol Behav, 79*(4-5), 783-788.

Sefton, M. V. (1987). Implantable Pumps. *Critical Reviews in Biomedical Engineering, 14*(Compendex), 201-240.

Seibel, K., Scholer, L., Schafer, H., & Bohm, M. (2008). A programmable planar electroosmotic micropump for lab-on-a-chip applications. *Journal of Micromechanics and Microengineering, 18*(Compendex).

Shen, C., Mokkapati, V. R. S. S., Pham, H. T. M., & Sarro, P. M. (2012). Micromachined nanofiltration modules for lab-on-a-chip applications. *Journal of Micromechanics and Microengineering, 22*(2), 025003 (025010 pp.).

Shifeng, L., & Shaochen, C. (2003). Polydimethylsioxane fluidic interconnects for microfluidic systems. *IEEE Transactions on Advanced Packaging, 26*(3), 242-247.

Singhal, V., Garimella, S. V., & Murthy, J. Y. (2004). Low Reynolds number flow through nozzle-diffuser elements in valveless micropumps. *Sensors and Actuators, A: Physical, 113*(Compendex), 226-235.

Stemple, C. C., Hyuck-Jin, K., & Jeong-Yeol, Y. (2012). Rapid and sensitive detection of malaria antigen in human blood with lab-on-a-chip. *IEEE Sensors Journal, 12*(9), 2735-2736.

Sugano, K., & Tabata, O. (2002). *Techniques for reduction in surface roughness and aperture size effect for XeF2 etching of Si.* Paper presented at the MHS2002. Proceedings of 2002 International Symposium on Micromechatronics and Human Science, 20-23 Oct. 2002, Piscataway, NJ, USA.

Swan, E. E. L., Mescher, M. J., Sewell, W. F., Tao, S. L., & Borenstein, J. T. (2008). Inner ear drug delivery for auditory applications. *Advanced Drug Delivery Reviews, 60*(15), 1583-1599.

Thorne, M., Salt, A., DeMott, J., Henson, M., Henson, O. J., & Gewalt, S. (1999). Cochlear fluid space dimensions for six species derived from reconstructions of three-dimensional magnetic resonance images. *Laryngoscope, 109*(10), 1661-1668.

Timoshenko, S. (1940). *Theory of plates and shells* (1st ed.). New York, London,: McGraw-Hill Book Company, inc.

Tingrui, P., Baldi, A., & Ziaie, B. (2006). A reworkable adhesive-free interconnection technology for microfluidic systems. *Journal of Microelectromechanical Systems, 15*(1), 267-272.

Tocci, A. M., Flores, E. S. E., & Mascheroni, R. H. (1997). Enthalpy, Heat Capacity and Thermal Conductivity of Boneless Mutton between -40 and +40 °C. *Lebensmittel-Wissenschaft und-Technologie, 30*(2), 184-191.

Tolinski, M. (2005). Macro challenges in micromolding. *Plastics Engineering, 61*, 14-16.

Tolstopyatov, E. M., Yang, S. H., & Kim, M. C. (2002). Thickness uniformity of gas-phase coatings in narrow channels: II. One-side confined channels. *Journal of Physics D: Applied Physics, 35*(21), 2723-2730.

Uhlig, E. L. P., Graydon, W. F., & Zingg, W. (1983). ELECTRO-OSMOTIC ACTUATION OF IMPLANTABLE INSULIN MICROPUMPS. *Journal of Biomedical Materials Research, 17*(6), 931-943.

Urbanchek, M. G., Picken, E. B., Kalliainen, L. K., & Kuzon, W. M. (2001). Specific force deficit in skeletal muscles of old rats is partially explained by the existence of denervated muscle fibers. *J Gerontol A Biol Sci Med Sci, 56*(5), B191-197.

URMC. (2012). Audiology: Glossary of Terms. Retrieved 12/29/2012, 2012, from http://www.urmc.rochester.edu/audiology/glossary.cfm

Waldschik, A., & Buttgenbach, S. (2010). *Micro gear pump with internal electromagnetic drive*, Tiergartenstrasse 17, Heidelberg, D-69121, Germany.

Wang, C.-H., & Lee, G.-B. (2006). Pneumatically driven peristaltic micropumps utilizing serpentine-shape channels. *Journal of Micromechanics and Microengineering, 16*(2), 341-348.

White, F. M. (1979). *Fluid mechanics*. New York: McGraw-Hill Science, 2010.

White, F. M. (2011). *Fluid mechanics* (7th ed.). New York, N.Y.: McGraw Hill.

Woias, P. (2005). Micropumps - past, progress and future prospects. *Sensors and Actuators B (Chemical), 105*(Copyright 2005, IEE), 28-38.

Wu, C.-L., Yang, J.-C., & Chen, Y.-C. (2006). *Low power consumption PZT actuated micro-pump.* Paper presented at the 2006 International Microsystems, Packaging, Assembly Conference Taiwan, IMPACT, October 18, 2006 - October 20, 2006, Taipei, Taiwan.

Xu, D., Cai, B., Ding, G., Zhou, Y., Yu, A., Wang, L., et al. (1999). *Novel micropump actuated by thin film shape memory alloy.* Paper presented at the Electronics and Structures for MEMS, Gold Coast, Australia.

Xu, G., Tay, F. E. H., Iliescu, C., & Luar, V. (2005). *Self-priming and bubble tolerant micro-pump.* Paper presented at the Biomedical Applications of Micro- and Nanoengineering II, December 13, 2004 - December 15, 2004, Sydney, NSW, Australia.

Yang, B., & Lin, Q. (2007). Planar micro-check valves exploiting large polymer compliance. *Sensors and Actuators, A: Physical, 134*(1), 186-193.

Yang, X., Grosjean, C., Tai, Y.-C., & Ho, C.-M. (1998). MEMS thermopneumatic silicone rubber membrane valve. *Sensors and Actuators, A: Physical, 64*(1), 101-108.

Yoon, J. S., Choi, J. W., Lee, I. H., & Kim, M. S. (2007). A valveless micropump for bidirectional applications. *Sensors and Actuators, A: Physical, 135*(2), 833-838.

Yun, K. S., Cho, I. J., Bu, J. U., Kim, G. H., Jeon, Y. S., Kim, C. J., et al. (2001). *A micropump driven by continuous electrowetting actuation for low voltage and low power operations.* Paper presented at the 14th IEEE International Conference on Micro Electro Mechanical Systems (MEMS 2001), January 21, 2001 - January 25, 2001, Interlaken, Switzerland.

Zahn, J. (2006). Micropump Applications in Bio-MEMS *Bio-MEMS* (pp. 143-175): CRC Press.

Zengerle, R., Ulrich, J., Kluge, S., Richter, M., & Richter, A. (1995). Bidirectional silicon micropump. *Sensors and Actuators, A: Physical, 50*(1-2), 81-86.

Zopfl, T., Klare, S., Wachutka, G., & Schrag, G. (2009). *Characterisation of the intrinsic stress in micromachined parylene membranes.* Paper presented at the Smart Sensors, Actuators and MEMS IV, 4-6 May 2009, USA.

Appendix A Parylene C Deposition Model

If we knew what we were doing it wouldn't be research.
Albert Einstein

The Parylene C deposition model used in the body of this work is based on a number of assumptions, such as assuming molecular diffusion through a triangular cross-sectioned channel will behave as diffusion through a round channel. Though this model served well in providing design guidance for the interconnect devices, a more robust model adaptable to a wider range of geometries and deposition pressures is desirable. Dr. Steven Weinstein, Dr. Karuna Koppola, and Dr. Masoumeh Haghpanahi helped with the theory and mathematics, the MATLAB code, and the data validation. The proposed model, based on first principles, has an advantage over models making broader assumptions, (Broer & Luijks, 1981; Ramachandran, et al., 2007), in that the model predicts the occlusive filling of the channels and not just the initial deposition in straight channels. Consider a binary mixture consisting of Parylene C monomers in air at a low pressure. 'A' represents the Parylene C that solidify at a moving boundary where flow is assumed to be completely concentration driven. The system is assumed not to be concentration driven, dilute in A, but of sufficiently low concentration to be pressure independent and therefor in the molecular flow regime.

Verification devices were fabricated with Kapton tape and glass microscope slides which allowed for increased ease of fabrication since they did not require masking or etching. Glass slides were used as the upper and lower channel surfaces with strips of polyimide tape on one slide creating the sides of the channels (see Figure A-1). The channel height, being much less than the width, dominates and is considered to be the characteristic channel height of the system.

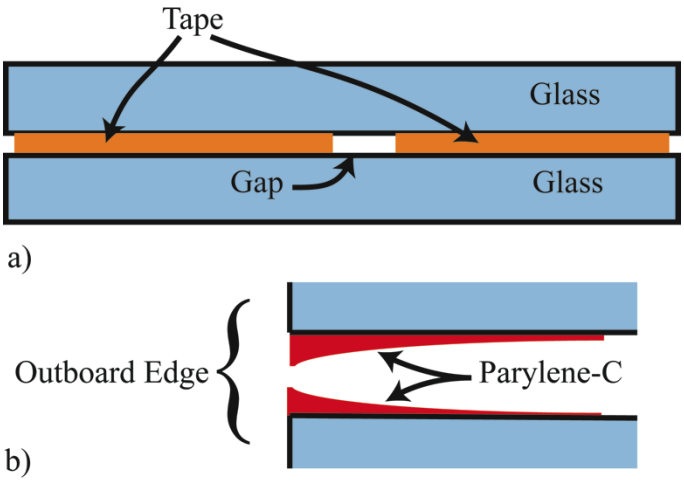

Figure A-1: Experimental setup to measure Parylene C deposition in straight channels.
Kapton tape of known thickness was applied to one side of a glass microscope slide in a 'U' configuration. The open end of the tape 'U' is aligned to the edge of the slide. The channel was formed by clamping a second slide to the topside of the tape. (a) Side view of the gap entrance (b) cross-sectional view of gap showing deposited Parylene C (in red)

The analysis begins with the equation for molar balance in bulk (A-1), the flux relation (A-2), and Fick's law (A-3). Although there are two components in the system, A and B, only the solidifying component A is of concern.

(A-1)

(A-2)

(A-3)

C_A is the concentration of the monomer, μ_A is the average velocity, J_A is the flux, and D is the diffusion coefficient . Boundary conditions were derived from the physical set up (see Figure A-2). The concentration of component A at the entrance, $x = 0$, is equal to the concentration in the chamber, C_{A0}, which is assumed to be constant during the deposition.

(A-4)

(A-5)

A finite channel is assumed, of length L, with zero flux in the x direction at the terminus of the channel and zero concentration within the channel before time $t = 0$.

(A-6)

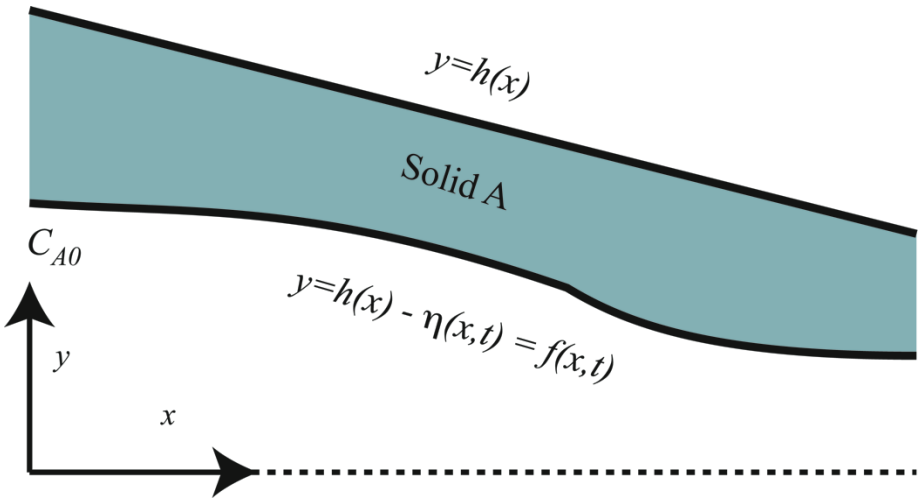

Figure A-2: Drawing of the tapered channel system consisting of A in gas and as a solid.
A is the solidifying component, $y = h(x)$ is the equation for one half the channel height, $y = f(x,t)$ is the function for the distance from the center of the channel to the gas / solid interface, $\eta(x,t)$ is the deposited thickness at x, and C_{A0} is the concentration of A at the channel entrance.

(A-7)

The opening height, $f(x)$, is defined as the height of the opening, $h(x)$, minus the deposition thickness, $\eta(x)$, and μ is the average velocity of both components A and B (the monomer and residual air).

(A-8)

Flux and mass conservation conditions between phases are now considered. From (A-1) and (A-2)

(A-9)

(A-10)

this with (A-3)

(A-11)

(A-12)

(A-13)

(A-14)

(A-15)

(A-16)

C_{A0} and C_S are the concentrations of component A in the gas and the solid. The equations (A-12), (A-13), and (A-14) and the boundary conditions were discretized and the variables non-dimensionalized to arrive at a system of equations, using the Crank-Nicolson method, to be solved. The sticking coefficient, $1/N_s$, which is the probability that a monomer striking the wall will lead to adsorption, has been added as the model assumes that particles will actually strike many times before adsorbing. N_s is the average number of wall strikes a monomer experiences before being permanently adsorbed. In the model the sticking coefficient, $1/N_s$, has been rolled into the coefficient N_1.

Verification devices were placed in the deposition tool for incremental depositions of Parylene C. Deposition thickness in the chamber on open surfaces, not in channels, is controlled by the amount of dimer placed in the vaporizer. The first deposition with 2 grams of dimer was performed on three devices. One device, slide 1, was removed from the deposition tool and a second deposition of 2 grams of dimer was performed on the two remaining devices. One of these devices, slide 2, was removed and a final deposition of 2 grams was performed on the last device, slide 3. This left slide two with twice as much deposited thickness as slide one, and slide three had three times as much as slide 1. The slides were separated and the tape was removed, leaving stripes of deposited polymer along the channel floor. A Tencor P2 profilometer (KLA Tencor, Milpitas, California) was used to measure across the channel every 0.5 mm. Thickness measurements were taken from the maximum thickness measured in the middle of the channel. Figure A-3 is a graph of the deposition thickness for three devices with different deposition times. This data was used to determine the sticking coefficient to be used with the model.

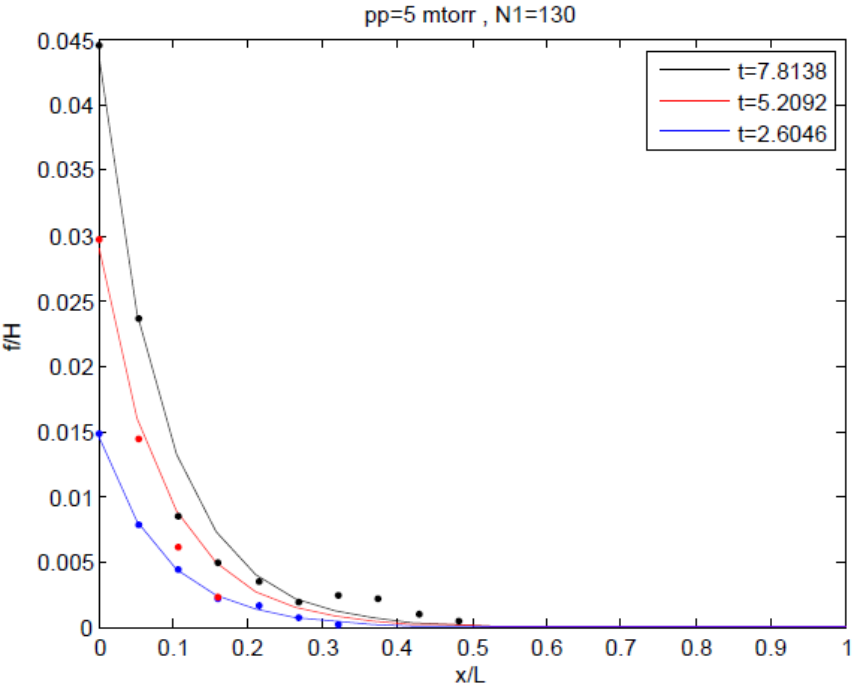

Figure A-3: Model data compared with measured thicknesses for 5 mtorr deposition.
Three identically fabricated devices were used with one device removed after deposition of 2 grams of Parylene C dimer.

Appendix B COMSOL Model

A theory has only the alternative of being right or wrong. A model has a third possibility: it may be right, but irrelevant.
Manfred Eigen

A simplified 2D COMSOL model was set up to analyze the four-chamber peristaltic pump. The model includes two chambers, each with an underlying fluid chamber covered with layers of Parylene C, 4 µm, and TEOS, 1 µm, and plena filled with one of the expansion materials with an aluminum heater element, 0.3 µm. Figure B-1 shows a drawing of the actuation portion of the model. The dimensions of the plena vary for the three actuation materials. For the air and wax, the dimensions are 1 mm by 40 µm, for gallium they are 1.5 mm by 100 µm. The material properties used to model the device are shown in Table B-1.

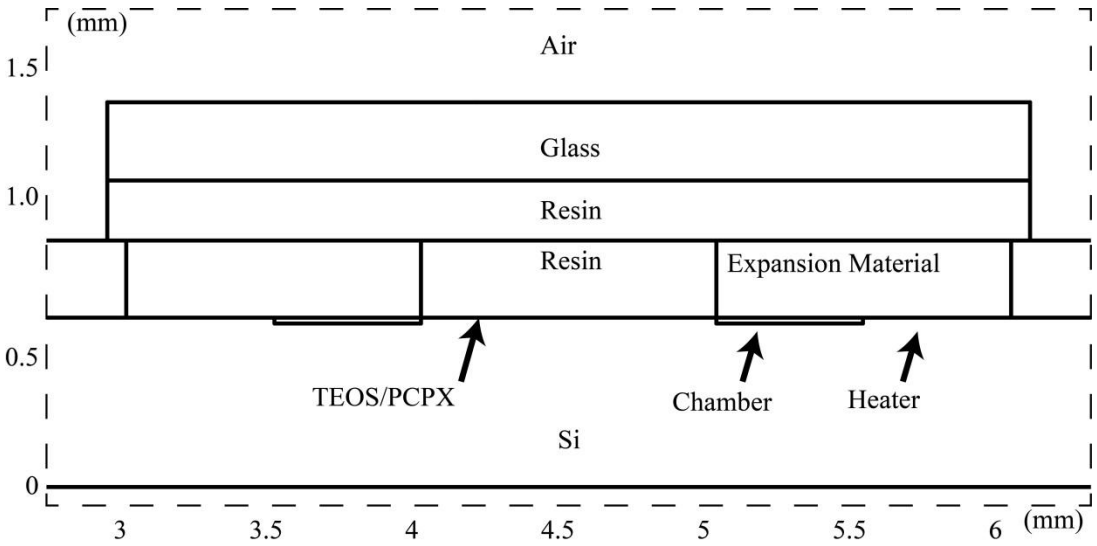

Figure B-1: Geometry of COMSOL model of two chamber device used for thermal analysis. Each chamber has an associated heater and expansion plenum. The dimensions of the plena are changed to fit the needs of the material's coefficient of expansion. The model (COMSOL 3.5a) used more than 330,000 triangular mesh units. Transient analysis was performed with pulsatile heating to mimic the peristaltic actuation cycles of the four chamber pump device.

Table B-1: Material properties used for 2D COMSOL model

Quantity	Temp.	Density	Specific Heat Capacity	Thermal Conductivity
Units	ºC	kg/m^3	J/g·K	W/m·K
Air	25	1.1465	1.005	0.02675
Wax (solid)	20	900	2.9	0.25
Wax (liquid)	60	750		
Gallium (solid)	20	5910	0.265	40.6
Gallium (liquid)	30	6095		
PCPX	25	1289	1	0.084
Si	25	2330	0.7	130
Resin	23	1400	1.35	0.4
Water	25	997.1	4.181	0.6
SiO_2	20	2200	0.73	1.4
Aluminum	20	2700	0.9	160
Animal Model	38	1060[*]	3.594[‡]	0.5[‡]

Source: (Bergman & Incropera, 2011)
[*] (Urbanchek, Picken, Kalliainen, & Kuzon, 2001)
[‡] (Tocci, Flores, & Mascheroni, 1997)

Biography

Biographies are but the clothes and buttons of the man. The biography of the man himself cannot be written
Mark Twain

Dean Johnson, raised in Williamston, MI, graduated in 1982 from Williamston High School. A National Honor Society student, he entered Michigan State University that fall as an Electrical Engineering major. He later added an emphasis in Digital/Computer Engineering. While remaining a Spartan, Dean took time off to join the United States Marine Corps in 1984. He served in the 1st Battalion 24th Marines Charlie Company in Lansing MI. After Boot Camp and Infantry Training School, Dean returned to MSU to finish his Bachelor of Science in Electrical Engineering. He continued at MSU and received his Master of Science in 1990 while working as a graduate teaching assistant. He was honorably discharged from the Marines in 1990 at the rank of sergeant. 1990 was also the year he married his longtime girlfriend, Kristen (BA English, MSU)

Dean began working as a Software/Systems Engineer for Xerox Corporation in Webster, NY in 1990. After a brief stint working for Tribune Media Services in Glens Falls, NY he entered the Microsystems Engineering Program at RIT.

He is currently working as a Postdoctoral Fellow at the University of Rochester in the Biomedical Engineering Department. He plans to continue his career in academia filling his time with teaching and research.